

Electrokinetic manipulation of micro to nano-sized objects for microfluidic application

Thesis submitted in accordance with the requirements of The
University of Liverpool for the degree of Doctor in Philosophy

By

Aleksandr Chichenkov

Department of Electrical Engineering & Electronics

July 2013

Abstract

This thesis describes experimental and numerical investigations of various electrokinetic techniques on fluorescent particles, bacteria and protein motors. The aim of this work is to extend the knowledge on the object manipulation, which is an essential part of a practical microfluidic device.

The dissertation consists of three major sections that contain novel approaches to object manipulation using electric fields. The effect of dielectrophoretic force on fluorescent particles is analysed first. Using an experimental setup with a controlled switch for the input signal, the theoretical framework for amplitude modulated response of dielectrophoretic force is developed. Also presented is the image processing software for quantitative particle motion analysis.

Another analysis of various electrokinetic techniques (dielectrophoresis, AC electroosmosis, AC electrothermal flow and electrophoresis) was carried out on *Pseudomonas Fluorescence* bacteria in a solution that supports its growth. These bacteria usually live in geometrically restricted spaces and so spatially confined transparent channels were created to mimic their natural environment. It was noted that in these conditions the motile bacteria do not experience the effect of dielectrophoretic force. The minimum frequency that can be applied to the solution without forming bubbles is too high to distinguish AC electroosmotic effect. Using the numerical simulation, however, the experimental setup that utilises the observed effect of electrophoresis and AC electrothermal flow is designed.

The final study was carried out on protein molecular motors. The novel experimental setup to investigate the effect of the electric field on the actin filament motility on five different surfaces, covered with myosin II motors, was developed. The application of higher external electric fields resulted in different velocity increases on different surfaces. Using the numerical simulation, this difference is quantitatively explained by the variation of the number of motors on surfaces. Also presented is a novel method that enables determining the forces exerted by the population of active and resistive motors without the need of expensive equipment.

Acknowledgements

I would like to thank Dr. David Bakewell for giving me the opportunity to start this PhD with his advice, support and friendship. I would also like to thank Prof. Dan Nicolau for giving me the opportunity to work on an exciting multi-million EU project and introducing me to the world of molecular motors. A very special thank you goes to Dr. Harm van Zalinge, who took over the role of a primary supervisor for his tremendous support, wisdom and guiding.

Many thanks to my friends from the work group: Jenny, Miguel, Laurence, Ben, Serban, Marie! Thank you guys, it's been quite a trip!

I would like to express my gratitude to the department of Electrical Engineering and Electronics for the financial support.

Finally I would like to thank my family for their support and faith in me.

Publications

Journal Publications:

D.J. Bakewell and A. Chichenkov "Fourier-Bessel Series Modelling of Dielectrophoretic Bionanoparticle Transport: Principles and Applications". IEEE Transactions on Nanobioscience (vol 11 issue 1 2012, pp 79-86)

D.J. Bakewell and A. Chichenkov "Quantifying dielectrophoretic nanoparticle response to amplitude modulated input signal" (vol 45, 365402, 2012). Journal of Physics D-Applied Physics, 2012. **45**(49).

Chichenkov A, Ramsey L C, Van Zalinge H, Aveyard J, Persson M, Mansson A, Nicolau D V. Estimation of the force generated in the acto-myosin system through electric field modulation of motility and stochastic simulation. In preparation (2013).

Conference Publications:

D.J. Bakewell, A. Chichenkov, N.A. Yunus "Models of Nanoparticle Transport in Dielectrophoretic Microdevices: Prediction, Parameter Estimation and Other Applications." IEEE EMBS Conference on Biomedical Engineering & Sciences (IECBES 2010)

Table of Contents

Chapter I: Introduction	1
1.1 Fluid manipulation techniques	3
1.2 Detection techniques	6
1.3 Object manipulation using electric fields.....	7
1.4 Applications.....	9
1.5 Thesis outline and authors contribution.....	11
Chapter II: Theory. Forces acting on objects in the electric field	14
2.1 Electrophoresis	15
2.2 Dielectrophoresis	16
2.2.1 Dielectric spheres in an electric field	17
2.2.2 Frequency dependent behaviour of DEP force.....	21
2.2.3 DEP of non-spherical particles	23
2.2.4 DEP of rod-shaped bacteria	25
2.3 AC Electroosmosis.....	28
2.4 AC electrothermal fluid flow	31
2.4.1 The force on the fluid in electric field due to Joule heating	32
Chapter III: Fabrication and other related technologies.....	36
3.1 Electrode fabrication using laser ablation	37
3.2 PDMS fabrication	41
Chapter IV: Amplitude Modulated Dielectrophoresis	44
4.1 Introduction	45
4.2 System model.....	47
4.3 Concepts and Parameters	49
4.4 Normalised Amplitude A_N	52
4.5 Experimental materials and methods.....	53
4.6 Number of particles and fluorescent intensity relationship	56
4.7 Effect of varying the switching frequency	58
4.8 Effect of varying the duty cycle.....	61
4.9 Conclusion	62
Chapter V: The Behaviour of the Bacteria in Channels with External Forces	64
5.1 Introduction	65

5.2 The bacterial structure and growth	66
5.3 Bacteria in channels	68
5.3.1 Overview	68
5.3.2 Bacterial Growth Conditions	71
5.2.3 Experimental procedure	72
5.4 Details of the numerical simulation	74
5.4.1 Equations used in the simulation.....	76
5.5 Results of the electric field effect on the bacteria.....	82
5.5.1 Effect of constant electric field on the bacteria.....	82
5.5.2 DEP effect on the bacteria	84
5.5.3 ACEO effect on the bacteria.....	87
5.5.4 ACET effect on the bacteria	89
5.5.5 Proposed design for a channel geometry	94
5.6 Conclusion	97
Chapter VI: The Effect of Electric Field on the Behaviour of Molecular Motors	100
6.1 Introduction	101
6.2 The molecular motors.....	102
6.2.1 Types of motility assays	103
6.2.2 Operating principle of molecular motors	105
6.2.3 Processivity of molecular motors.....	107
6.2.4 Duty cycle of molecular motors	109
6.2.5 Applications of molecular motors.....	111
6.3 Detecting the protein motors on the surface	111
6.4 Guiding the molecular motors	113
6.5 <i>In Vitro</i> motility in the electric field	116
6.5.1 Materials and methods.....	116
6.5.4 Effect of the electric field on motility	121
6.6 Model description	123
6.7 Simulated results	129
6.8 Conclusion.....	136
Chapter VII: Conclusion.....	139
Appendix	143
References	147

Chapter I: Introduction

The development of the electronic circuits and consequently the silicon fabrication technology in 20th century has had an enormous impact in various fields of science. Currently one the most developed and explored aspect of silicon fabrication from the commercial point of view is the integrated circuit based devices [1, 2]. Over the last few decades, however, an enormous interest in the alternative exploitation of the fabrication technology has been witnessed with a particular interest in microsystems for biological and chemical analysis. As a result a number of concepts have been developed including microelectromechanical system (MEMS), microfluidic devices, microarrays, etc [3, 4].

Another concept that is aimed towards developing a practical microfluidic device is a micro- total analysis system (μ TAS) or a lab-on-a-chip technology where a number of functions such as separation, concentration and detection are performed in a single device. The aim of this technology is to shrink the conventional laboratory based equipment into a chip through the integration of functional units like pumping, concentration, separation and detection systems. A number of theoretical models and academic proof-of-concept studies have demonstrated the advantages of lab-on-a-chip system over laboratory tests [5-9].

The common feature of microfluidic devices is the handling and manipulation of small amounts of fluid usually in micro and nano-liters or even in pico-liter range. These devices can have virtually any design however the system has a series of generic components: an inlet mechanism i.e. the method of introducing the reagents and samples (this can simply be a reservoir on the chip where the sample in the solution is pipetted into), a mechanism to move and mix the fluids on the chip and detection mechanism depending on the desired application of the device [10].

1.1 Fluid manipulation techniques

There is currently a wide range of techniques (a categorised list is presented in figure 1.1) to produce fluid flow that can be used as means to move the sample within the chip and/or mix the fluids.

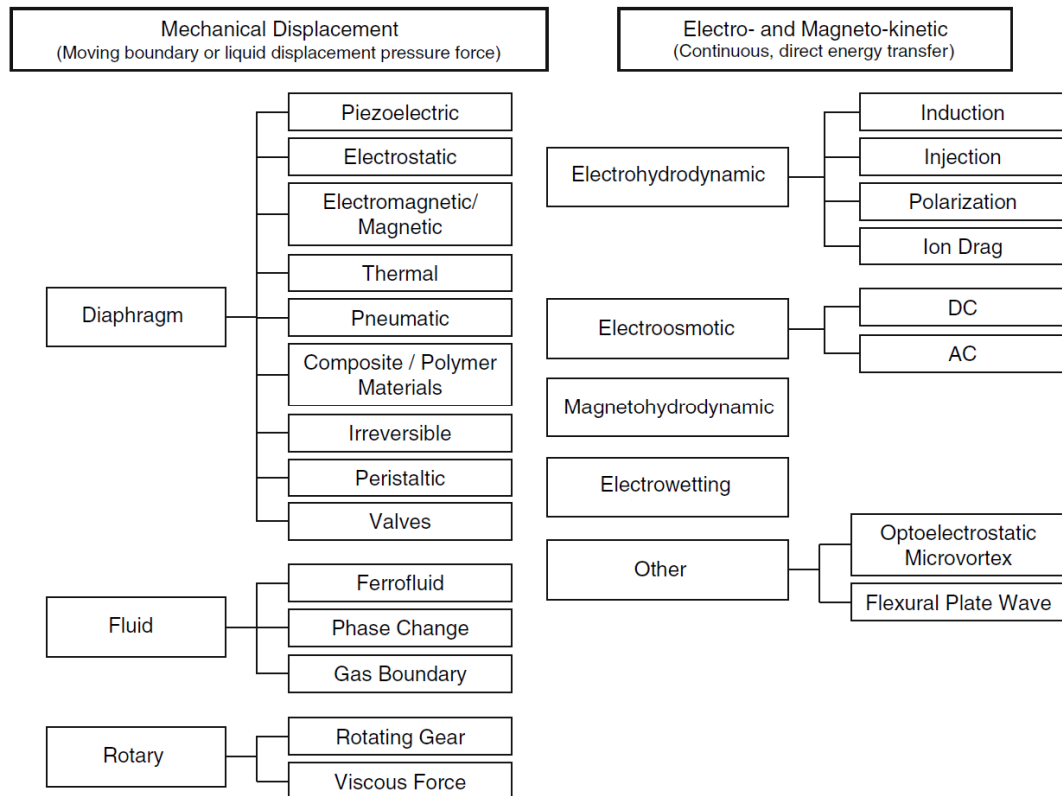


Figure 1.1. A categorised list of currently used fluid manipulation techniques. The figure was reprinted from [11]

The selection of the fluid pumping technique depends on the desired application. These may vary over a wide range: from low power, low flow-rate to high flow-rate, high pressure pumping. The techniques for micropumping can be broadly divided into 2 categories:

1. Mechanical displacement micropumps - defined as "those that exert oscillatory or rotational pressure forces on the working fluid through a moving solid-fluid (vibrating diaphragm, peristaltic, rotary pumps), or fluid-fluid boundary (ferrofluid, phase change, gas permeation pumps)" [11].
2. Electro- and magneto-kinetic micropumps - defined as "those that provide a direct energy transfer to pumping power and generate constant/steady flows due to the continuous addition of energy (electroosmotic, electrohydrodynamic, magnetohydrodynamic, electrowetting, etc.)"[11].

These categories can be further sub-divided according to actuation principles. A detailed analysis of the techniques as well as their applications can be found in literature [12, 13]. However, only some of these techniques are used to generate the fluid flow in microfluidic devices. Namely these techniques are [14]:

Gas boundary displacement - most commonly an external syringe or vacuum pump is connected to a microfluidic channel via an inlet/outlet. The pressure is applied to a syringe that contains either liquid or gas and is connected to a channel. As a result the motion of fluid is produced. Similarly, the liquid can be dragged from the reservoir using a vacuum pump by removing the gas from the channel.

Membrane actuated displacement - This system consists of a closed chamber with valves and a membrane made out of specialised material. Upon application of external source, the material undergoes the change which results in a force production. In case of thermal actuation, the volume of the material expands or stress is produced in response to external heat. Alternatively piezoelectric material can be used for membrane as this material undergoes the mechanical stress in presence of

the applied electric potential. Other types of membrane actuated displacement include electrostatic and electromagnetic mechanisms.

Ferrofluidics displacement - In this system ferrofluid is separated from the working fluid with an oil plug. The diagram of a simple ferrofluidic pump is shown in figure 1.2. The motion of the magnet produces the fluid flow from the inlet to outlet.

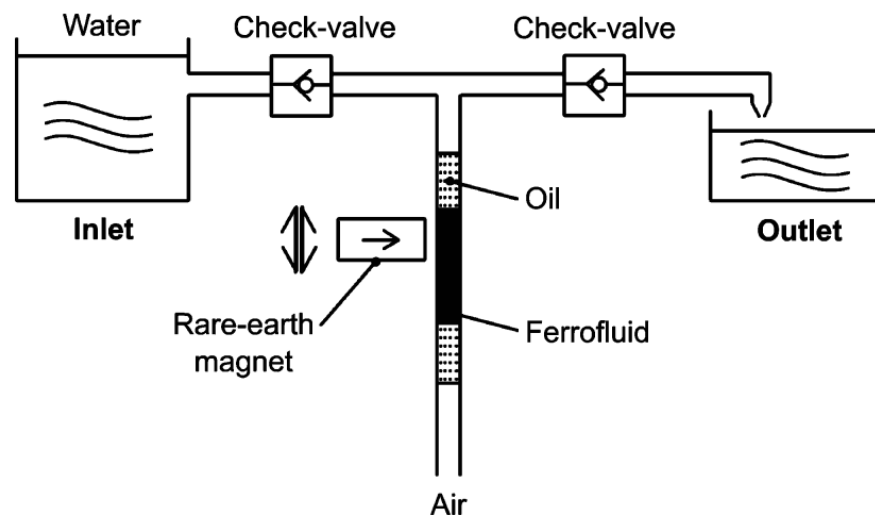


Figure 1.2. A schematic diagram of a ferrofluidic piston pump. The figure was reprinted from [15]

Other methods include the use of capillary force [16, 17] or gas bubbles [18] to produce the motion inside the channels. Alternatively to the techniques discussed so far, the pumping system can be integrated onto the chip itself. Some of these methods include electrohydrodynamic, magnetohydrodynamic and electroosmotic pumps.

According to a comparison of various pumping techniques in a recent comprehensive review [11], piezoelectric diaphragm pumps, induction- and injection-type electrohydrodynamic and electroosmotic pumps produce high flow

rates per unit area. In addition electroosmotic pumps offer great miniaturisation potential, which makes it favourable technique for microfluidic application.

1.2 Detection techniques

One of the detection techniques that is used in the microfluidic and lab-on-a-chip system is the optical detection. It is a very common detection method due to the ease of implementation [19]. Out of the number of optical detection methods, the fluorescence detection is the most popular method for the microfluidic devices due to the excellent sensitivity which is often required because of the small sample volume involved.

In fluorescence microscopy the specimen is illuminated by a light of a specific wavelength which is absorbed by fluorophores causing them to emit light of a different wavelength (i.e. of a different colour) than the absorbed light. The illumination and emission light is separated by the use of a spectral emission filter. Alternatively, charge couple device (CCD) cameras [20, 21] and photomultiplier tubes [22] (PMT) can also be used to detect the emitted fluorescent light. The equipment, required for the fluorescence detection is, however, very large, which constrains the portability of microfluidic devices. In addition only the natively fluorescent or are amendable to labelling analytes can be detected [23].

Another commonly used optical detection method is the ultraviolet-visible light (UV-Vis) absorbance detection. In this system when the emitted light passes through a sample, the molecules within the sample absorb the energy to move the electrons to

a different energy state. The detection is made according to the wavelength, required to promote the electron to a different state. The signal of such system is pathlength dependent and the small scale of the microfluidic devices severely minimises the sensitivity of the measurements on the chip [14]. In recent studies, the photothermal absorbance detection technique was presented [23, 24]. This technique relies on the physical changes (refractive index, viscosity and conductivity) in the solution that take place when an analyte absorbs the light of the excitation beam.

Other optical detection methods include surface plasmon resonance, where the frequency of the light photons matches the natural frequency of the surface electron oscillation, which is sensitive to the surface absorbed molecules and Raman spectroscopy. For microfluidic system, however, surface enhanced Raman spectroscopy [25, 26] is generally used due to the sensitivity limitation of the conventional analysis [27].

Another mechanism for detection is electrochemical detection. It has the potential to be compact and fully integrated as the signal is detected using the electrodes [28, 29]. The system can be used to detect the molecules that undergo oxidation or perform conductivity measurements [30, 31]. Recently mass spectrometry has been used in microfluidic systems for ultrasensitive analysis of microscale samples [32].

1.3 Object manipulation using electric fields

One of the main challenges for a practical application of a lab-on-a-chip device is to be able to manipulate objects on small scales. The manipulation mechanism has to be

compatible with the miniaturised portable system, highly reliable and easy to maintain. Among the large number of manipulation methods reported in literature [33], electrokinetic techniques are currently most favourable.

The electrokinetic techniques can be separated into two categories according to the type of signal that is applied: AC and DC electrokinetics. The list of the forces produced by the electric field that can be exerted on objects is given in table 1.1

Table 1.1 A summary of electrokinetic forces that can be exerted on objects in aqueous solution due to external electric field and the origin of the effect.

Force	DC	AC	Origin (Interaction of)
Electrophoresis	✓	×	Charge and the electric field
Dielectrophoresis	✓	✓	Induced dipole and non-uniform field
Electroosmosis	✓	✓	Charge in double layer and tangential field
Electrothermal flow	✓	✓	Gradients in permittivity and conductivity of the fluid and the electric field

A large number of studies have been carried out for both DC and AC electrokinetic effects. In the context of manipulation for lab-on-a-chip application, however, the preference has been given to AC effects for a number of reasons, such as the fact that the alternating fields significantly reduce electrolysis, prevent bubble formation, suppress electrochemical reaction and maintain the pH level at the interface between the electrode surface and the electrolyte [34, 35].

In a system with alternating electric fields, low voltages are generally applied over closely spaced microfabricated electrodes producing large electric fields. These fields are capable of directly moving the objects through an induced dipole and field interaction i.e. dielectrophoresis (DEP), traveling wave dielectrophoresis,

electrorotation and electroorientation, or indirectly by producing fluid motion via electroosmosis or electrothermal flow, which drags the object in the direction of the induced flow.

1.4 Applications

One of the most highly developed applications of microfluidic devices is their use for screening of protein crystallisation conditions (such as pH, ionic strength and composition and concentration) [36-38], as these devices offer a potential to screen a large number of conditions, minimise the damage to crystals and separate the nucleation and growth [10].

Considering the small sample volumes and no need for an expert to operate them, these devices look very appealing for diagnostics [39-43]. Low weights makes it portable and so it can be used directly at sites where samples are taken which results in the short time frames for the results to be obtained with less chance of contamination. The mass production would also enable low cost which is particularly important for the third world countries where buying the expensive specialised equipment for laboratory tests may not be possible.

A particularly important contribution in the development of microfluidic devices is the polydimethylsiloxane (PDMS) material. It is a transparent elastomer with low toxicity and high permeability to dioxygen and carbon dioxide. In cell biology PDMS microfluidic system can be used in a wide range of studies such as

cytoskeleton [44, 45], the contents of cell (down to single-cell level) [46-49] as well as separation of motile and non-motile cells (e.g. sperm [50]).

In addition, PDMS-based microfluidic devices can be used to perform a range of studies on the bacteria. For example, the studies of macro-scale flow of bacterial biofilms (groups of microorganisms in which cells stick to each other on the surface) are conventionally conducted in a low-throughput environment, generally require large volumes of sample and do not allow spatial and temporal control of biofilm community formation [51]. The mentioned devices help to overcome the problems associated with these studies. Additional benefits of microfluidic based bacterial biofilms investigation are the control of the hydrodynamic conditions, real time monitoring and the ability to establish stable chemical gradients [52-55]. These devices are also used for other applications, such as exploring the bacterial microenvironments [56] as well as the separation [57-60] and detection [61-67] of the bacteria.

The integration of protein molecular motors into a microfluidic system is another line of research which has been heavily investigated by means of the *in vitro* motility assay [68-73]. These motors convert chemical energy (ATP) into mechanical work in a very energy efficient manner and are naturally “designed” for cargo transportation without the need of induced fluid flow. Moreover the proteins that are sliding above the motor covered surface in a typical experiment are extremely small (the radius of actin filament and microtubule are only few nanometers) which is beneficial when building devices of micron and sub-micron scale.

1.5 Thesis outline and authors contribution

The aim of this thesis is to explore the capabilities of currently used electrokinetic techniques for a practical microfluidic device. Through a set of experiments aided by numerical simulations a theoretical framework has been developed that could be of critical importance when designing a device for bacterial analysis and/or uses protein molecular motors.

The complete dissertation consists of the following major sections:

chapter I serves as an introduction to the background and the motivation of this work. The theoretical background of the electrokinetic techniques used for the object manipulation is presented in chapter II.

Small distance between electrodes enables application of high electric fields at low voltages. Using the laser ablation technique the electrodes can be fabricated as shown in chapter III. Also presented is the microfluidic channel fabrication procedure and surface topography imaging using the atomic force microscope.

One of the commonly used techniques for object manipulation on microscale is dielectrophoresis. The force, associated with this phenomenon depends on the properties of both particle and the medium. In chapter IV a mechanism for a novel object characterisation using amplitude modulated dielectrophoresis is developed.

Authors Contribution to the amplitude modulated dielectrophoresis chapter is the following: I have designed and performed a range of experiments using the square-wave modulated input signal applied to castellated electrodes as well as quantitatively analysed the effect of changing the frequency and duty cycle of the

square wave. Developed an image processing tool using Matlab software for fluorescence intensity (quantitative) analysis of the cyclic collection-diffusion behaviour. Performed an experiment to determine the relationship between the fluorescence intensity and particle number for 512 nm and 1 μm particles.

A systematic study of various electrokinetic techniques is presented in chapter V. The techniques were used to manipulate the *Pseudomonas Fluorescence* bacteria in microfluidic channels. These spatially restricted channels resemble the geometrically confined natural habitat of the bacteria.

Authors contribution to this chapter included design of experimental setup for AC and DC electric field manipulation. More specifically a fabrication of the "needle" device for DC analysis as well as performing the experiments on the bacteria in such device. Experimental investigation of DEP and ACEO effect on motile and non-motile bacteria. Fabrication of the gold ablated electrodes and PDMS channel (as discussed in the fabrication chapter) for ACEO and ACET analysis. I have also developed numerical simulations using Comsol software to:

- Minimise the experimental setup used for DC analysis to dimensions typical to microfluidic system
- Compare the experimentally observed motion of the bacteria influenced by ACET and the simulation produced streamlines
- Design the channel geometry that allows producing a unidirectional flow using the PDMS topography

In addition the heat map of the bacteria motion inside the Venice waterways was produced using the Matlab software.

In chapter VI the experimental setup to manipulate negatively charged protein molecular motors is developed. This setup allows the application of relatively large electric fields without producing bubbles and free radicals that are harmful for the proteins. Also presented is the numerical simulation that uses the experimentally obtained results to gain more insight on the protein-surface and motor-filament interaction.

Authors contribution to this chapter was the development of the numerical simulation that allows calculating the number of motors on the surface as well as determine the active and resistive force of motors that interact with the filament. The author has also developed a method of calculating the number of lever arms that can interact with the filament for a given number of motors on the surface. I have also assisted on performing the electrical motility experiments and determining the ratio of active and inactive motors.

Chapter II: Theory. Forces acting on objects in the electric field

This chapter gives a theoretical background to various electrokinetic techniques that are used to manipulate objects suspended in aqueous solutions. More specific these manipulation methods are electrophoresis, dielectrophoresis, AC elektroosmosis and AC electrothermal flow.

2.1 Electrophoresis

Electrophoresis is commonly referred to as the steady transition of a particle under the influence of a spatially uniform electric field [74-76]. This phenomenon was first described by Reuss in a paper published in 1809 [77]. Reuss has noticed that the application of the electric field caused clay particles suspended in water to migrate. However, it would take almost 100 years to explain the underlying principles of the phenomenon [78]. It is currently known that the electrokinetic properties of a particle in suspension are governed by the electric charge distribution in the double layer that surrounds the particle [79, 80]. The formation of this double layer takes place when a solid particle that carries a surface charge suspended in a liquid becomes surrounded by counter-ions (of opposite charge to that of the surface of the particle). As the particles move through the solution, the plane beyond which the counter-ions do not migrate along with the particle is known as the slipping plane. The electric potential at the slipping plane is known as the zeta potential ζ .

The term that describes the rate of particle motion under the electric field is the electrophoretic mobility, μ .

$$\mu = \frac{v}{E}, \quad (2.1)$$

where v is the velocity and E is the electric field strength. The electrophoretic mobility is also dependent on zeta potential. Assuming that the thickness of the double layer is negligible in comparison with the particle diameter, the expression for the electrophoretic mobility is given by equation 2.2

$$\mu = \frac{\varepsilon_0 \varepsilon_r \zeta}{\eta} . \quad (2.2)$$

Here ε_0 is the permittivity of free space, ε_r and η are the permittivity and viscosity of the suspending medium, respectively. ζ is the zeta potential of the suspended particle.

Electrophoresis is currently a common technique for molecule separation. Few of the many applications include DNA, protein, antibiotics and vaccine analysis. Various types of electrophoretic setups are currently used, however most commonly gel medium (Electrofocusing gels, DNA agarose gels, DNA denaturing polyacrylamide gels, etc.) is used for the separation.

2.2 Dielectrophoresis

The term dielectrophoresis commonly refers to a micro to nanoscale manipulation technique which takes place due to the interaction of a non-uniform electric field with the induced dipole of an object, suspended in the solution. Pohl [81] was one of the first to recognise and explore the applications of the force that this system experiences. This force strongly depends on the gradient of the electric field, thus on the distance between electrodes. His early work to observe the effect of DEP generally involved needles, wires and flat surfaces to generate inhomogeneous electric fields [81, 82], however, the forces generated in these studies were relatively small and presented results received little attention. With the advance of microfabrication techniques, larger electric fields could be produced, re-igniting the interest in this area. Currently DEP theory is well established (the summary can be

seen in a recent review by one of the pioneers in the area [83]) and a number of analytical and numerical approaches have been presented [84-88]. DEP force is routinely used in a whole range of applications presented in a comprehensive review [83] with over 950 journal papers published in the last 5 years. Different electrode geometries are used to investigate conventional dielectrophoretic behaviour [89-94] and more recently insulator-based [95, 96] and contactless techniques [97] have been developed.

2.2.1 Dielectric spheres in an electric field

In order to explain how force, acting on an object in a non-uniform electric field is produced, it is essential to analyse the charge distribution at the interface between two materials of different conductivity and/or permittivity. Conductivity is a measure of the ease with which charge can move through a material, while permittivity describes the amount of electrical energy (or charge accumulation at the interface) stored in a material. In a DEP system, these two materials are a particle (which in reality can be a latex bead, a cell, a virus, bacteria or a protein molecule) and an aqueous solution [35].

Dielectric materials ideally have no free charge and all electrons are bound to the nearest atom or molecule. They exist in two types: polar dielectrics and non-polar ones. When the electric field is applied, bound charges are forced to move slightly with positive and negative charges moving in opposite directions. The charge distribution around a particle can be described by introducing a concept of Polarisability, which is a measure of the ability of a material to respond to a field

(polarise) and produce charge at the interface. It can be otherwise described as the ability of a material to acquire a dipole through the action of an external electric field.

There are three basic molecular polarisation mechanisms that can occur when an external electric field is applied to a homogeneous dielectric: Electronic, atomic and orientation (or dipolar). Electronic polarisation is present in both polar and non-polar materials when the electric field acts on electrons and nucleus of an atom, distorting the electron orbitals such that their average position does not coincide with nucleus. Atomic polarisation takes place within the material when differently charged ions are displaced. Polar dielectrics contain atoms (or molecules) that possess a permanent dipole moment (randomly oriented). Alignment of these permanent dipoles is called orientational polarisation.

Real systems are often heterogeneous (i.e. consist of a number of different dielectrics each with its properties). For such systems, when an electric field is applied, surface charge accumulates at the interface between different dielectrics. This is referred to as interfacial or Maxwell-Wagner polarisation.

In a dielectrophoretic system that is used in these studies, when an electric field is applied, the interface between the particle and the suspending medium undergoes the Maxwell-Wagner polarisation.

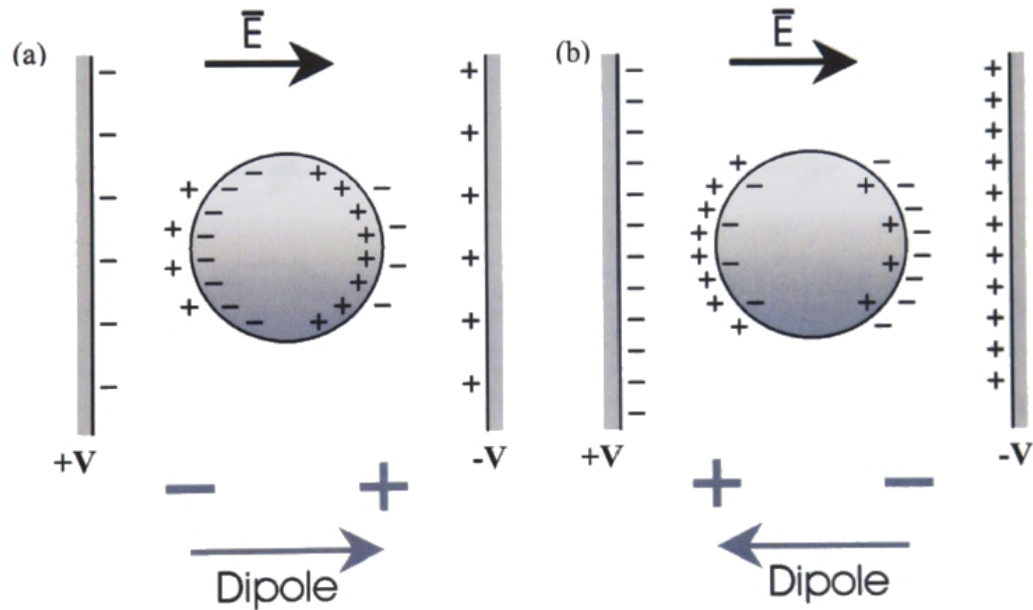


Figure 2.1. Effect of uniform electric field on uncharged particle. The polarisability of particle is greater (a) and less (b) than that of the suspending medium. Figure was adapted from [35]

Consider the case, where a spherical particle is suspended in an electrolyte and subjected to a uniform electric field. A charged particle will experience a net force towards the electrode of opposite polarity through electrostatic force or Coulomb interaction. A neutral particle will become polarised as a result of the electric field, but will not experience any net force. Depending on the polarisability of the particle and medium, the net induced dipole can have different direction. When the polarisability of the particle is greater than the electrolyte, there are more charges just inside the interface rather than outside (figure 2.1a). The difference in charge density gives rise to an effective (induced) dipole across the particle aligned with the field. For a medium with polarisable larger than that of a particle, the direction of induced dipole is reversed (figure 2.1b). Equal polarisability of a particle and medium results in zero effective dipole.

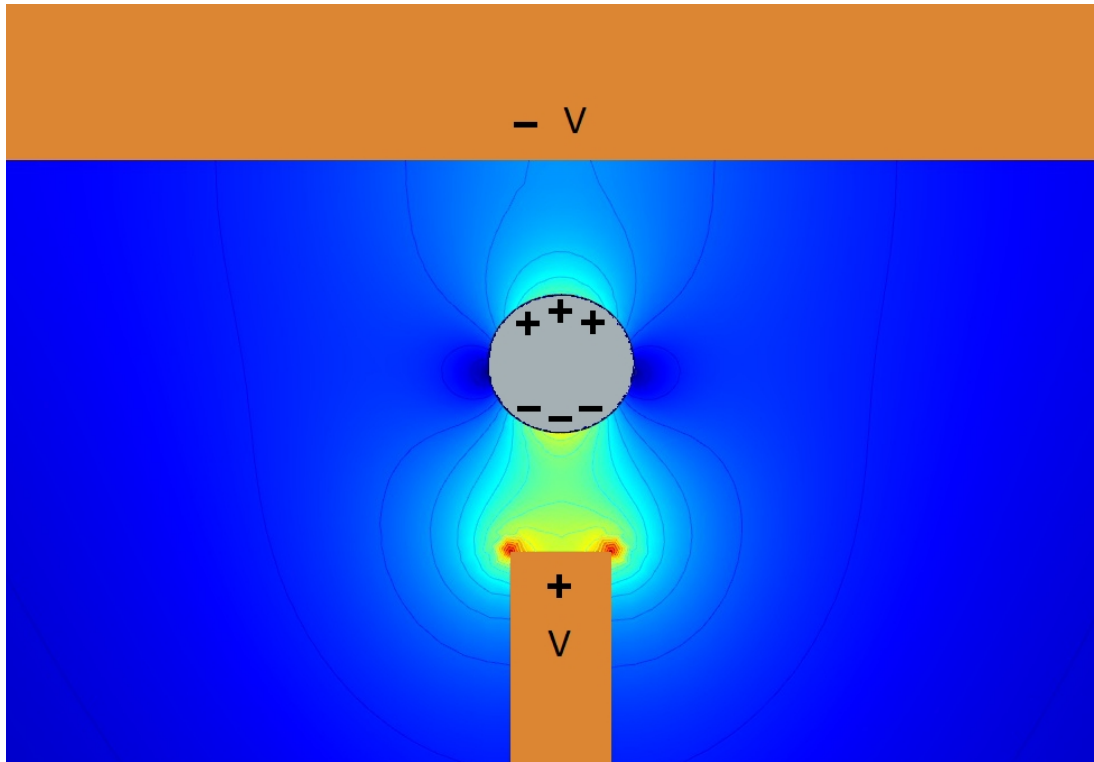


Figure 2.2. Simulated non-uniform electric field displays different field strength acting on the same particle. This imbalance leads to a force – dielectrophoretic force.

When placed in a non-uniform DC electric field a charged particle will still experience the force toward the electrode of opposite polarity. However a neutral particle will experience a force, moving it away or towards the regions of high electric field intensity. The reason for this force is the following: charge distribution at the interface may be considered of equal amounts towards $+V$ and $-V$ as shown in figure 2.1. However the field line density is different which leads to different field strengths on one side of the particle than the other (illustrated in figure 2.2) and as a result an imbalance of forces on the induced dipole, leading to particle movement. This effect is called dielectrophoresis.

The formation and/or orientation of a dipole does not occur instantaneously. By reversing the polarity of electrodes in figure 2.2, the resulting charge distribution of a

sphere would also change. This redistribution takes some time and clearly if the frequency, at which the polarity of electrodes is reversed, is continuously increased at a certain point the motion of the charge will no longer be able to keep up with the pace of the field and polarisation no longer occurs.

2.2.2 Frequency dependent behaviour of DEP force

The complex permittivity describes the frequency dependent response of the dielectric particle to an applied electric field [98] and is given by

$$\tilde{\epsilon} = \epsilon_0 \epsilon_r - j \frac{\sigma}{\omega}, \quad (2.3)$$

where ϵ_0 is absolute permittivity of vacuum, ϵ_r is the relative permittivity of the dielectric, σ is the conductivity and ω is the angular frequency, $2\pi f$. From the above discussion (2.2.1) it becomes apparent that a homogeneous dielectric sphere, suspended in homogeneous dielectric medium will experience interfacial polarisation. The effective dipole moment (derived in [99]) in this case is given by

$$p = 4\pi\epsilon_m \left(\frac{\tilde{\epsilon}_p - \tilde{\epsilon}_m}{\tilde{\epsilon}_p + 2\tilde{\epsilon}_m} \right) r^3 E, \quad (2.4)$$

here ϵ_m is the permittivity of the suspending medium (i.e. fluid), ϵ_p is the permittivity of the particle, r is the radius of the particle, and E is the electric field strength. The term in brackets is called the Clausius-Mossotti factor, f_{CM} , for a spherical particle. The force, acting on the induced dipole is further derived in [35] and the result is:

$$F_{DEP} = (p \cdot \nabla)E, \quad (2.5)$$

and the full equation of time-averaged DEP force on a spherical particle is given by

$$\langle F_{DEP} \rangle = 2\pi r^3 \varepsilon_m \text{Re}\{f_{CM}\} \nabla |E|^2. \quad (2.6)$$

The variation of magnitude and direction of the force is determined by the real part of f_{CM} which depends on the conductivity and permittivity of the particle and the surrounding medium. When analysing the particle conductivity, it is important to consider the effect that the surface charge has on the dielectric response. For example it has been noted that the latex particle (which has the bulk conductivity of the order of 10^{-16} S/m) exhibited anomalously high values of internal conductivity. This anomaly is explained by the fact that the total particle conductivity attributed to the surface charge movement is determined using the following equation [100]:

$$\sigma_p = \sigma_{bulk} + \frac{2K_s}{r}, \quad (2.7)$$

where σ_p and σ_{bulk} are the respective particle and bulk conductivities, K_s is the surface conductivity (for a spherical latex particle $K_s \approx 10^{-9}$ S [100]) and r is the radius of a sphere.

The Clausius-Mossotti factor is calculated in a Matlab program (program code is similar to [100]) for a sphere with a diameter of 1 μm , conductivity of $\sigma_p = 0.04$ S/m, permittivity ε_p of $2.5\varepsilon_0$ ($\varepsilon_0 = 8.85 \times 10^{-12}$ F/m), suspended in a medium with ε_m of $80\varepsilon_0$ and three different conductivities σ_m of 1×10^{-3} ; 0.04 and 0.1 S/m. The result is displayed in figure 2.3. When the real part of f_{CM} is positive, the particle is attracted to a region of high electric field and this attracting force is called positive dielectrophoresis (pDEP). At a negative value the particles are repelled from that

region experiencing negative Dielectrophoretic force (nDEP). A transition point of zero value is termed a crossover frequency. No net force is exerted on particle in this case.

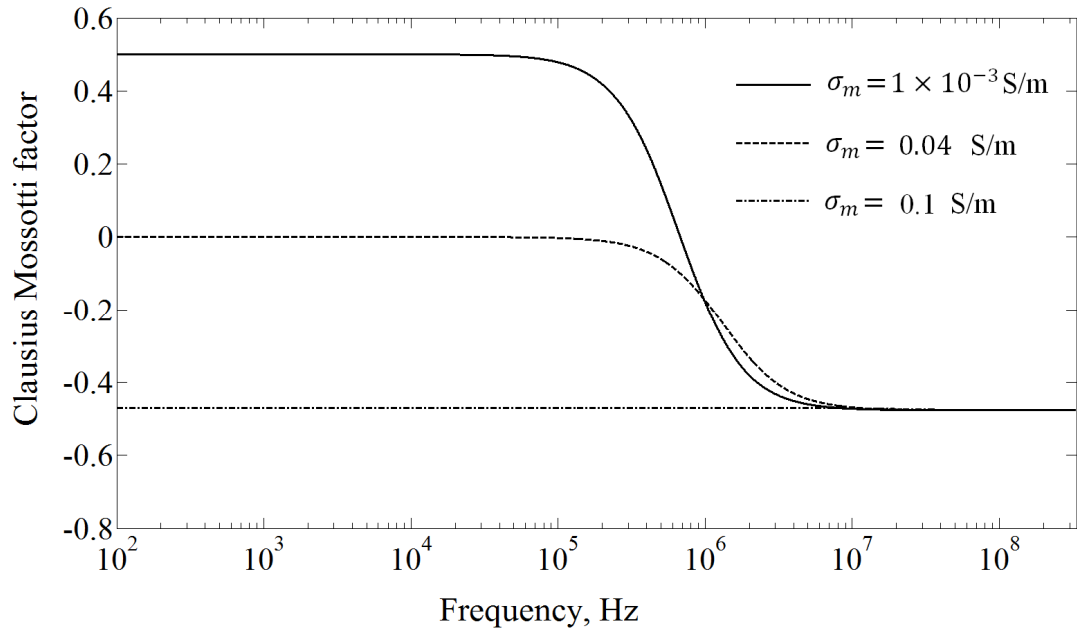


Figure 2.3. Plot of real part of f_{CM} as a function of frequency at different medium conductivities

2.2.3 DEP of non-spherical particles

So far the polarisability of a sphere with a very simple internal structure has been considered. Biological particles, such as cells, viruses and bacteria have a more complex structure which is generally modelled as multi-shell system. For sphere-like biological particles concentric shells, each having its own electric properties, are used.

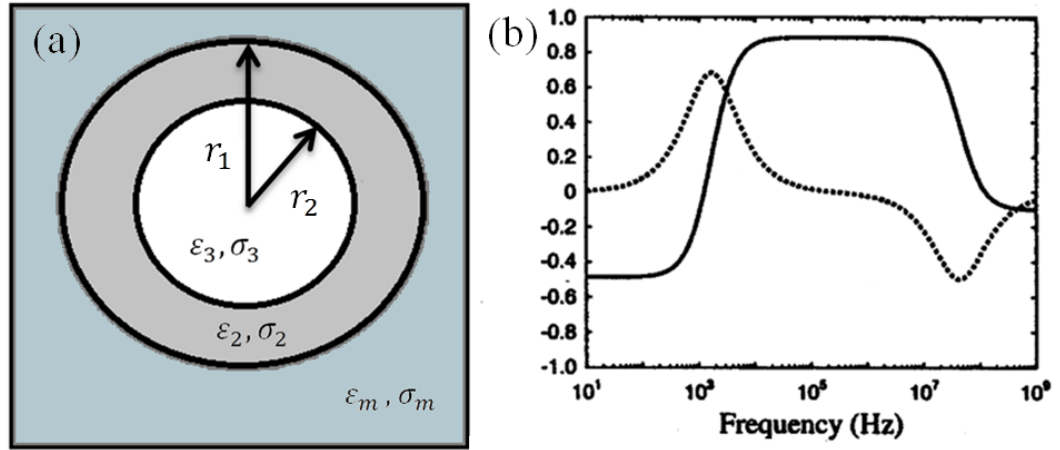


Figure 2.4. (a) Schematic of a spherical particle with a single shell. (b) The frequency variation of the equivalent Clausius-Mossotti factor with $r_1 = 2.01 \times 10^{-6}$ m, $r_2 = 2.0 \times 10^{-6}$ m, $\epsilon_m = 78.5\epsilon_0$, $\epsilon_2 = 10\epsilon_0$, $\epsilon_3 = 60\epsilon_0$, $\sigma_m = 10^{-4}$ Sm $^{-1}$, $\sigma_2 = 10^{-8}$ Sm $^{-1}$, $\sigma_3 = 0.5$ Sm $^{-1}$. (a) was re-drawn and (b) re-printed from [35]

The simplest example is that of a single shell particle e.g. red blood cell is schematically shown in figure 2.4. This system has 2 different types of materials which respond differently to an external electric field. The polarisability $\tilde{\alpha}$ is given by

$$\tilde{\alpha} = 3\epsilon_m \left(\frac{\tilde{\epsilon}_{23} - \tilde{\epsilon}_m}{\tilde{\epsilon}_{23} + 2\tilde{\epsilon}_m} \right), \quad (2.8)$$

and the complex permittivity of the particle $\tilde{\epsilon}_{23}$, is given by

$$\tilde{\epsilon}_{23} = \tilde{\epsilon}_2 \left[\frac{\gamma_{12}^3 + 2 \left(\frac{\tilde{\epsilon}_3 - \tilde{\epsilon}_2}{\tilde{\epsilon}_3 + 2\tilde{\epsilon}_2} \right)}{\gamma_{12}^3 - \left(\frac{\tilde{\epsilon}_3 - \tilde{\epsilon}_2}{\tilde{\epsilon}_3 + 2\tilde{\epsilon}_2} \right)} \right], \quad (2.9)$$

with $\gamma_{12} = \frac{r_1}{r_2}$.

More shells can be adopted to mimic more complicated systems say cell membrane, nucleus and cytoplasm of animal cell. However, not all microorganisms have sphere-like structure. In fact their geometry can be very diverse.

2.2.4 DEP of rod-shaped bacteria

Throughout this work the rod-shaped bacteria and proteins were used so it is sufficient to show the DEP force, derived for a prolonged ellipsoid [101, 102] whose major axis is parallel to the electric field:

$$\langle F_{DEP} \rangle = 2\pi \frac{r_x r_y r_z}{3} \varepsilon_m \operatorname{Re} \left\{ \frac{\tilde{\varepsilon}_p - \tilde{\varepsilon}_m}{[\tilde{\varepsilon}_m + (\tilde{\varepsilon}_p - \tilde{\varepsilon}_m) \times R_x]} \right\} \nabla |E|^2, \quad (2.10)$$

where r_x , r_y and r_z ($r_y = r_z$) are the lengths of major and minor axes. R_x is the “depolarising factor” along the major axis r_x and is given by:

$$R_x = \frac{r_y^2}{2r_x^2 e^3} \left[\left(\ln \frac{1+e}{1-e} \right) - 2e \right], \quad (2.11)$$

and e is the particle eccentricity

$$e = \sqrt{1 - \frac{r_y^2}{r_x^2}}. \quad (2.12)$$

Using the equations 2.10-2.12 the effective Clausius Mossotti factor was calculated for a *Pseudomonas putida* bacteria with the conductivity of 20 mS/m [103, 104] in the media that supports the bacteria growth (more detail in section 5.3.2) with conductivity of 16.4 mS/m and distilled water with conductivity of 15.6 μ S/m. It was

previously determined that as the bacteria cell dies, the effective conductivity of the cell increases and as a result selective trapping of dead and alive bacteria by dielectrophoretic force is observed [105].

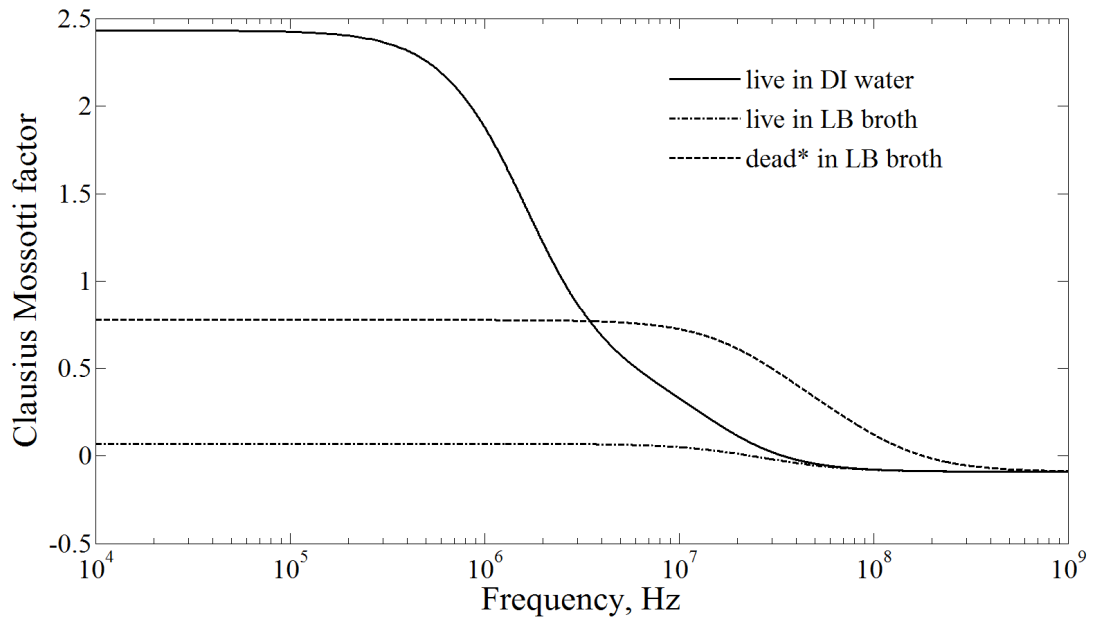


Figure 2.5 The Claussius Mossoti factor, calculated for a no shell model. The dead* bacteria represents the conductivity, 5 times larger than the live bacteria cell (100 mS/m) and the simulation was performed using the value of relative permittivity of 60 (similar to a mammalian cell [106]). These values were used for illustration purpose as exact values were not available.

The no-shell system in figure 2.5 suggests that the relatively weak positive dielectrophoretic effect is present at frequencies up to tens of MHz range (Clausius Mossoti factor at these frequencies is 0.07). However, provided that the changes in the cell conductivity once the cell dies will significantly increase, stronger positive DEP effect at the same applied signal could be noted.

In other studies, where the shell model has been used, it was suggested that the conductivity of the *e. coli* bacterial cell membrane increases by 4 orders of magnitude as the bacteria dies [107]. Assuming that the conductivity data of the bacteria, used for the experiments, is similar to the *e.coli* bacteria, the simulation of a

two-shell model was performed as discussed in [101] and the result is shown in figure 2.6. The conductivity of medium was 16.4 mS/m and the relative permittivity of the cytoplasm, cell membrane, cell wall and the medium were 60, 10, 60 and 80 respectively.

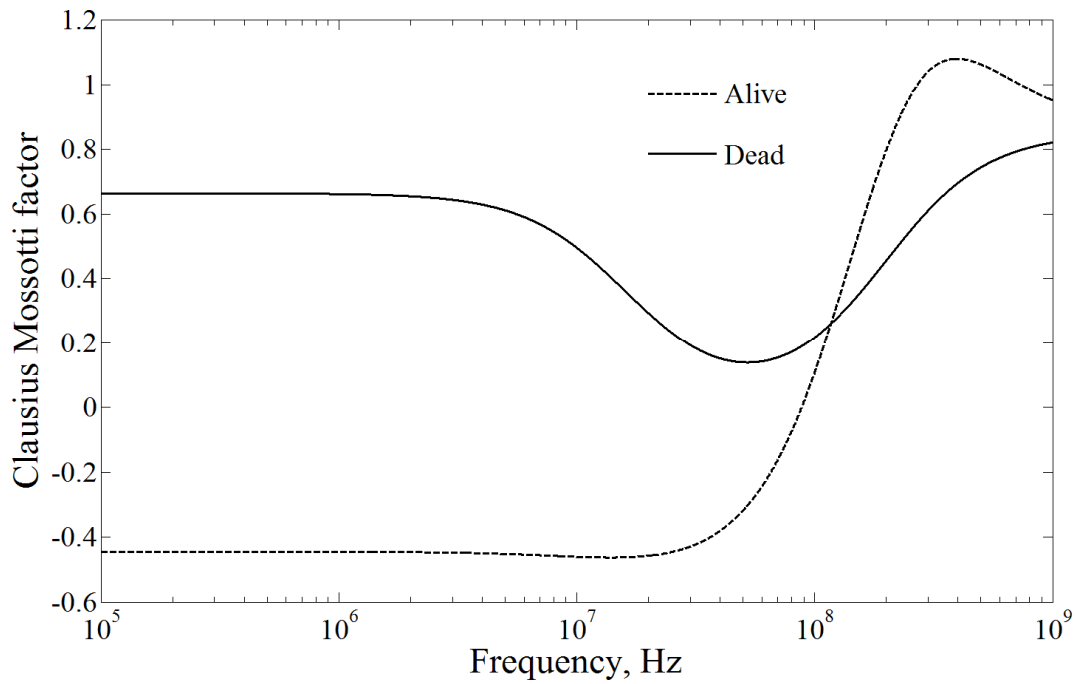


Figure 2.6 The Clausius Mossotti factor calculated for a 2 shell model of dead and alive bacteria. See text for more details.

The two shell simulation was developed for a bacterial cell with a cytoplasm, membrane and cell wall. The values of permittivity for dead and alive cell were kept constant [108]. The conductivity values for the live bacteria were used similar to the data of *e.coli* [101]: $\sigma_{\text{cytoplasm}} = 0.5 \text{ S/m}$, $\sigma_{\text{membrane}} = 10^{-6} \text{ S/m}$ and $\sigma_{\text{wall}} = 5 \times 10^{-3} \text{ S/m}$. It was further assumed that as the cell dies, the conductivity of the cytoplasm decreases (provided that the conductivity of the medium is lower). The simulation of the Clausius Mossoti factor for the dead bacteria was performed using $\sigma_{\text{cytoplasm}} = 3 \times 10^{-2} \text{ S/m}$, $\sigma_{\text{membrane}} = 10^{-2} \text{ S/m}$ and $\sigma_{\text{wall}} = 5 \times 10^{-3} \text{ S/m}$. These values were used for illustration purpose and an exact model would require a

more sophisticated shell system with accurate conductivity and permittivity measurements of live and dead bacterial cell.

In contrast to a no-shell model, figure 2.6 suggests a possible transition between the negative dielectrophoretic effect for a live cell to a positive dielectrophoresis for a dead one similar to the data reported in [109].

2.3 AC Electroosmosis

As discussed for dielectrophoresis, when an electric field is applied, a double layer is formed at the interface of the particle and the suspending medium. For such a system it is also important to analyse the behaviour of the free charges at the electrode edges. When coming in contact with the free ions in fluid, (this could be electrolyte or a dielectric fluid with ionic impurities) charged electrodes attract counterions from the bulk to establish charge neutrality. As a result the density of the counterions in the solution right at the interface with the electrodes is higher than in the bulk. Helmholtz was the first to propose the concept of an electrical double layer forming between the electrode and the electrolyte [110]. In his model he assumed that all counterions are absorbed at the surface of the electrode, which can be treated as a parallel plate capacitor separated by a specific distance. Realising that the ions in the solution are mobile, Gouy and Chapman have re-designed the model where ions were treated as point charges [111, 112]. The result was a so called diffusive layer model. Stern has combined the two models, describing the double layer as two layers: the first layer contains strongly bound immobile ions and the second diffusive layer with mobile ions to which the Gouy-Chapman model applies [113]. More

details on the current understanding of the double layer can be found in literature [35, 75].

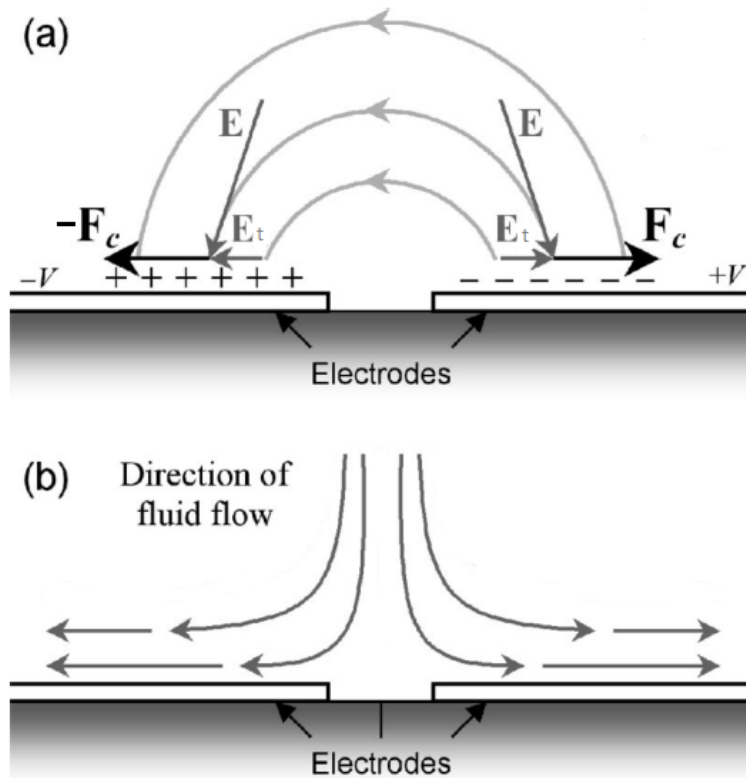


Figure 2.5. A schematic diagram representing the mechanism of AC Electroosmosis. (a) shows the charge layer around electrodes, electric field between two electrodes and its tangential component E_t . Induced charge experiences a force F_c due to E_t . (b) The interaction of E_t and charge within the double layer results in fluid motion. The figure was adapted from [35].

In the case of a constant electric field, the double layer forms according to the amount of charge at the electrode surface and the free ions in the solution. For an alternating field the formation of a double layer becomes more complicated. The ions in the solution have to keep up with the charges produced on the electrodes. At a certain frequency free ions will no longer be able to respond to the oscillations of the field, resulting in the absence of the effect of electrode polarisation at high frequencies.

However, when the double layer is present, the electric field tangential to the surface of the electrode can act on the mobile ions inside the double layer moving them in the direction of the field (illustrated in figure 2.5). As a result the fluid is dragged along by the ions and this motion is termed Electroosmotic flow. The AC analogue of Electroosmosis has been demonstrated and theoretical work developed using finger electrodes [114-118].

Even though AC Electroosmosis (ACEO) is effective even at relatively large distances from electrodes (compared to DEP) it is generally restricted to a low range of frequencies and low conductivity media as shown in figure 2.6.

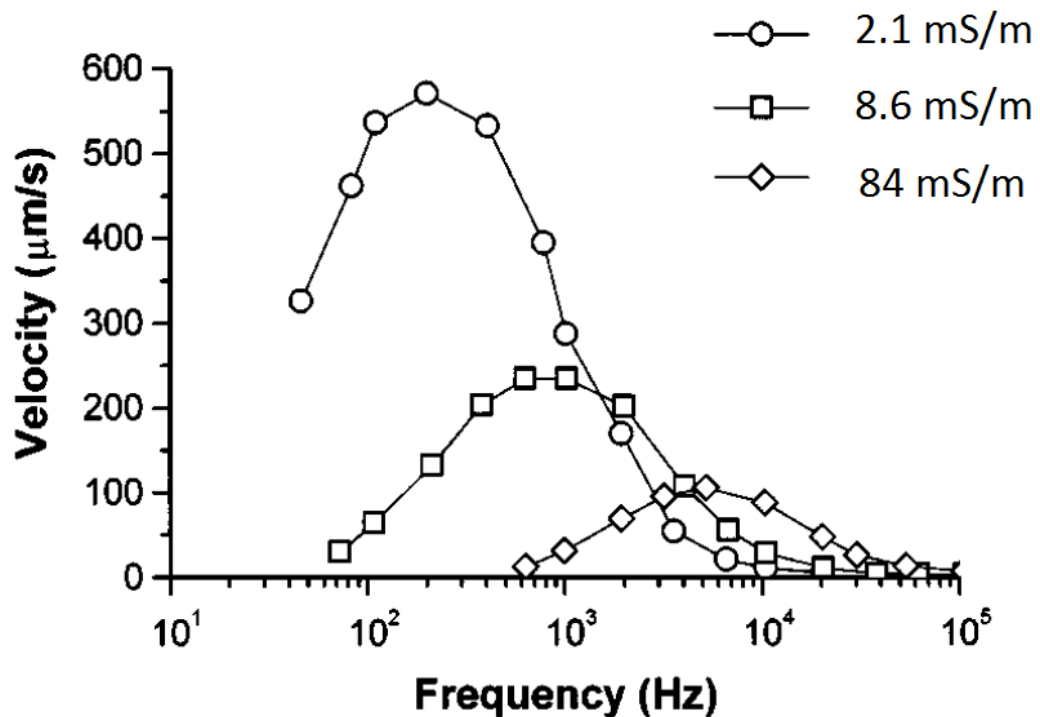


Figure 2.6. The velocity profile of a spherical particle observed 10 μm away from the electrodes for different media conductivities. As the conductivity increases, the magnitude of the fluid flow decreases. At high frequencies no ACEO is observed. The figure was reprinted from [117].

The peak velocity is shifted towards higher frequencies for higher medium conductivities and no ACEO is observed at 100 kHz or higher (figure 2.6).

2.4 AC electrothermal fluid flow

The electrokinetic technique that dominates at high frequency and in high conductivity media is electrothermal flow (ACET). It is produced by the non-uniform electric field, which causes power dissipation in the fluid – Joule heating. The amount of energy dissipated in the system is given by

$$\langle W \rangle = \frac{1}{2} \langle \sigma E^2 \rangle, \quad (2.13)$$

where σ is the conductivity of the electrolyte. The produced heat (also non-uniform) diffuses through the system producing gradients in permittivity and conductivity. Consequently, a force is generated as the electric field now acts on these gradients [119]. In addition it has been shown that external light sources (e.g. observing the sample using the fluorescent microscope), at low voltages can play an important role for the resulting fluid flow [120] in the system with closely spaced electrodes.

As already mentioned, ACET is efficient in a high conductivity medium, which makes it useful for manipulating biological specimen in their natural environment. This technique has a short history since it was introduced in 1990's with the majority of studies focusing on its ability to act like a pump with functional dimension in micrometre range to induce directed motion [121-124] or mixing [125, 126] of fluids.

2.4.1 The force on the fluid in electric field due to Joule heating

In order to derive the force, acting on the fluid, the electric field that produces the Joule heating has to be discussed first. In the small temperature gradient (STG) approximation the electric field can be determined by solving Laplace's equation [35]:

$$\nabla^2 \tilde{\phi} = 0, \quad (2.14)$$

where $\tilde{\phi}$ is the potential phasor which is given by a real and an imaginary part $\tilde{\phi} = \phi_R + i\phi_I$. For a two-dimensional situation with an electrode length larger than the width and ignoring the imaginary part [84] the electric field can be derived from

$$E = -\nabla\phi. \quad (2.15)$$

For high conductivity media and high applied voltages the small temperature approximation is no longer accurate and an enhanced model that uses electrical thermal coupling and temperature dependent expression for the electrical conductivity and dynamic viscosity has recently been developed [127]. Substantial differences between the results of the enhanced model and STG were observed when the temperature increases by more than 5 °C, which was not achieved in our system. Therefore in the rest of this thesis the small temperature gradient approximation has been used.

In order to find the changes in the temperature, it is necessary to solve the energy balance equation. This has been shown to reduce to a heat diffusion equation [114]:

$$k\nabla^2 T + \frac{1}{2}\langle\sigma E^2\rangle = 0, \quad (2.16)$$

where k is thermal conductivity. Finally, when both field and temperature profiles are determined, the force produced due to Joule heating in a non-uniform electric field can be calculated. The general expression of the electric body force is given by [35]

$$f_e = \rho E - \frac{1}{2}|E|^2 \nabla \varepsilon + \frac{1}{2} \nabla \left(\rho_m \left(\frac{\partial \varepsilon}{\partial \rho_m} \right) |E|^2 \right), \quad (2.17)$$

ρ and ρ_m are the charge and mass densities respectively. The right hand side consists of Coulomb force, dielectric force and electrostriction pressure; the latter can be ignored for an incompressible fluid.

When relative changes in permittivity and conductivity are small, the changes in charge density and electric field are also small and the electric field can be expressed as a sum of an applied field E_0 and a perturbation field E_1

$$E = E_0 + E_1, \quad (2.18)$$

with $|E_1| \ll |E_0|$. According to Gauss's Law for inhomogeneous media [128], the charge density is given by

$$\rho = \nabla \cdot (\varepsilon E). \quad (2.19)$$

Substituting (2.18) and (2.19) into (2.17) the expression for electrical body force becomes

$$f_e = (\nabla \varepsilon \cdot E_0 + \varepsilon \nabla \cdot E_1) E_0 - \frac{1}{2} |E|^2 \nabla \varepsilon. \quad (2.19)$$

By further applying the charge conservation equation while neglecting the convection current and the time varying harmonic signal of a single frequency [35] the expression for the perturbation field can be expressed as

$$\nabla \cdot E_1 = \frac{-(\nabla\sigma + i\omega\nabla\varepsilon) \cdot E_0}{\sigma + i\omega\varepsilon}. \quad (2.21)$$

Combining (2.20) and (2.21) gives the body force in fluid produced by the electric field

$$\langle f_e \rangle = \frac{1}{2} Re \left[\left(\frac{(\sigma\nabla\varepsilon - \varepsilon\nabla\sigma) \cdot E_0}{\sigma + i\omega\varepsilon} \right) E_0^* - \frac{1}{2} |E_0|^2 \nabla\varepsilon \right]. \quad (2.22)$$

This force is frequency dependent. At low frequencies the Coulomb force is larger (first term in square brackets) than the dielectric force (second term on the right hand side of the equation 2.22) which dominates at high frequencies. It has been shown in [114] that the conductivity and permittivity gradients can be expressed in terms of temperature gradients. For a typical aqueous electrolyte [129] those expressions are:

$$\begin{aligned} \nabla\varepsilon &= \left(\frac{\partial\varepsilon}{\partial T} \right) \nabla T; \quad \frac{1}{\varepsilon} \left(\frac{\partial\varepsilon}{\partial T} \right) = -0.004 \\ \nabla\sigma &= \left(\frac{\partial\sigma}{\partial T} \right) \nabla T; \quad \frac{1}{\sigma} \left(\frac{\partial\sigma}{\partial T} \right) = 0.02 \end{aligned}, \quad (2.23)$$

substituting the conductivity and permittivity gradient expression into (2.22), multiplying the part that represents the Coulomb force by a complex conjugate and taking the real part of the equation (2.22) yields

$$\langle F_e \rangle = \frac{1}{2} \varepsilon \left[\frac{-0.024}{1 + \left(\frac{\omega\varepsilon}{\sigma} \right)^2} \times (\nabla T \cdot E) E + 0.002 |E|^2 \nabla T \right]. \quad (2.24)$$

The resulting equation describes the average force produced by the Joule heating. It was previously shown [130] that this force is stronger in low frequency region (i.e. when Coulomb force dominates).

Chapter III: Fabrication and other related technologies

In this chapter the electrode fabrication using laser ablation and microfluidic channel fabrication using polymeric organosilicon compounds is discussed.

3.1 Electrode fabrication using laser ablation

Laser ablation is an attractive anisotropic technique, widely used in a number of industries and research fields such as microfabrication, medical surgery, mass spectrometry and film synthesis [131]. The working principle of laser ablation involves photothermal, photomechanical and/or photochemical processes, depending on the nature of the polymers used in the experiment and laser properties (i.e. wavelength and pulse duration).

Photothermal ablation takes place when the excitation energy is converted into heat. This process occurs when photons have low energy (long wavelengths) and laser radiation is delivered continuously or in long pulses. High power laser would melt, boil and eventually vaporise the material.

During the photomechanical process the photons in the laser beam (applied as short bursts) are absorbed by the surface, causing a rapid temperature rise. This is accompanied by sudden thermal expansion of the heated material and subsequent generation of stresses and strains within the material. At high power densities, the produced stress can exceed the elastic properties of the material and as a result the material is ejected from the surface.

Photochemical reaction takes place if the photons are sufficiently energetic, e.g. when high power nanosecond or shorter pulse of ultraviolet (UV) light is applied. The absorption of these photons results in breaking chemical bonds without heating. The volume of the product of this chemical reaction is larger than the original sample and this sudden volume increase expels the material.

The application of laser ablation technique for lab-on-a-chip devices and electrode formation has been discussed in detail elsewhere [132, 133].

In order to design electrodes using laser ablation, $1 \times 1 \text{ cm}^2$ with a thickness of 200 nm and $2 \times 2 \text{ cm}^2$ with a thickness of 50 nm gold coated glass was purchased from “Ssens”, The Netherlands and “Platypus Technologies”, USA. The sandwich structure is composed of glass, a chromium layer and a gold layer. The QuikLase-50ST laser mill, used for the electrode design ablates straight lines with a width, selected by the user in the range of 5 to 100 μm . The design of these lines is done in Qcad software and the .dxf files are uploaded to the laser mill system.



Figure 3.1. Dielectrophoretic trapping of 512 nm fluorescent particles on laser ablation fabricated gold electrodes. 5V peak-to-peak signal at 500 MHz was applied.

The centre of the gold cover slip is determined by locating the edges and taking the average in x and y direction. The alignment of the stage in x,y,z direction and monitoring of the ablation procedure is done via a built-in microscope. Short bursts (laser burst frequency was set to 10 Hz) were fired at the gold surface and an example of laser-ablation produced electrodes is shown in figure 3.1.

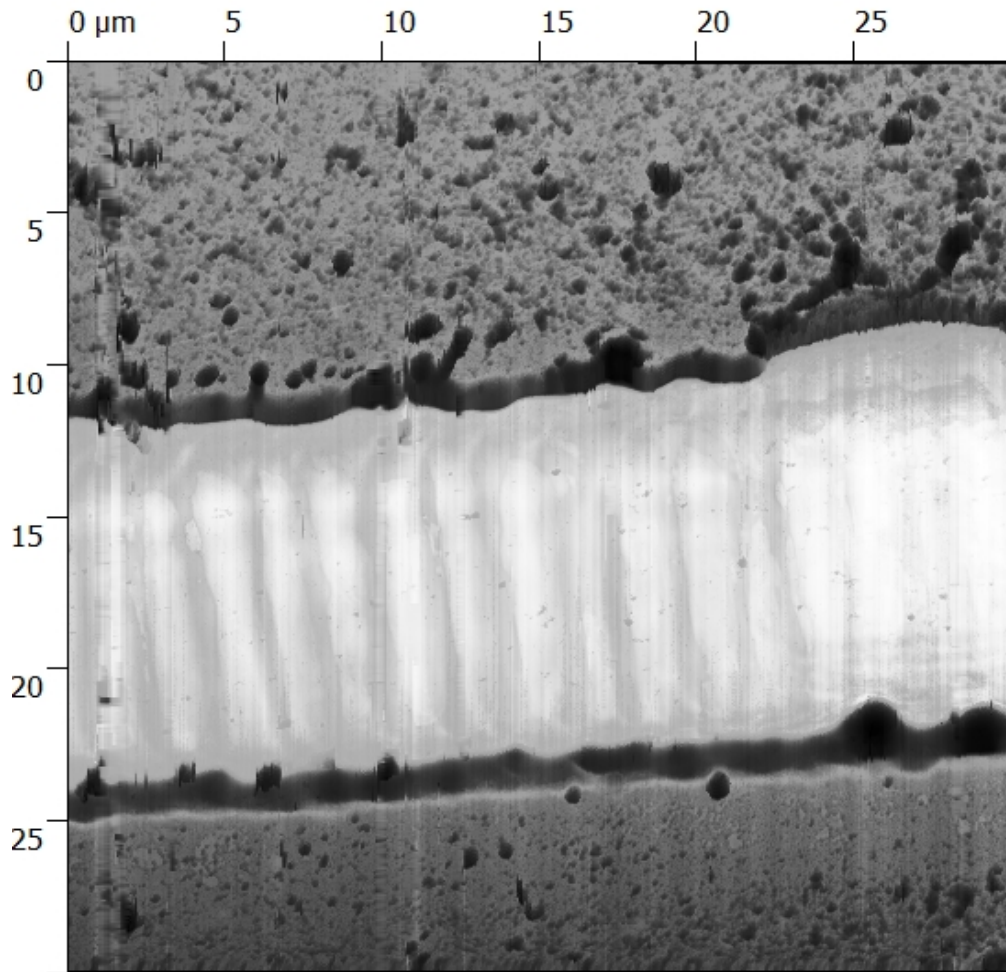


Figure 3.2. Atomic Force Microscope image of laser ablated channel on gold surface.

Both 50 nm and 200 nm thickness gold can be used to successfully observe DEP and AC Electrothermal flow. However, after either doing a number of experiments, or washing the existing solution off the electrodes, 50 nm gold would start to peel off. So it was decided to use 200 nm for further experiments. Note that it was necessary

to ablate the same line at least twice for a gold layer of 200 nm to get rid of any debris within the channel. The atomic force microscope (AFM) image of the ablated lines is shown in figure 3.2.

As the laser evaporates gold from the surface, melted pieces of hot metal land on the surface, leaving marks as shown in figure 3.3. This issue has successfully been addressed in our group by reversing the gold coated cover slip upside-down and ablating from the bottom; while the sample is placed inside a reservoir, such that the gold surface is in direct contact with water. Moreover produced lines are not perfectly parallel and at the interface of the ablated gap and gold, ‘hills’ are formed due to the melting of gold.

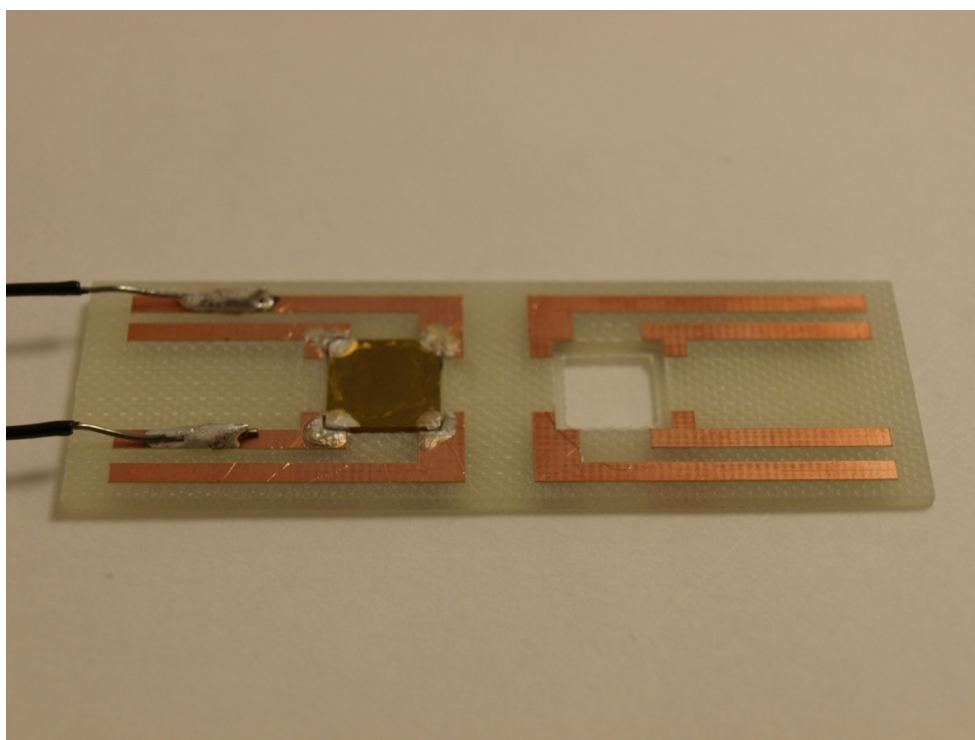


Figure 3.3. An image of an electrode holder with a gold coated glass. The connections on the plastic chip is made of copper which is connected gold via silver conductive paint.

Holders for the electrodes were also designed (see illustration in figure 3.3). 1cm² gap was machine-cut for a gold-coated glass to exactly fit into. Copper connection lines lead to the gold surface, and the connection between gold and copper is done

using the silver conductive paint (RS Components, UK). The wires for external connection are soldered on to the copper lines.

3.2 PDMS fabrication

The silicon masters, containing the structures used in this work were fabricated and provided by Philips Innovation Services, Eindhoven, Netherlands. The “Sylgard 184 Silicone Elastomer Kit” was purchased from Dow Corning, Glasgow, UK, which contains a PDMS prepolymer and a curing agent. The manufacturer recommended mixing ratio of the agent and polymer is 1:10. Increasing the ratio of curing agent makes the resulting PDMS harder. Thorough mixing of two agents introduces air bubbles, which are removed by placing the mixture in a vacuum desiccator for several minutes. Once the mixture is bubble free, it can be casted over a silicon master. The detailed description of the PDMS fabrication process is given below:

- 1) Heat the Silicone wafer (fixed to a glass petri dish, figure 3.4a) containing the desired geometries to 120 °C for 30 minutes to remove any water from the surface which can prevent adhesion. Switch off the hot plate and leave the system to settle for 10 minutes
- 2) Apply hexamethyldisiloxane (HMDS) into the closed petri dish with the master (figure 3.4b). HMDS will evaporate and (as the petri dish cools down) precipitate on all surfaces of the dish, including the master. This leaves the wafer slightly hydrophobic due to the methyl-terminated surface [134]. As a result HMDS prevents atmospheric moisture from condensing on the wafer improving the adhesion.

- 3) The de-gassed mixture (figure 3.4c) is then poured over the cooled silicon master (figure 3.4d). The petri dish is again placed into a vacuum desiccator in order to remove any bubbles introduced while pouring the PDMS. Due to the viscoelastic properties of the mixture, PDMS fills the entire structure.
- 4) The petri dish with PDMS and master is finally placed inside a 65 °C pre-heated oven and cured for 8 hours to ensure the full cross-linking of the monomer. Any monomer left in the PDMS can be toxic for the biological species under investigation [135]. After cooling, the structures are carefully peeled off the master.

In general the masters contain a number of non-connected structures, which can be individually used. A final step before performing experiments involves placing the pattern of interest on a microscope slide so that the channels are facing upwards. The microscope slide is placed into a UV/ozone atmosphere for 30 minutes (figure 3.4e). This is done to increase the strength of the bonds between the PDMS and the glass. Finally PDMS structures were placed on either glass or electrode surface (immediately after the exposure) forming a seal through the formation of covalent bonds at the interface (figure 3.4f).

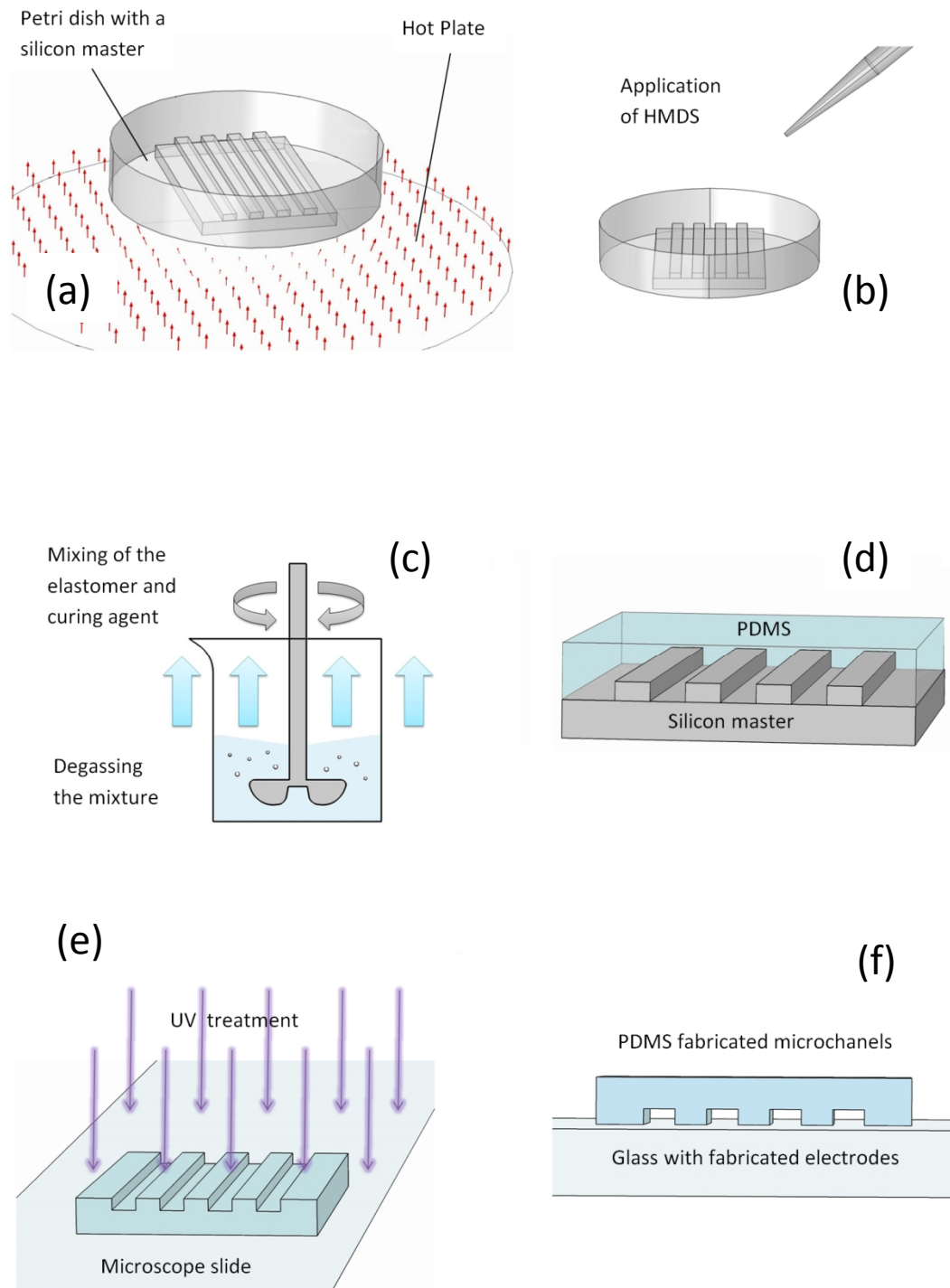


Figure 3.4. A schematic diagram of the PDMS fabrication procedure (see text). The arrows in (a) illustrate the heat, coming from the hot plate, in (c) the application of vacuum on mixed polymer and curing agent, and the exposure to UV light in (e).

Chapter IV: Amplitude Modulated Dielectrophoresis

The study on amplitude modulated (AM) DEP consists of video recording of the experimental procedure, image post-processing using the Matlab software and the mathematical description of work and data analysis.

Also presented are a number of concepts like cyclic steady state and signal modulation that were adapted from signal processing to describe object motion, driven by the dielectrophoretic force.

4.1 Introduction

A schematic diagram, showing the cyclic movement of spherical particles caused by AM DEP towards, and away from a horizontal planar electrode array, is displayed in figure 4.1(a). Each cycle consists of a particle collection phase followed by a release phase. The distribution of particles over space and time is described by the object concentration, $c(y, t)$ and the total number of objects, N , within the system remains constant throughout the experiment, i.e. no particles enter or escape. The corresponding time-dependent particle concentration near the electrode array at $y = a$ is shown in figure 4.1(b).

Before switching on the DEP force at the start of the collection phase of the cycle $t < t_l$, figure 4.1(a)(i), the particles are uniformly distributed with initial concentration, c_{li} (the subscripts ' l ' and ' i ' denote 'collection' phase of cycle and 'initial' state). When applying the potential to the electrodes, the action of the pDEP force causes downward particle movement, particularly near the electrode array where the DEP force is strong, figure 4.1(a)(ii).

As the concentration further increases near the array, DEP accumulation near the lower boundary results in a depletion layer that steadily rises towards the cap at $y = b$. The cap is located at height $h = b - a$ above the array, as shown. Eventually the DEP particle flux becomes balanced by thermally driven diffusion, figure 4.1(a)(iii), and approaches the steady state, $t = t_{ss}$ with concentration, c_{ss} . Switching off the ac potential initiates the release phase since there is no longer any pDEP force to trap the particles, and they diffuse into the bulk medium, figure 4.1(a)(iv) eventually reaching initial state at $t = t_{ri}$.

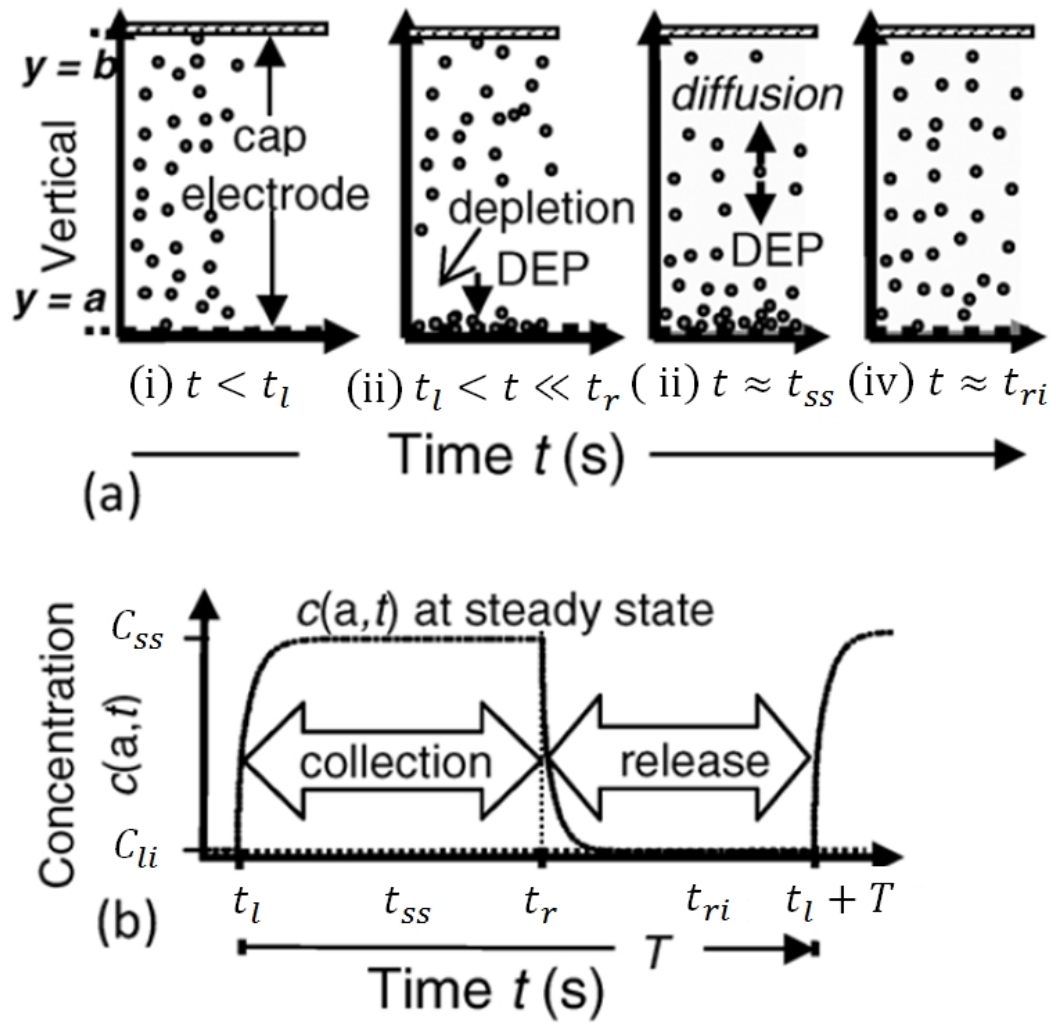


Figure 4.1. Particle cyclic collection under the action of pDEP force and release after the DEP force is switched off (a) cartoon showing particle distribution (side view) (b) concentration at the array as a function of time showing particle collection (onto the array) and release.

On–off switching can be repeated, as reported for pDEP of DNA [136]. In the scheme where on–off switch periods are sufficiently long for the system to reach steady and initial state in each of the phases, the difference between the steady state and initial concentration is $\Delta c = c_{ss} - c_{li}$. The alternative case when the on–off switch periods are much shorter than the time required to reach steady and initial states is considered in the following sections.

4.2 System model

A schematic of the AM RF DEP system is shown in figure 4.2. The signal generator supplying voltage to the DEP electrode system is assumed to be adjusted so that 100% modulation occurs. The electrical potential at the output is given by,

$$\Phi(t) = A_c[1 + m(t)] \times \cos(\omega_c t), \quad (4.1)$$

where the A_c and ω_c are the co-sinusoidal amplitude and angular frequency, respectively. To distinguish with modulation parameters, the subscript ‘c’ denotes carrier that is analogous to message signalling in electronic communication systems [137].

The modulation signal is a square-wave zero-mean cyclic process with period T , frequency $f_m = 1/T$ with subscript ‘m’ denoting modulation, and duty ratio, η , that distinguishes separate positive and negative phases. The modulating signal of the j^{th} cycle is written as

$$m(t) = sq(t) = \begin{cases} +1, & jT < t < jT + \eta T \\ -1, & jT + \eta T < t < (j+1)T \end{cases}, \quad (4.2)$$

The small time average spatial-temporal force distribution has been further developed using Laplace’s equation to evaluate spatial variation of electric field (peak value) and unit step function [138].

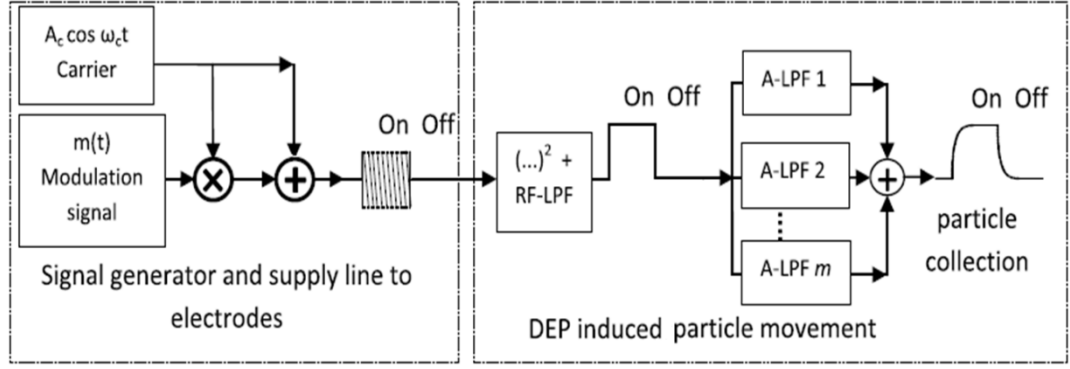


Figure 4.2. Schematic of ‘on–off’ amplitude modulation (AM) model. The left box shows an AM generator that produces a co-sinusoidal signal with a square-wave envelope. The AM signal is fed to the DEP planar array. The action of DEP process effectively removes the RF carrier, as shown in the right box, thus filtering the signal to a baseband square wave. The output shows diffusion-limited particle transport, quantified near the array, and is represented as a series of ultra-low pass filters (LPFs).

$$\langle F_{DEP}(x, t) \rangle = 2A_c^2 \pi r^3 \epsilon_m \text{Re}\{f_{CM}(\omega_c)\} \nabla |K(x)|^2 S_\omega(t), \quad (4.3)$$

where the bracket term for DEP force resemble time averaged force, $K(x)$ is the normalised electric field, given by $E(x)/\Phi(t)_{max}$ and $S_\omega(t)$ is a switch function that is unity (‘on’) at a specified time interval and zero (‘off’) elsewhere. After including the effect of thermally driven Brownian motion, the space-time evolution of concentration, assuming non-interacting particles, is written in differential form as the modified diffusion equation:

$$\frac{\partial c(x, t)}{\partial t} = -\frac{1}{\xi} \nabla \cdot (c(x, t) F_{DEP}(x) S_\omega(t)) + \frac{k_B T}{\xi} \nabla^2 c(x, t). \quad (4.4)$$

4.3 Concepts and Parameters

Particle motion to the electrode edges depends on the strength of the pDEP. After a certain time t_{ss} , the number of particles at the edges will be saturated. This number is dependent on the attracting force. When AM DEP is applied, however, the final number of particles, collected on the electrode edges n_{max} also depends on the collection-release state (transient or cyclic steady behaviour, figure 4.3) and the frequency of modulation signal. The electrode edges, previously referred to, in reality are small areas of interest around the electrodes. And the motion, away from that area caused by Brownian motion is not instantaneous. Hence the minimum number of particles n_{min} in AM DEP is also dependent on the collection-release state and the frequency of modulation signal as well as the stochastic force.

The cyclic DEP collection and release of particles within a designated volume leads to an important parameter: the difference between the maximum and minimum value of the particle number, for the j^{th} cycle. This particle number fluctuation, or amplitude, is defined,

$$n_j = n(t_j)_{max} - n(t_j)_{min}, \quad (4.5)$$

where subscripted terms ‘max’ and ‘min’ denote maximum and minimum particle number. As illustrated in figure 4.3, an important distinction is made between transition and periodic or cyclic steady behaviour c_{sb} . In the case of the transition state, the number of particles n at the beginning of j^{th} cycle is less than at the beginning of $j+1$, $n[jT] < n[(j+1)T]$. For c_{sb} this number remains constant. An alternative to ‘ c_{sb} ’ is a term ‘cyclostationary’, used in information theory, where

system statistics remain unchanged at periodic time points [139, 140]. This periodic equilibrium state implies that the initial condition (IC) and, as a result for constant pDEP force, the amplitude remains constant.

The transition from a well-defined DEP amplitude response at ultra-low f_m compared with the response being negligible at higher modulation frequencies naturally suggests a DEP ‘modulation bandwidth’. It can be defined as the range of modulation frequencies, f_m , such that at c_{sb} ,

$$n_s(f_{mB}) - \varepsilon \Delta n_s(f_{mUL}), \quad (4.6)$$

where ε is an arbitrary cut-off typically, $\varepsilon \approx 0.1$, and subscripts ‘ mB ’ and ‘ mUL ’ denote modulation bandwidth and ultra-low modulation that approaches dc (when $f_m \rightarrow 0$). The transition state may be of interest when analysing the initial collection rate as in [141], however, this work mainly focuses on the amplitude during the cyclic steady behaviour. This amplitude depends on the magnitude of DEP force, modulation frequency and duty cycle η . Clearly for extreme cases when $\eta = 0$ and $\eta = 1$, $n_s = 0$.

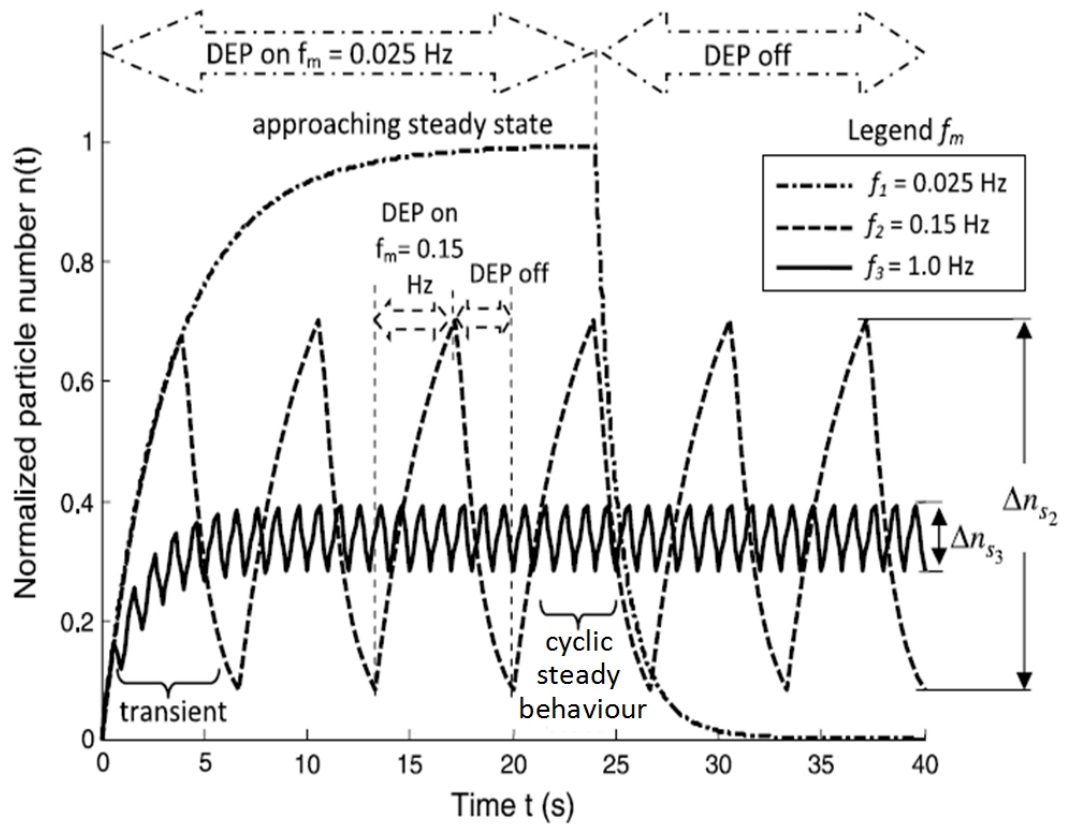


Figure 4.3 A schematic diagram of a normalised particle number versus time for $\eta=0.6$ (60% duty cycle)

So far the amplitude was presented as the difference in the particle number. And although image analysis tools like ImageJ offer flexible automated system for particle identification and estimation, using particle number for quantitative experimental analysis remains impractical. The fluorescence intensity produced by these particles is used and a normalised amplitude A_N is derived instead (section 4.4).

4.4 Normalised Amplitude A_N

As previously discussed in section 4.3, it is useful to describe the difference in ‘on’ and ‘off’ state in terms of the fluorescence intensity. The normalised amplitude A_N was derived for this purpose.

The amplitude “ A ” of the intensity variation for a number of cycles N_c over a video sequence can be defined as the difference between the maximum and minimum intensities over a certain j^{th} cycle:

$$A = \frac{1}{N_c} \sum_{j=1}^{N_c} [F_{\max}(j) - F_{\min}(j)], \quad (4.7)$$

F represents the spatially averaged fluorescence intensity. For a number of fluorescent particles, ignoring the background effect, it can be written as

$$F \propto \frac{f_k n I_{in}}{\Delta x \Delta z}, \quad (4.8)$$

I_{in} is the incident light, n is the number of particles, that at the cyclic steady state consists of a nearly constant minimum and maximum number; and f_k is the optical fluorescence constant that is dependent on the size and optical properties of the spheres. $\Delta x \Delta z$ mean that F is spatially averaged in x and z direction.

Equation 4.7 provides an estimate for the intensity amplitude A as shown in figure 4.4(b). But it is unsatisfactory to use this equation to compare between different experiments, because even though the nominal concentration remains the same, the number of particles close to the electrode array may vary. Also different particle sizes affect A due to the differences in f_k . Consequently, to compare different

experiments, a normalised value which takes into account an average intensity of the sequence of frames was derived by Bakewell *et al.* [138] and the resulting value of the normalised amplitude which considers the effect of duty cycle is give in equation 4.9.

$$A_N = \frac{\frac{\eta}{N_c} \sum_{j=1}^{N_c} F_{max}(j) - F_{min}(j)}{\frac{1}{N_f} \sum_{i=1}^{N_f} F(i)} \quad (4.9)$$

The resulting equation enables the comparison between experiments for particles with different diameters. In the equation N_f is the total number of frames. Provided that the variations in the aliquot concentration are not too large, the normalised amplitude is a good estimate of the cyclic temporal variation in particle numbers at cyclic steady behaviour.

4.5 Experimental materials and methods

The fluorescently labelled 0.5 and 1 μm diameter carboxylate modified polystyrene fluorescent spheres FluoSpheres® (F8813 and F8823, Invitrogen, UK) with yellow–green emission $\lambda = 515 \text{ nm}$ were diluted 2/1000, 4/1000 and 8/1000 stock. Reverse osmosis water (Millipore, UK) was used to dilute the latex spheres and the final conductivity was measured to be $\sim 1 \text{ mS/m}$ (Hanna, HI 8733, UK). 4 μl samples were micro-pipetted (Gilson, UK) on planar castellated microelectrode structure and covered with a coverslip. The electrode arrays were planar, platinum on glass, and made using standard microlithographic methods. The electrodes were mounted on Veroboard (RS components, UK). The height of the flow cell was approximately 160

μm . Imaging of the spheres for quantification used a standard epi-fluorescence upright microscope GX L3001 (Brunel Microscopes, Chippenham, UK) with $\times 500$ magnification ($\times 50$ objective) unless otherwise stated. An example of a particle collection onto the castellated planar electrodes is shown in figure 4.4(a).

Each AM DEP cyclic collection and release experiment was preceded by constant (non-modulated) DEP force, applied for two minutes to ensure sufficient spheres were concentrated near the array. An AM signal was generated using a Tektronix signal generator (FG504, Oregon, USA) configured such that the resulting signal is 100% amplitude modulated. Videos were recorded at 30 frames per second (fps) on Windows Media Video platform (WMV, Microsoft, USA) using a USB 2.0, 640×480 pixel resolution digital camera (Brunel Microscopes, UK) controlled with Scopephoto v3.0 software (Scopetek, Hangzhou, China).

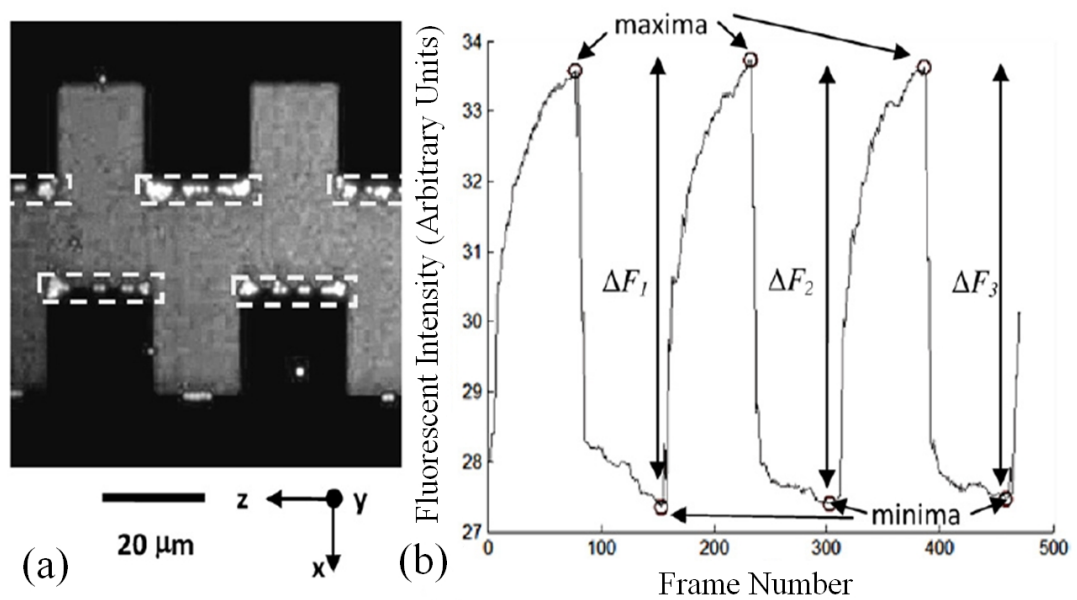


Figure 4.4 Fluorescence spectroscopy (a) sub-frame sized image of fluorescent $1.0 \mu\text{m}$ spheres collecting onto the edges of $20 \mu\text{m}$ feature size castellated electrodes with particle capture region of 4 pixel width lying well within dashed rectangles shown (the vertical y axis faces out of the page), (b) example of cyclic steady behaviour of the fluorescence intensity at $f_c = 500 \text{ kHz}$, $f_m = 0.2 \text{ Hz}$, $A_c = 6 \text{ V}$, at 30 frames/cycle; the fluorescent intensity was normalised with respect to area around the electrodes (sum of all pixel intensities divided by the total number of pixels).

A total of three videos per experiment were recorded. Consistency between analysed data was obtained using two procedures. First, the first video of the new experiment was recorded using the same signal properties as the last video of the previous experiment. Second, the fluorescence variation was normalised using the equation 4.9. In order to analyse the intensity variation of particles, the recorded videos were converted into an .avi file format using Prism Video File Converter v1.61 (NCH Software, USA), and processed using Matlab 7.0. The procedure can be described in the following steps:

- (i) A Matlab created program opens a video at a suitable frame e.g. when particles are collected onto electrode edges. This enables the identification and selection of the exact location of the collection regions. An example is shown in figure 4.4(a), where the analysed 'region' of 4 pixels lies within the area of the dashed rectangles. The same 'region' is used for a user defined and hand-picked number of electrode edges.
- (ii) For every frame of the video each subplot is spatially averaged in x and z direction (figure 4.4(a)) using the trapezium rule to obtain and save the fluorescence value in a text file.
- (iii) The program moves to the next frame and repeats the procedure.
- (iv) A profile of the fluorescence intensity variation as a function of the analysed frame number is produced and displayed for further amplitude analysis.
- (v) The amplitude is given by the difference between the maximum intensity value during the collection phase and minimum value during the release phase of cyclic steady behaviour. Noisy fluorescence intensity signal

appears to have a lot of localised minima and maxima, as shown in figure 4.4(b), which has to be filtered by selecting a threshold for amplitude value and periodicity according to modulation signal

4.6 Number of particles and fluorescent intensity relationship

The fluorescence intensity for both 0.5 μm and 1 μm particles showed a linear relationship as shown in figure 4.5. The number of particles was estimated by eye from the recorded videos.

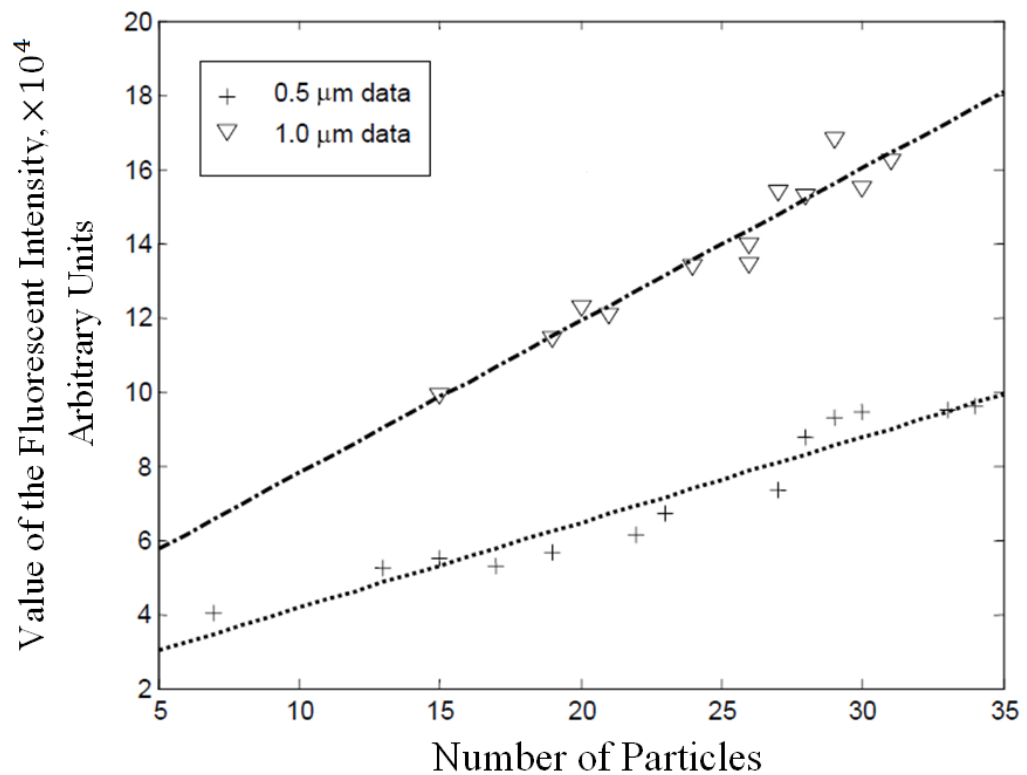


Figure 4.5. Plot of the total measured fluorescence intensity versus a number of 0.5 μm and 1 μm particles within the area of interest

The intention was to make a direct comparison between the number of particles and resulting fluorescence intensity. The total fluorescent intensity around a number of electrodes, rather than spatially averaged value was used. Sufficient area, around the electrodes was selected to ensure that the entire particle is contained within when measuring the intensity.

The experiment was done using 3 V peak-to-peak applied 500 kHz signal. Particles were monitored on a frame-by-frame basis and measurements were only performed when particles collected at the edges of the electrode (rather than approaching as this may alter the intensity reading due to the particle being in a plane that is out of focus). The relationship remains linear for a relatively small number of particles collected on the edges. As more particles are being attracted by pDEP force, fluorescent spheres start ‘clumping’ and individual particles become indistinguishable. Changes in the number of particles at this point no longer results in proportional change in the amount of detected light. These findings are consistent with previously reported data [141].

The difference in the amount of fluorescence intensity of 0.5 μm and 1 μm particles, shown in figure 4.5 is explained by the fact that different diameter sizes also exhibited different spot sizes (number of occupied pixels). This difference for low concentration of particles (individual particle at the electrodes can be identified) is shown to be approximately of factor of 2, so in order to perform the comparison, the dilution of 2/1000 and 4/1000 for 1 μm and 0.5 μm particles respectively was used for all further investigations.

4.7 Effect of varying the switching frequency

In the following section a 500 kHz, 10 V peak-to-peak sinusoidal signal was 100% modulated by a square wave of various frequencies f_m as illustrated in table 4.1:

The setup described has Dielectrophoretic force dominating over other AC electrokinetic forces like AC electroosmosis and AC electrothermal flow [35].

Table 4.1. Modulation frequencies used for AM-DEP experiments.

Experiment number	Modulation frequency, Hz
1	0.025
2	0.05
3	0.15
4	0.25
5	0.5
6	1
7	2
8	3
9	4
10	10
11	25

A surface plot of the fluorescence as a function of the modulation frequency and time $F(f_m, t)$ up to 40 s is shown in figure 4.6 for 0.5 μm diameter spheres. The modulation frequency is deliberately represented in stepped format in order to clearly illustrate the dependence of the fluorescence on the ‘on/off’ modulation. In figure 4.6 the fluorescence amplitude $F(f_m, t)$, being the difference between the maxima and minima, at $f_m = f_1 = 0.025$ Hz is greater than at $f_2 = 0.05$ Hz. This trend continues for all frequencies listed in table 4.1. The plots illustrate a clear

reduction in DEP induced amplitude as the modulation frequency is increased until it is practically indistinguishable from non-modulated DEP force.

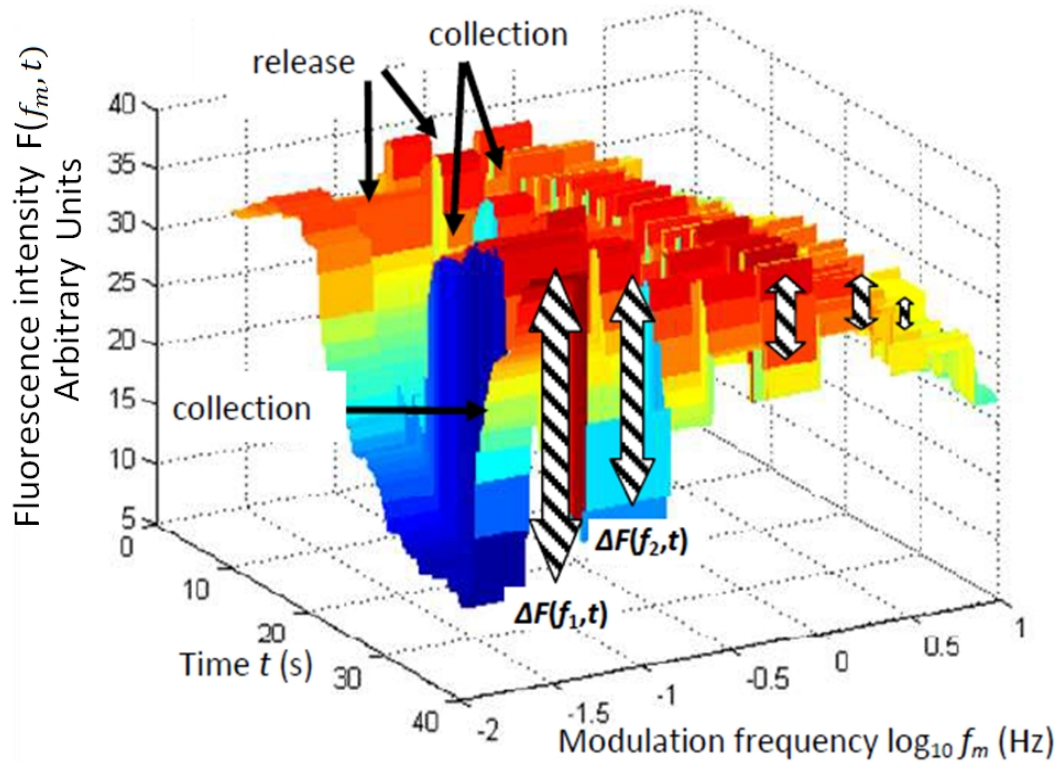


Figure 4.6. AM DEP fluorescence for 0.5 μ m diameter spheres as a function of time t and modulation frequency f_m . Fluorescence amplitude (differences between maxima and minima), indicated by hashed double arrows, decreases as f_m is incremented.

Normalised amplitude A_N for both 0.5 μ m and 1 μ m particles has been derived according to equation 4.9 and results are shown in figure 4.7.

The normalised amplitude near the 10% cut-off for the 0.5 μ m diameter spheres is shown to be slightly larger than for the 1.0 μ m diameter spheres. This result is consistent with smaller spheres exhibiting a faster diffusion time. Typically, whenever the normalised amplitude is less than 10% of the maximum at the lowest modulation frequency $f_m = 0.025$ Hz, very little microscopic movement of particles, in and out of the capture region, was observed.

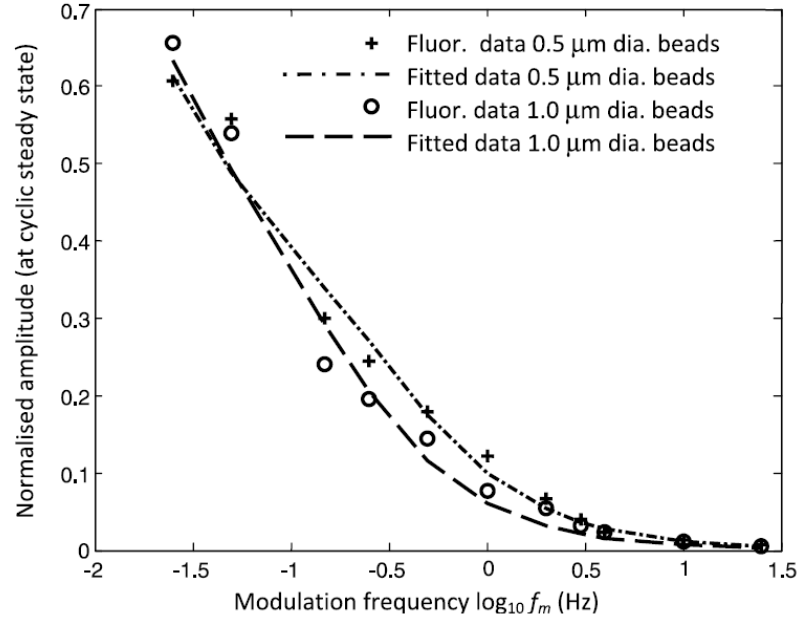


Figure 4.7. Normalised amplitude at cyclic steady behaviour versus DEP ‘on/off’ modulation frequency, f_m , comparing measured fluorescence data for 0.5 and 1.0 μm diameter particles. The smaller particles exhibit a slightly greater bandwidth of the order of 1 Hz. The fit was done using the exponential fit in curve fitting tool in Matlab software.

One of the factors affecting the bandwidth is the scaling and dimensions of the fluorescence microscope system. An increase in physical dimension of the analysed area was achieved by using a smaller, $\times 20$ objective. This has resulted in an increase of physical dimensions of a pixel size and hence a slight decrease of the bandwidth. For a $\times 50$ objective the size of a pixel is 0.16 μm . Using the Stokes-Einstein's relation, the average distance travelled by diffusion for a particle can be calculated:

$$\langle x \rangle = \sqrt{\frac{k_B T \times t_{dif}}{3\pi\mu r}}, \quad (4.10)$$

where k_B is the Boltzmann constant, T is temperature, t_{dif} is the time travelled, μ is dynamic viscosity and r is the radius. For 1 μm particle the motion bandwidths was at around 1 Hz resulting in an average distance travelled by diffusion $\langle x \rangle \approx 0.6 \mu\text{m}$, which is in a good agreement with 4 pixels used for the analysis.

4.8 Effect of varying the duty cycle

The effect of varying the duty-cycle ratio on c_{ss} amplitude was investigated using 0.5 μm diameter spheres for three different modulation frequencies: $f_m = 0.25, 0.5$ and 1 Hz. All three plots of the normalised amplitude as a function of the duty-cycle ratio shown in figure 4.8 exhibit the convex shape.

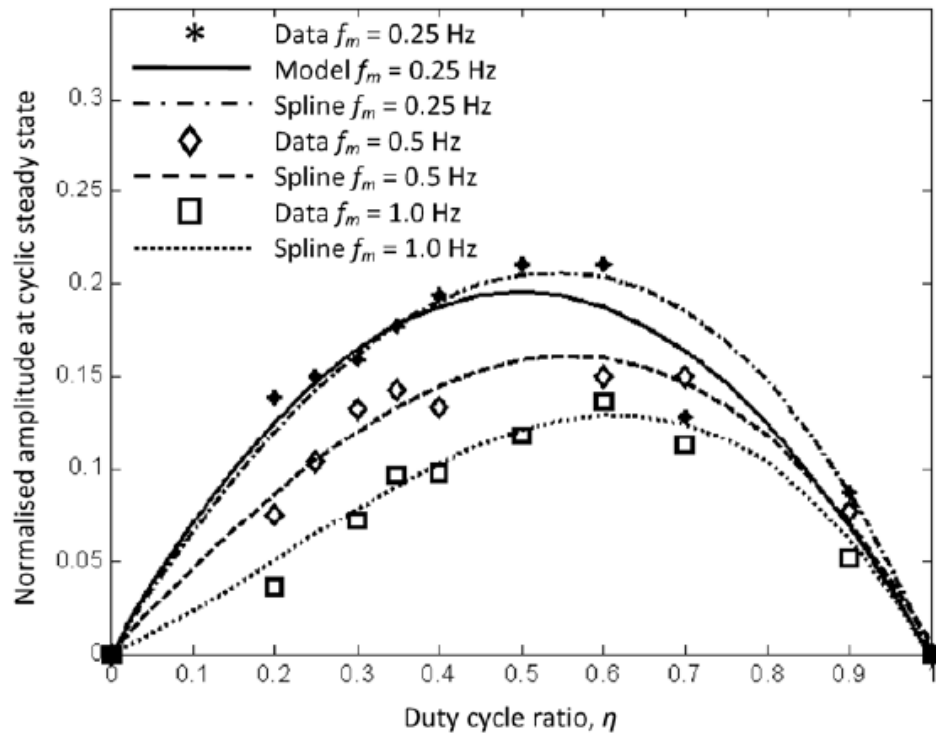


Figure 4.8. Normalised amplitude at cyclic steady behaviour versus duty-cycle ratio, η for three DEP ‘on/off’ modulation frequencies, f_m , 0.25, 0.5 and 1.0 Hz. The solid line labelled as ‘Model’ shows a data comparison with an exponential series model. The ‘Model’ plot is obtained by solving the equation 4.4 for amplitude modulated system as shown in [138].

As can be seen from graph, the maximum amplitude for different duty cycles vary. Clearly as the modulating frequency increases, the maximum amplitude value progresses towards the higher duty cycle ratio.

4.9 Conclusion

In this chapter the concept of amplitude modulated dielectrophoretic force is explained first. This force is further used to develop an inexpensive, easy to setup system for particle manipulation. This system, however, is restricted to limited concentrations of particles that can be used. The detection system also has a number of limitations:

- Spot size of the particles,
- Camera pixel size,
- Video recording rate (fps),
- Microscope objective magnification.

In principle, similar experiments can be performed at smaller scales (e.g. a higher magnification lens with a faster video recording camera), which would result in a higher bandwidth. Rather than switching the electric field ‘on’ and ‘off’ in a controlled fashion, hopping between frequencies could be performed instead. For a frequency jump between 500 kHz and 50 kHz using the experimental setup as described in 4.4, particles started moving from the electrode edges (attracted by dominating DEP force) to an area inside the electrodes (at this point AC electroosmotic fluid flow would dominate) and back, according to the carrier signal frequency.

It has been previously noted that the particle collection rate is proportional to the dielectrophoretic force and thus depends on the properties of the particle and medium. This chapter presents a novel tool for a more controlled collection rate

estimation thus enables accurate parameter estimation which is essential to understanding the frequency response of the force. Latter enables developing the necessary experimental conditions for particle separation, concentration or detection.

As an advancement to the developed framework in this chapter, it has been recently shown that the developed tool can be also used for hopping between a number of frequencies and measuring the collection rate to determine the dielectric properties of particles [142].

Chapter V: The Behaviour of the Bacteria in Channels with External Forces

The experimental conditions that mimic the geometrically constrained natural habitat of the bacteria are developed using the PDMS microchannels. The effects of the various electrokinetic techniques under these conditions are investigated in the media that supports the growth of bacterial species.

5.1 Introduction

In this chapter, a systematic study of the manipulation of bacteria using various electrokinetic methods will be presented. Unlike the fluorescent nanospheres used for the experiments in the previous chapter, bacteria are living organisms with a complex structure, reproduction cycle, internal motility mechanisms and sensors. All these factors contribute to how the bacteria behave and are important for successful manipulation of these organisms. Moreover, the natural habitat of bacteria is geometrically diverse and spatially restricted, which has been mimicked by the use of microfabricated structures during the experiments.

This chapter has the following structure: a general introduction to bacteria is given first. This is followed by the materials and methods section that contains the design of the channels, bacteria growth conditions and the experimental setup that was used for further analysis.

The description of the numerical simulation is presented in 5.3. *Pseudomonas Fluorescens* bacteria were used to experimentally investigate the effect of various electrokinetic techniques. The results for both experimental investigation and simulation of various electrokinetic techniques is shown in section 5.4

The concluding remarks are presented in section 5.5.

5.2 The bacterial structure and growth

Bacteria are one of the oldest living organisms which have been evolving for around 4 billion years and are present in most habitats of the planet [143]. It is a single autonomous prokaryotic (lacks cell nucleus) cell with various shapes, ranging from spherical structure (cocci) to spirals and rods (bacilli). Typical dimensions are a few micrometres in length and a general structure is presented in figure 3.1

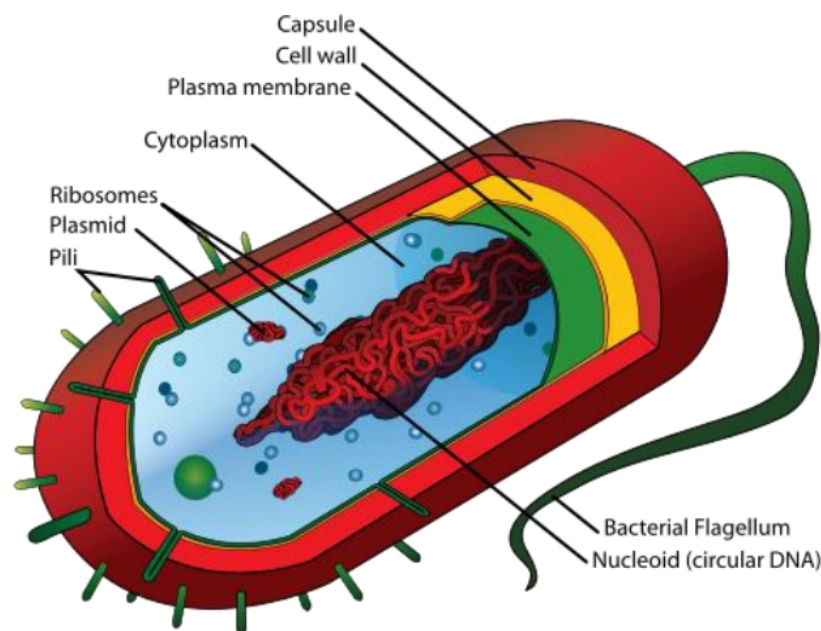


Figure 5.1 Structure of a bacterial cell (figure drawn by Mariana Ruiz Villarreal and reprinted with author's permission)

The bacterial cell has three different regions: cell envelope, appendages and cytoplasmic region. The envelope consists of a cell wall, capsule and a membrane. Depending on the composition of a cell wall, bacteria are divided into gram-positive and gram-negative bacteria according to their reaction to violet-iodine dye complex [144]. Standard microbiology text books like [145, 146] provide more details on the structure and function of each section of bacteria cell.

Growth in microbiology is defined as the increase in the number of cells. Each cell has a limited lifespan, and a species is maintained only as a result of continued growth of its population. Bacterial cell growth relies on a number of reactions necessary for doubling the amount of all cellular components and division to form two daughter cells (most microorganisms grow by binary fission). In order to accommodate these reactions, a bacterium needs nutrients, a source of energy, appropriate temperature and pH level, water, presence or absence of oxygen and inorganic ions. Provided the necessary conditions are met, the growth of colony in an enclosed vessel goes through a following cycle:

- When a population is introduced into a fresh medium, growth does not start instantaneously, but rather after a certain period of time. This time is called a **Lag Phase** which occurs when either a damaged (but not killed) population is introduced to the same media or when a microbial population is transferred from a rich culture medium to a poorer one.
- **Exponential Phase** exhibits the division of a cell into two daughter cells, each of which also divide and so on. The rate of the exponential growth depends on environmental conditions as well as genetic characteristics of the organism. During this phase cells are typically in their healthiest state.
- The increase in cell numbers only happens for a limited amount of time due to depletion of essential nutrients and waste products that organisms accumulate in the medium. The phase, when there is not net increase or decrease in cell number is referred to as **Stationary Phase**. A sample, taken from a colony at a stationary phase and placed into a new medium of similar environment would also exhibit a lag phase before exponentially growing.

- After the population reaches the stationary phase, the cells may remain alive and continue to metabolize but they will eventually start dying mainly due to the lack of the nutrients, entering the **Death Phase**.

One of the responses to environmental changes, like nutrient depletion, that bacteria have developed, involves the formation of a resistive cell morphology called spore (which are generally less active than a vegetative cell). More commonly however, the bacteria move away from the hazardous regions towards the areas that are more suitable for reproduction. These areas could for example be richer in nutrients or warmer. A biological term for this active spontaneous motion is motility. It is generally used for unicellular and simple multicellular organisms.

5.3 Bacteria in channels

5.3.1 Overview

As already mentioned, the behaviour of bacteria is extremely dependent upon the environment it lives in. However, most of the studies are performed on colonies that were cultivated on the surface of agar. This environment may be convenient, however, it has little resemblance of the diverse microgeometries that the natural habitat of the bacteria displays. On the other hand most environments in which bacteria live are non-transparent making it impossible to observe how they adapt and optimize their behaviour within the physical constraints. Using well established semiconductor fabrication techniques combined with transparent, non-toxic and oxygen permeable poly(dimethylsiloxane) – PDMS material [147], artificial

structures that resemble natural spatial environments can be produced and bacteria monitored in real time.

A number of experiments on the bacteria within the spatially restricted environment have been performed. One of the experiments that analysed the behaviour of the *E.coli* has shown that in a microfluidic channel these bacteria species preferentially swim along the right hand side of the channel [148]. Other experiments have shown that the bacterial motility is guided by surface topography suggesting that bacteria senses the obstacles within the channel [149]. In another study the velocity of the motile bacteria has been investigated in the channels of different geometries and widths [150]. It was concluded that the surface topography affects the speed and the channel width only slightly larger than bacteria is sufficient for them to swim through. Recently, Kojima *et al.* [151] has fabricated a PDMS microchip to analyse the chemotaxis (the phenomenon whereby the cells direct their motion according to certain chemicals in the environment) of bacterial cells.

It has been suggested that the motility of bacteria over specially designed structures can be used for bio-computation devices [152, 153]. The proposed example of such a device is a microfabricated maze with a single entry and exit. The authors suggest that the mathematical problems can be coded using fabrication techniques and these problems can then be solved using biological agents such as bacteria.

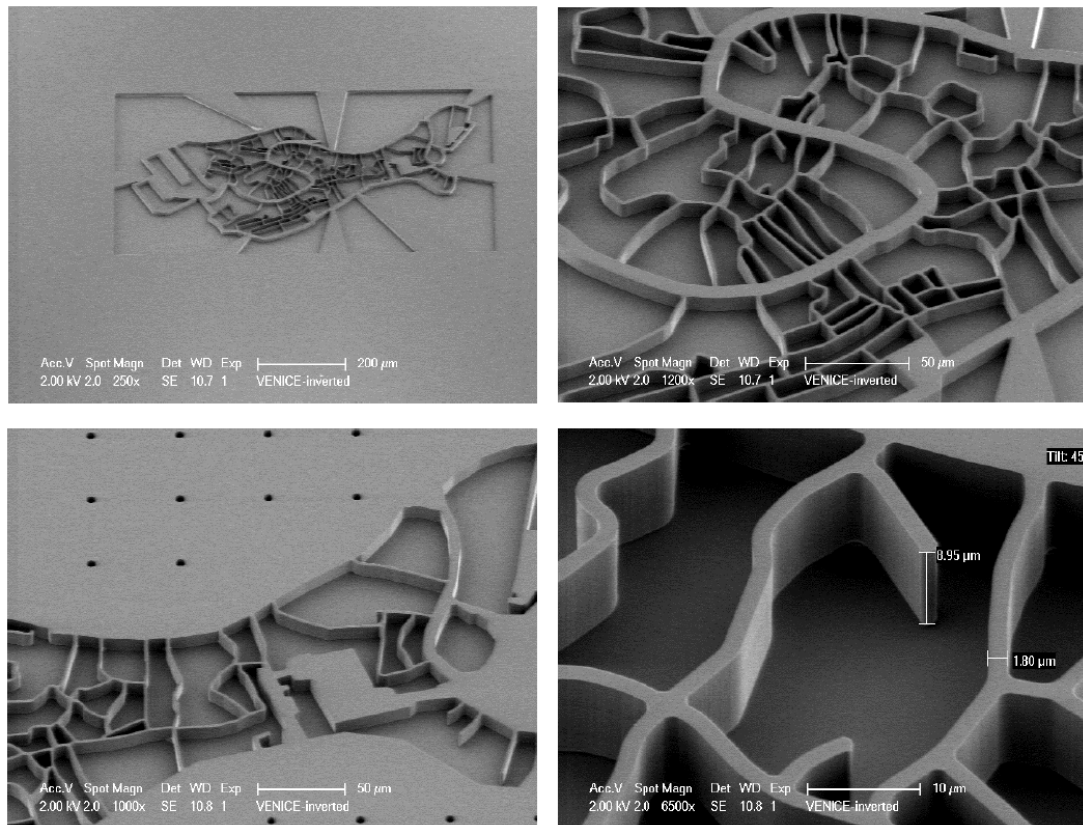


Figure 5.2. Scanning electron microscope image of the fabricated Venice waterways. The image was produced by the Philips, Eindhoven, The Netherlands

Another possible application of bacteria motility in complex structures, currently seen as a long term innovation can be found in biosimulation devices. These devices are believed to help solve problems such as traffic in large urban areas or optimising the flow of people in confined spaces. Venice waterways were chosen as the subject for such a device which was fabricated from the PDMS, using the negative tone silicon master (figure 5.2), produced by Philips Research, Eindhoven, The Netherlands.

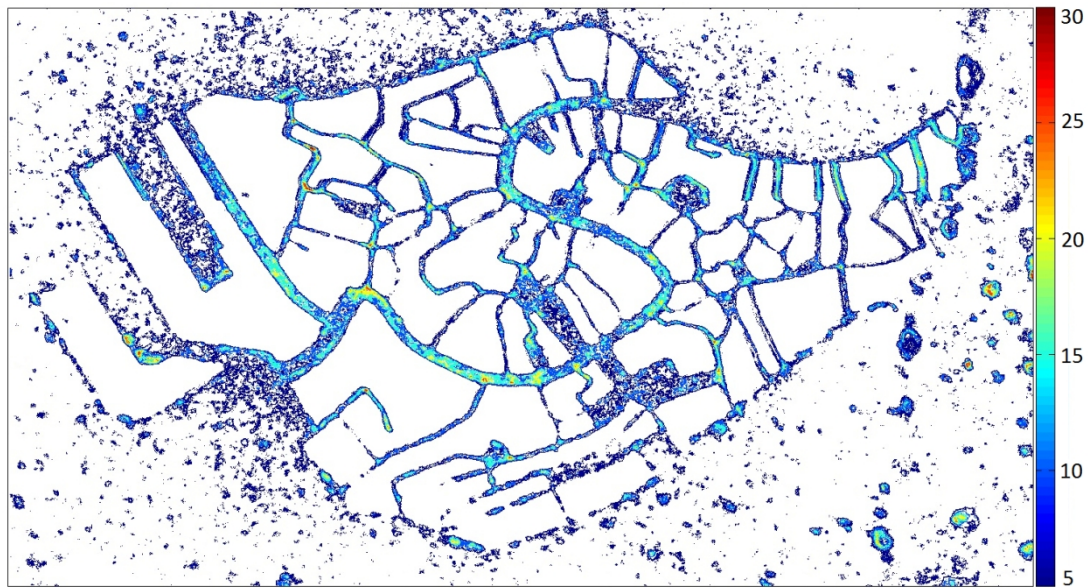


Figure 5.3. Congestion heat map of the Venetian waterways. Areas coloured towards the red end of the spectrum indicate the pixels were visited more frequently by bacteria

As shown in figure 5.3, the bacteria were able to enter every channel in the Venice waterways. In order to explore the potential of this device to solve traffic problems, it has to be integrated with a system that can prevent the motion of bacteria in channel junctions [154].

5.3.2 Bacterial Growth Conditions

The nutrient agar medium which consists of 1% of Luria Bertani (LB) broth and 1.5% of agar mixed with distilled water was sterilised by autoclaving for 15 minutes at a temperature of 150 °C. Once the solution had cooled down it was poured into a petri dish and left to dry. Dry nutrient agar can now be used to host the bacteria. A loopful of a single colony of bacteria is further taken from the agar and placed inside 5 ml of LB broth. The broth is prepared by mixing 0.5% yeast extract, 1% tryptone

and 1% NaCl with deionised water. The pH was adjusted to 7.2 by adding NaOH. The colony was left overnight at 30 °C shaking at 200 rpm. Finally 100 µl of the overnight culture was mixed with 10 ml of LB and left to grow for the optical density (OD) to reach ~0.6. At this optical density value the bacteria is approximately in the middle region of its exponential growth phase as discussed in 5.2 [155, 156]. Another term for optical density is absorbance and its quantitative measure can be expressed as a logarithmic ratio:

$$A = -\log_{10} \left(\frac{I_1}{I_0} \right), \quad (5.1)$$

where I_1 and I_0 are the light intensities after passing (transmitted) and before passing (incident) through the material. Experimentally the absorbance was measured by placing a cuvette filled with the solution containing necessary specimen (e.g. bacteria) into a spectrophotometer.

5.2.3 Experimental procedure

The preparations for the experiment were made in the following manner:

1. PDMS maze was fabricated as discussed in 3.2,
2. A small section containing only one channel was cut out of the maze,
3. This section was placed on a microscope slide and put in UV/ozone with the channel facing upwards to establish the stronger binding of PDMS to the electrodes,
4. After 30 minutes the treated PDMS was placed on the electrodes surface with the channel facing towards the electrodes,

5. A Bovine Serum Albumin (BSA) solution was pipetted onto the electrodes, fully submerging the PDMS block. BSA is a surface-active agent that prevents cell adhesion to the glass,
6. The system was placed in vacuum for 10 minutes to extract any air trapped in the channel. This also allows the BSA to fully coat the PDMS channel,
7. After the vacuum treatment, excess solution was removed and the area around the PDMS and inside the channel was dried with filter paper.
8. Steps 5 and 6 were repeated with LB solution instead of BSA. Excess broth was again removed from around the PDMS leaving the inside of the channel filled,
9. The solution, containing the bacteria was pipetted on one of the sides of the channel,
10. The introduction of the bacteria into the channel was either natural (motile bacteria would swim into the channel) or induced: dragging the liquid with filter paper or liquid drying at the opposite side of the channel would also drag the bacteria.

The schematic diagram of the experimental setup is shown in figure 5.4. The channels selected for the study were $\sim 140\ \mu\text{m}$ wide and $\sim 3\ \text{mm}$ long. For a channel this wide, the effect of the BSA on the surface roughness and the electroosmotic velocity [157] can be ignored.

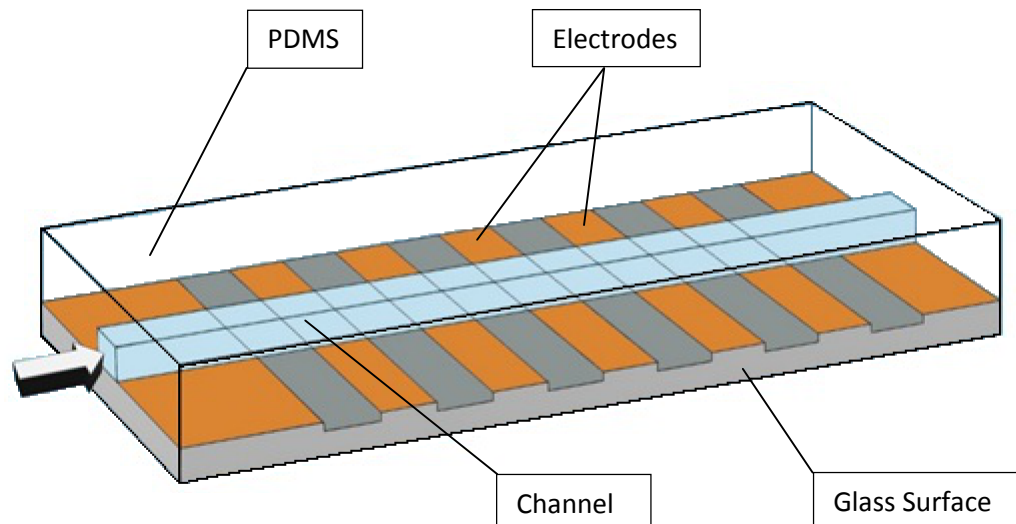


Figure 5.4. A schematic diagram of experimental setup to investigate the DEP, ACEO and ACET effect on bacteria inside the channel

The behaviour of bacteria inside the channel was observed using an upright fluorescent microscope with x20 objective lens. The cells of the bacteria used for the experiments in this chapter contained a plasmid encoding green fluorescent protein (gfp) which allowed for easy detection via fluorescence microscopy.

5.4 Details of the numerical simulation

Comsol Multiphysics (version 4.3) software was used to perform numerical simulation of the ACET flow in channels. Conceptually the modelling consists of three parts each with its own set of equations described in the following section: the electric field distribution, the temperature rise and the resulting force that causes the fluid flow. These equations are already built into the physical models of the software modules. Namely the physical models used for the computation were: Electric Current (AC/DC Module), Heat Transfer in Fluids (Heat Transfer Module) and

Creeping Flow (Fluid Flow Module). The flow chart of the simulation procedure is shown in figure 5.5.

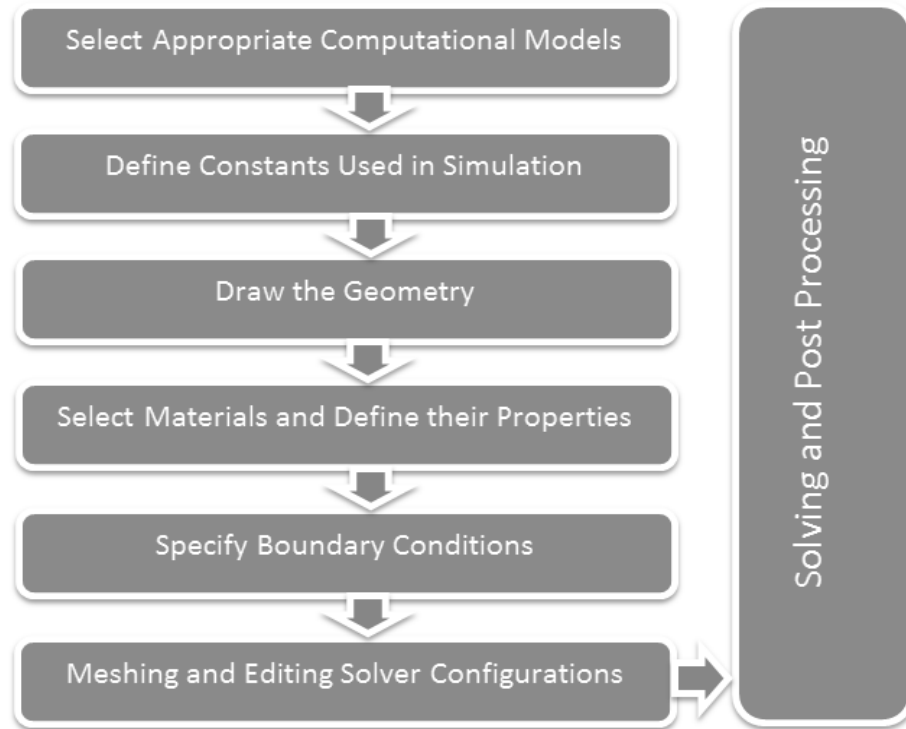


Figure 5.5. Flow chart diagram describing the step by step procedure for the numerical simulation of ACET flow. The simulation was achieved using Comsol Multiphysics v.4.3

Both two and three dimensional geometries that represent the polynomial and finger electrode setups were used for the investigation. The common feature of all the geometries was the sandwich structure of glass, electrode, fluid and PDMS layers. Joule heating, produced by the electric field is used as a source of heat which diffuses in the solution, glass and PDMS. Due to the high thermal conductivity and the thin layer (200 nm) the effect of gold on the temperature change can be ignored. The outermost layer of the PDMS and the glass were subjected to convective cooling with the heat transfer coefficient of 5 W/mK (heat transfer coefficient value for air). This means that the heat produced by the electrodes was balanced by the air in the

room. ACET induces a volume force to the fluid bulk and obeys a no-slip boundary condition [120]. In order to simulate the fluid flow, a volume force described in equation 2.24 had to be broken down to x and y components and added to the creeping flow.

For a 100 kHz, 5 V applied signal the simulated fluid flow was in $\mu\text{m/s}$ region (figure) which is in a good agreement with previously reported data [130].

Table 5.1. List of parameters used for the numerical simulation of AC Electrothermal Flow.

Parameter	Value
Permittivity of Air ε_0	$8.85 \times 10^{-12} \text{ F/m}$
Relative Permittivity of fluid	$80\varepsilon_0$
Frequency of the Signal	$2\pi \times 5 \text{ MHz}$
Electrical Conductivity of fluid	16.4 mS/m
Thermal Conductivity of PDMS	0.15 W/(mK)
Thermal Conductivity of Glass	0.96 W/(mK)
Heat Transfer Coefficient	5 W/(mK)

5.4.1 Equations used in the simulation

The set of equations along with the boundary conditions that allow us determine the electromagnetic field distribution in the system are referred to as the Maxwell's equations. In differential form these equations are:

$$\nabla \times \bar{H} = \bar{J} + \frac{\partial \bar{D}}{\partial t}, \quad (5.2)$$

$$\nabla \times \bar{E} = -\frac{\partial \bar{B}}{\partial t}, \quad (5.3)$$

$$\nabla \cdot \bar{D} = \rho, \quad (5.4)$$

$$\nabla \cdot \bar{B} = 0, \quad (5.5)$$

where \bar{J} is the current density, \bar{E} and \bar{H} are the respectively the electric and magnetic field intensities, \bar{D} and \bar{B} are the electric and magnetic flux densities and ρ is the charge density. The software solves the system of equations using the quasi-static approximation which is later shown to be valid for the system used. This simplifications has the effect such that $\frac{\partial \bar{D}}{\partial t} = 0$ and $\frac{\partial \bar{B}}{\partial t} = 0$. And so the electric field can be expressed in terms of electric potential $\bar{E} = -\nabla V$. Combining this electric field expression with $\bar{D} = \epsilon_r \epsilon_0 \bar{E}$ gives:

$$-\nabla \cdot (\epsilon_r \epsilon_0 \nabla V) = \rho, \quad (5.6)$$

The continuity equation used for simulation is expressed by:

$$\nabla \cdot \bar{J} = \nabla \cdot (\sigma \bar{E} + J^e), \quad (5.7)$$

where σ is the conductivity and J^e is the external current density.

Quasi static approximation neglects the fact that the changes in electromagnetic fields do not vary in phase with the source. Hence it enables calculating the electromagnetic fields by considering stationary currents at every instant. For this approximation to be valid, the currents and electromagnetic fields must vary slowly.

To accommodate that, the structure must be small compared to a wavelength. For a

frequency of 20 MHz, the highest frequency used in any experiment, the wavelength $\lambda = \frac{c}{\nu} = \frac{3 \times 10^8}{2 \times 10^7} = 15 \text{ m}$, which is much greater than the typical dimensions of a microfluidic system. Another assumption in quasi static approximation enables

ignoring the coupling between the magnetic and electric fields. This is the case when the skin depth is much greater than the geometry used. The skin depth is given by

$$\delta = \frac{1}{\sqrt{\pi\mu_0}} \sqrt{\frac{\rho}{\mu_r \nu}}, \quad (5.8)$$

where μ_0 and μ_r are the permeability of free space and relative permeability respectively, ρ is the resistivity and ν is the frequency of an applied signal. At 20 MHz the values were determined:

Table 5.2 The skin depth and the simulation used geometry dimension comparrison.

Material	Skin Depth	Dimensions used
Gold	6.7 μm	0.2 μm
Glass	$10^8 - 10^{12}$ m	1 mm
Fluid	0.1 m	10-20 μm
PDMS	4.3×10^5 m	< 1 mm

This proves that the quasi static approximation is valid for the simulation.

The current, flowing through the fluid generates the heat (known as the Joule heating). In order to estimate the effect this heating has on the system the energy balance equation that links the electric and thermal fields is used:

$$\rho_m c_p \bar{v} \cdot \nabla T + \rho_m c_p \frac{\partial T}{\partial t} = k \nabla^2 T + \sigma E^2, \quad (5.9)$$

where ρ_m is the mass density, c_p is the heat capacity, \bar{v} is the fluid velocity and k is thermal conductivity. The term $\rho_m c_p \bar{v} \cdot \nabla T$ of equation 5.9 illustrates the heat

convection by fluid motion which is assumed to be minimal. For this assumption to be valid, the relationship has to apply:

$$\frac{\rho_m c_p l v}{k} \ll 1. \quad (5.10)$$

For a water of a density of 1000 kg/m^3 , heat capacity of $4.2 \times 10^3 \text{ J/kgK}$ and $k = 0.6 \text{ W/mK}$ with characteristic length $l = 20 \text{ }\mu\text{m}$ the assumption is valid for fluid flows slower than 7 mm/s . The observed and simulated flows were in $\mu\text{m/s}$ range thus the assumption applies.

The other term on the left hand side of equation 5.9 stands for the temperature diffusion process. The diffusion time estimates can be deducted from the Fourier equation as [114]

$$t_{diff} = \frac{\rho_m c_p l^2}{k}. \quad (5.11)$$

The diffusion time of the used system is at the order of milliseconds. That means that the thermal equilibrium is established milliseconds after the application of signal. Since the frequency of an applied signal was much higher than $\sim 1 \text{ kHz}$, differential temperature change was neglected. Equation 5.9 then simplifies to a heat diffusion equation (2.15 in section 2.4.1, chapter II).

The resulting fluid motion produced by the electric field acting on the conductivity and permittivity gradients is calculated by using the Navier-Stokes equation for an incompressible Newtonian fluid. The equation is based on a continuum hypothesis which assumes that the number of molecules is large (i.e. statistical average is valid).

The applicability of the continuum theory can be checked by introducing the Knudsen number:

$$K_n = \frac{\lambda}{L}, \quad (5.12)$$

where λ and L are respectively the mean free molecular path and the characteristic length of a system. The continuum theory applies for system with Knudsen number less than 0.01 [158]. For a water molecule at room temperature and pressure $\lambda \approx 10^{-7}$ and so the continuum theory applies for geometries of 10 μm (smallest dimension used in these studies) and larger.

In addition it is important to determine the type of flow in the system i.e. establish the Reynolds number. Latter is defined as the ratio between inertial and viscous forces and consequently quantifies the relative importance of these two types of forces for given flow conditions. Reynolds number can be calculated using the following equation:

$$Re = \frac{\rho v l}{\mu}, \quad (5.13)$$

where ρ is the density, v is the average velocity through a system with a relevant length scale l and μ is the viscosity.

The flow is laminar (viscous forces dominate over the inertial ones) if the Reynolds number is less than 2300. For a system, designed in the simulation the Reynolds number was determined to be few orders of magnitude smaller than 1, so the flow was assumed to be laminar which simplifies the Navier-Stokes equation to Stokes equation. Mathematically the Stokes flow is given by

$$\mu \nabla^2 \bar{v} + f = \nabla P, \quad (5.14)$$

where f is the body force produced by the electric field acting on the conductivity and permittivity gradients (equation 2.23 in the theory chapter) and P is the pressure.

Another important aspect of a numerical simulation that solves partial differential equations is the boundary conditions. In the simulation, produced in this chapter three sets of boundary conditions were set to accommodate the electrical, diffusion and fluid flow problems.

For electrical part of the simulation, all vertical boundaries were set to electrical insulation. This condition sets the electrical current, normal to the boundary to zero. The electrodes were set to ground and a desired potential.

In another part of the simulation where the heat diffusion through the system was calculated, the top and bottom boundaries were assigned with the convective cooling so the heat produced by the applied signal is balanced out by the air in the room.

Finally the no-slip boundary condition was set between the fluid, contained within the channel and the glass and PDMS surface. The left boundary of the channel was selected to be an inlet and right boundary - outlet with a zero fluid velocity. The physical meaning of an inlet and outlet is the flow produced by external sources such as pumps connected to the system.

In order to validate that the electrical insulating boundary condition does not affect the electric fields (in the middle of the device) used for studies, the dimensions of the system were doubled. Similarly for diffusion, the width of the PDMS and glass were increased to see if latter had resulted in any changes on the observed temperature

rise. However, changing the dimensions of the system did not alter the results in the area of interest.

5.5 Results of the electric field effect on the bacteria

5.5.1 Effect of constant electric field on the bacteria

An investigation was carried out to see the effect of electric field, produced by a DC voltage, on the negatively charged bacterium. A simple experimental design consisting of a PDMS channel and four $\sim 400\ \mu\text{m}$ radius needles (with tips cut out) as electrodes was used. A small amount of PDMS was poured into a petri dish and left to semi-cure at room temperature for ~ 15 minutes.

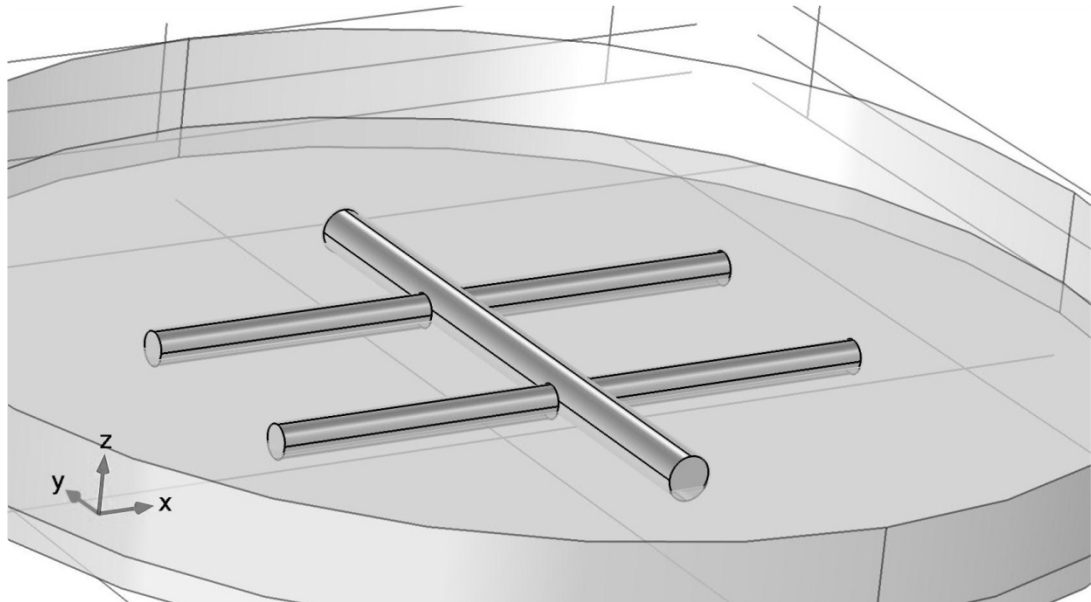


Figure 5.6. A schematic diagram of a device, used for the investigation of bacteria in constant electric field. The cylinders on the diagram represent the needles that were placed into semi-cured PDMS to position the channel and electrodes in the same plane.

This resulted in PDMS becoming hard enough to hold needles on the surface and in the same plane. Five needles were placed forming capital 'H' letter-like structure with the needle in the middle extending further to the left and right (figure 5.6).

More PDMS was poured over the structure, submerging it. The setup was left to cure for 8 hours at 65 °C in the oven. After curing, the needle in the middle was carefully removed, forming a channel between the 4 electrodes. The electrical connections were made at the rear ends (away from the channel) of the needles.

The experimental investigation has shown that bacteria, moving through such a system are repelled from the region, where the electric field is the strongest. Rather than stop, bacteria would move to the upper or lower channel wall, away from the plane where electrodes are and away from the focal plane of the microscope. Although this experiment proves that the electric field can change the direction of motion of the bacteria, large scales of the setup are impractical for microfluidic application. Smaller channels and electrodes need to be used instead. However scaling down a system with DC Voltage applied poses a threat of bubble formation. An investigation of the feasibility of the DC applied signal has been carried out by means of numerical simulation.

The simulation was performed using the geometry, similar to the one, shown in figure 5.4. Instead of finger electrodes, this time four rectangular blocks ($10\text{ }\mu\text{m} \times 5\text{ }\mu\text{m} \times 0.2\text{ }\mu\text{m}$) were placed $10\text{ }\mu\text{m}$ away from each other (see figure 5.7). The applied voltage was determined using the value for the electric field to stop the motility of *Pseudomonas Fluorescens* reported in literature [159].

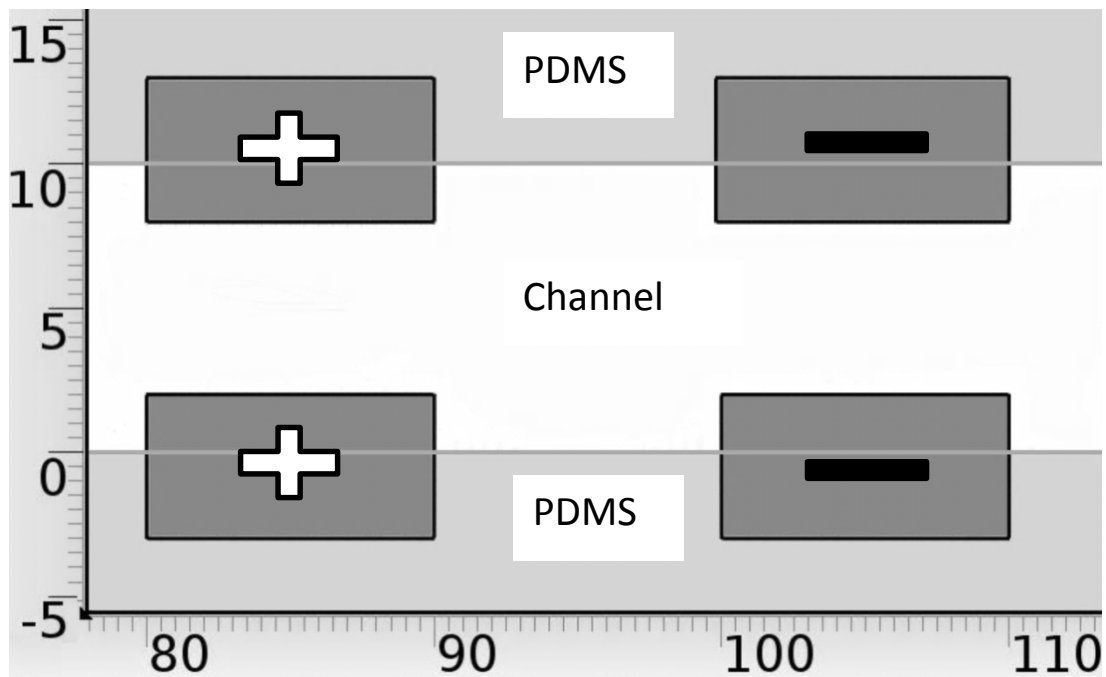


Figure 5.7. X-Y Plane view of the experimental setup for DC electric field manipulation of the bacteria.

According to a Comsol created simulation with the setup described above, for a channel that is 10 μm high and wide, as little as 0.01 Volts has to be applied in order to reach the electric field necessary to stop the motility of the bacteria throughout the entire surface area of the channel (between the positive and negative electrodes). Increasing the voltage by 2 orders of magnitude only resulted in $\sim 1^\circ\text{C}$ temperature increase. Parameter values (apart from signal frequency as DC field was applied) used for the simulation are given in the table 5.1. Electric current and Heat Transfer in Fluids modules were used for the purpose of the simulation.

5.5.2 DEP effect on the bacteria

Manipulation of various bacterial species using dielectrophoresis has been extensively studied in the past [96, 160-169]. These studies mainly concentrate on

separation of dead and alive bacteria or sorting different biological species. As shown in chapter 2, DEP force depends on the conductivity and permittivity of particle and medium through the Claussius-Mossotti relation. Hence it is important to know these properties in order to calculate the resulting force in a non-uniform electric field. Successful bacteria characterisation has previously been reported using dielectrophoresis [101-103], cross-flow filtration [170] or by repeatedly washing bacteria and measuring the difference in conductivities of the supernatant and the suspension [104].

The techniques described above, however, generally consist of centrifugation and washing of the bacteria, which exposes the micro-organisms to osmotic shock and may result in transport of water and other solutes through the membrane [171] affecting the conductivity measurements. Moreover the majority of reported experiments, where bacteria were manipulated with positive dielectrophoretic force, were performed either in distilled water of low conductivity or deionised water with adjusted salt concentration.

For a practical application it is important to manipulate bacteria in their natural environment rather than the one, convenient for DEP experiments. So the investigation of the effect of a non-uniform electric field on *Pseudomonas Fluorescens* bacteria was carried out in Luria Broth (LB) – a nutritionally rich medium that supports the growth of the bacterial species. The conductivity of this medium was measured to be ~16.8 mS/m and the investigation was carried out over the range of frequencies between 10 kHz and 20 MHz with a set of voltages from 2 to 20 Volts (peak-to-peak). The dominant effects acting on bacteria were Brownian motion (at low voltage) and AC Electrothermal fluid flow.

Negative DEP was inconstantly observed at ~ 7 MHz and 6 Volts peak-to-peak input signal. According to [114], at similar frequencies the induced flow experiences a change in dominant force from Coulomb (at low frequencies) to dielectric (at high frequencies) which results in smallest value of fluid velocity. When the field was switched off, no clear indication of motility of the trapped bacteria was observed.

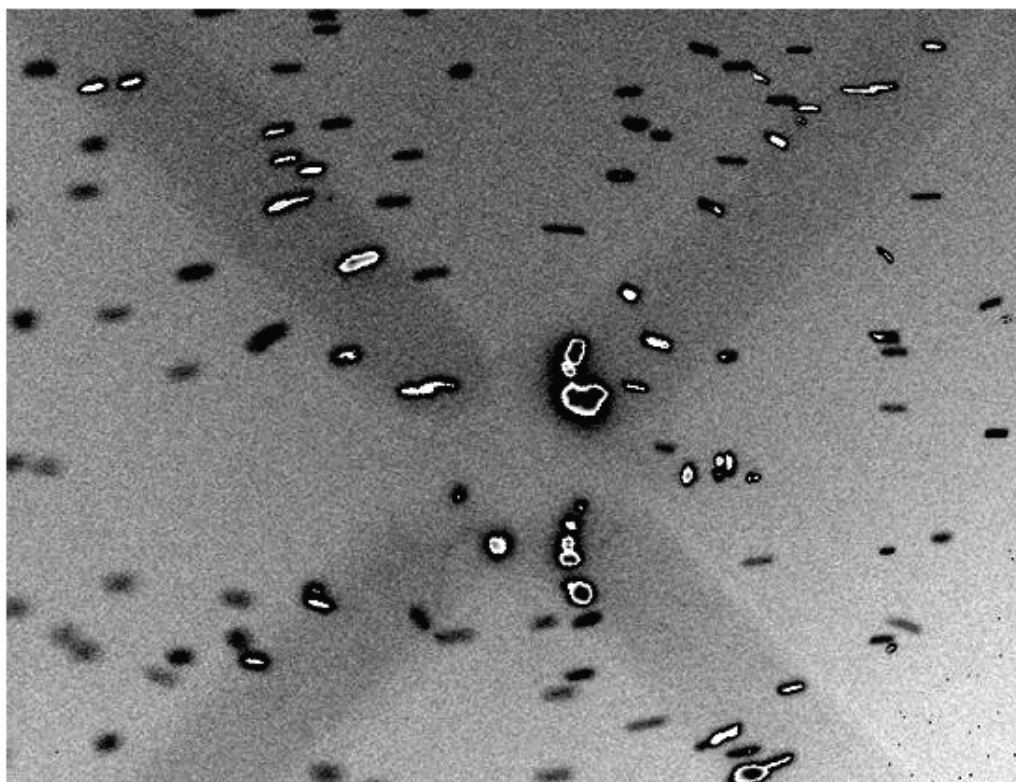


Figure 5.8. Trapping of the non-motile bacteria by positive DEP in capillary and ACET produced fluid flow in a channel over the polynomial electrodes. The applied signal was 500 kHz and 8 Volts peak-to-peak. Once switching the electric field off, the bacteria gets dragged by fluid flow away from the electrodes.

Bacteria were later grown in LB medium with altered salt concentration (reduced the amount of NaCl in a mixture) and resulting conductivity of 7 mS/m. When analysed under the microscope the bacteria in this colony grouped together forming ‘clumps’. Positive DEP of motile bacteria could still not be observed over a large frequency and voltage range. Similar clumps are also formed in original LB broth after some

time. This is a result of the amount of nutrients in the solution becoming insufficient. It is interesting to note, that when experiments were done on clumps that contained non-motile bacteria, positive dielectrophoretic trapping was achieved over the polynomial electrodes as shown in figure 5.8.

5.5.3 ACEO effect on the bacteria

The first set of experiments was similar to the DEP experiments as described in chapter 4. An aliquot of 7 μ l of *Pseudomonas Fluorescens* bacteria with optical density of 0.68 was pipetted on to microfabricated electrodes of different geometries (finger and polynomial). A coverslip was placed over the solution forming a chamber. An AC signal with different frequencies and amplitudes was then applied to investigate the dominant electrokinetic effect on bacteria. In the mS/m conductivity region, both ACET and ACEO produce a similar circular motion around the electrodes [130, 172].

Observing the motion of bacteria in the low voltage region (2 to 5 volts peak-to-peak) with a range of frequencies from 2 kHz (frequency low enough to accommodate ACEO) to 1 MHz (where no ACEO is present) significant changes in the behaviour were not detected. As discussed in [35] from experimental observations, the streamlines of the fluid were above the electrodes rather than approximately midway between electrodes (figure 5.9) suggesting ACET was the dominating electrokinetic effect rather than ACEO.

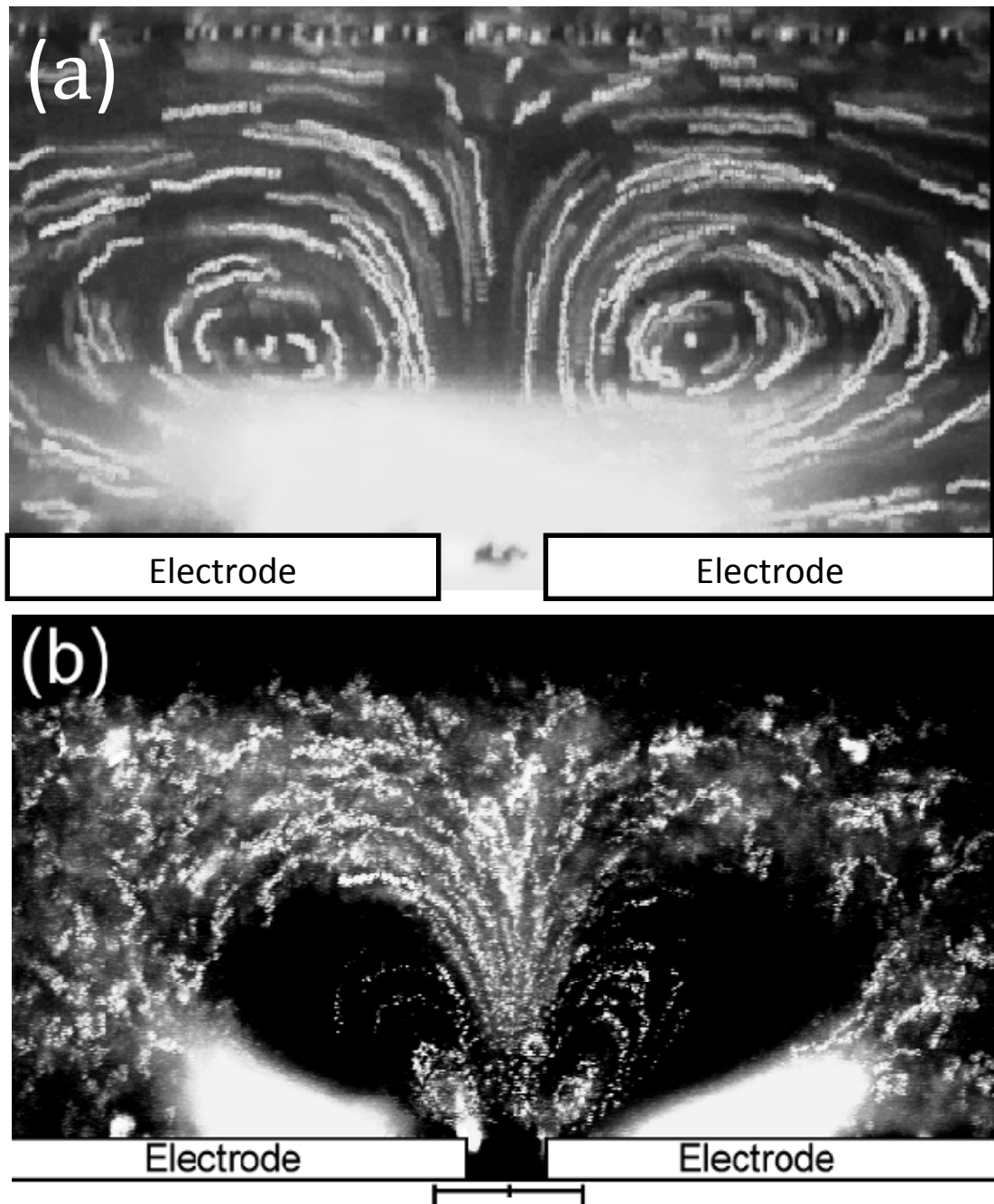


Figure 5.9. Fluid streamlines obtained by superimposing successive frames of a video of particle motion driven by AC electrothermal flow (a) and AC electroosmosis (b). The images (a) and (b) were reprinted from [35] and [172] respectively.

The direction of the streamlines at low frequencies for both ACEO and ACET are similar. This limits the information that can be extracted from the experimental observations. It is however known that at high frequencies ACEO is not present. The

magnitude of the ACET also does not change for a frequency range between below kHz region (where ACET is present) and few MHz (where ACET no longer takes place). For a second experiment a confined PDMS channel with fixed height of $\sim 8 \mu\text{m}$ and finger electrodes with $20 \mu\text{m}$ laser ablated gaps between $40 \mu\text{m}$ gold strips were used (see figure 5.4 for the illustration of the setup). No capillary force was present so that the direct comparison between the fluid velocities at different frequencies could be established.

The experimental investigation has been carried out using 50 kHz (using lower frequencies caused bubble formation in the solution) and 1 MHz frequencies. The direction of the fluid motion remained the same for both frequencies and no significant changes in velocity at 50 kHz and 1 MHz have been observed. It was concluded that for the frequencies that can be used in the experimental setup described, no ACEO is present. This is consistent with the previously published findings [117].

5.5.4 ACET effect on the bacteria

The effect of ACET flow produced by polynomial and finger electrodes on the bacteria moving inside the channel has also been investigated. According to a numerical simulation the flow, produced by the electric field, exhibits a circular profile as shown in figures 5.10, 5.11 and 5.13b.

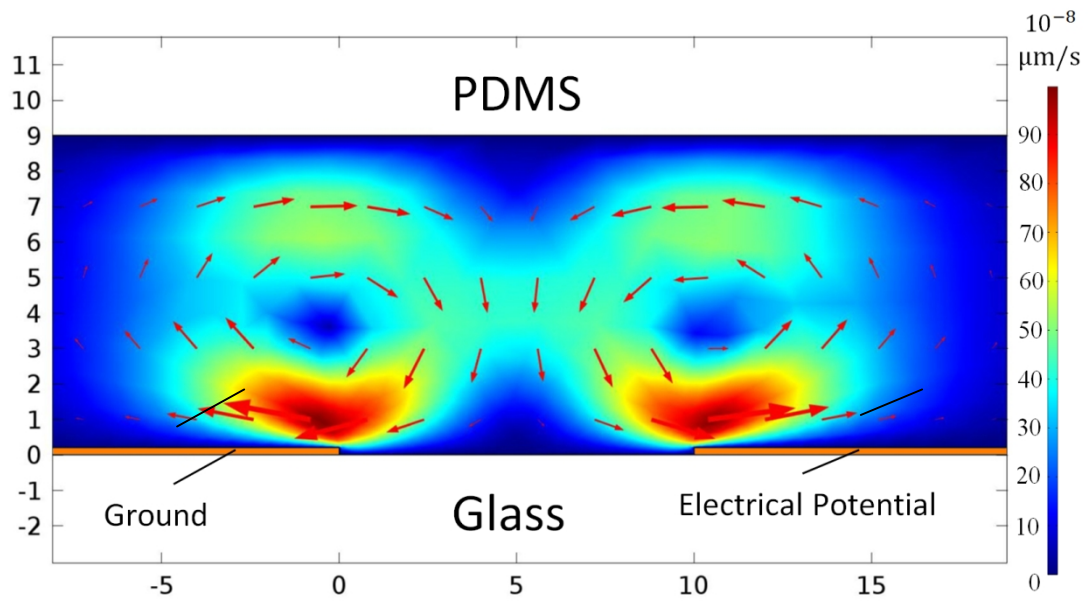


Figure 5.10. A two-dimensional simulation of the AC electrothermal flow above the finger electrodes inside the PDMS channel. The arrows represent the streamlines of the induced fluid flow.

For a two-dimensional cross-section of the finger electrodes, the flow is symmetric and acting in the opposite directions around the middle of the gap between the charged electrode and the grounded one. This motion is more complicated in actual three-dimensional structure (figures 5.11 and 5.13b).

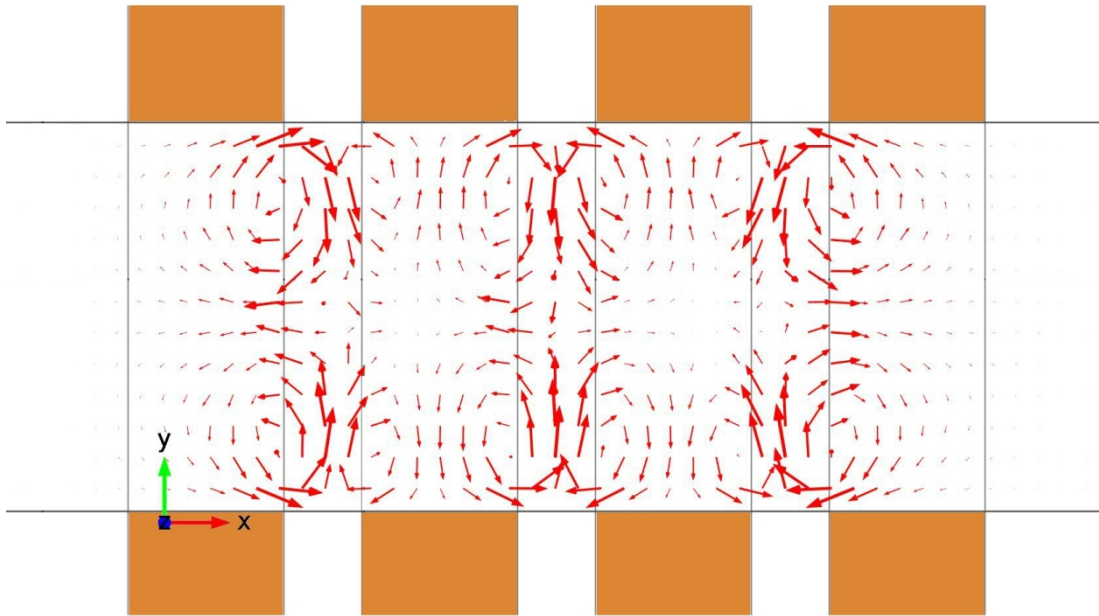


Figure 5.11. The simulated streamlines around the finger electrodes observed from the top (x-y projection) in the middle of the PDMS channel ($5\text{ }\mu\text{m}$ away from the electrode surface in z direction).

The experimentally observed tracks of the motion of the bacteria in channel over the set of finger electrodes are shown in figure 5.12. Upon switching the electric field, the motion would either slow down or completely reverse the direction, depending on the magnitude of the capillary force and the voltage applied.

As shown in figures 5.10 and 5.11, the circular flow produced by the electric field around the charged electrode and the grounded one are the same in magnitude but act in opposite directions. The overall observed effect (combination of capillary force and ACET force), however, is that when the field is switched on, the bacteria move with similar velocities throughout the entire channel, i.e. no clear distinction between the velocity near the positive electrode and the ground is distinguished.

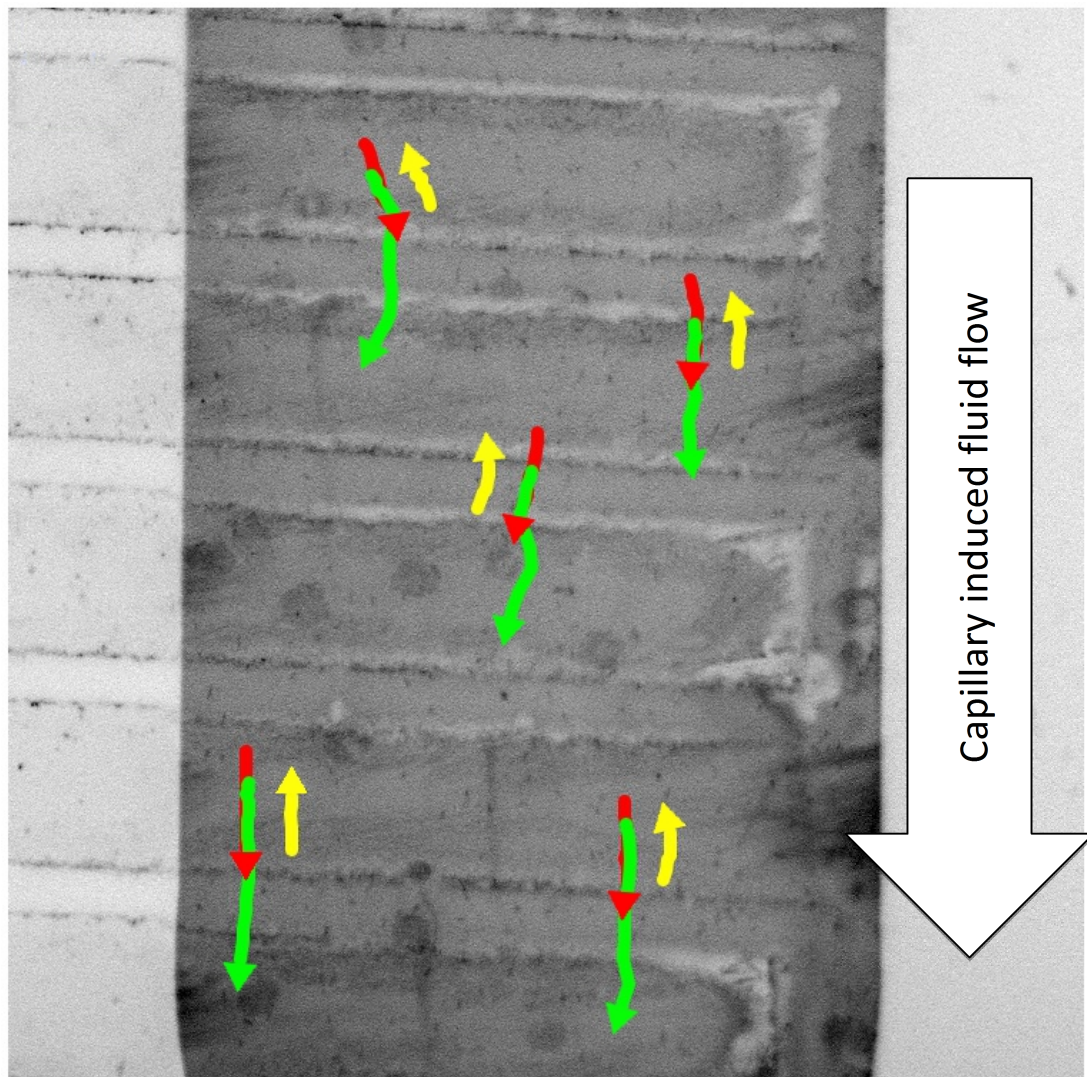


Figure 5.12. The motion of the bacteria inside the PDMS channel above the finger electrodes. The red and green arrows indicate the direction of the motion before the electric field was switched on and after the field was switched off respectively. The yellow arrows display the tracks of the bacteria motion when the 15 V peak-to-peak 5 MHz signal was applied. These yellow arrows were deliberately drawn a small distance away from the actual motion path for illustration purposes as the tracks of the motion with and without electric field overlap.

Similar experiments were carried out with the polynomial electrodes. At low voltages (below 8 V peak-to-peak) the bacteria, which were moving through the channel due to capillary force, would exhibit clear circular motion around the electrodes as shown in the figure 5.13a. This motion matches with the simulated motion around the polynomial electrodes (figure 5.13b).

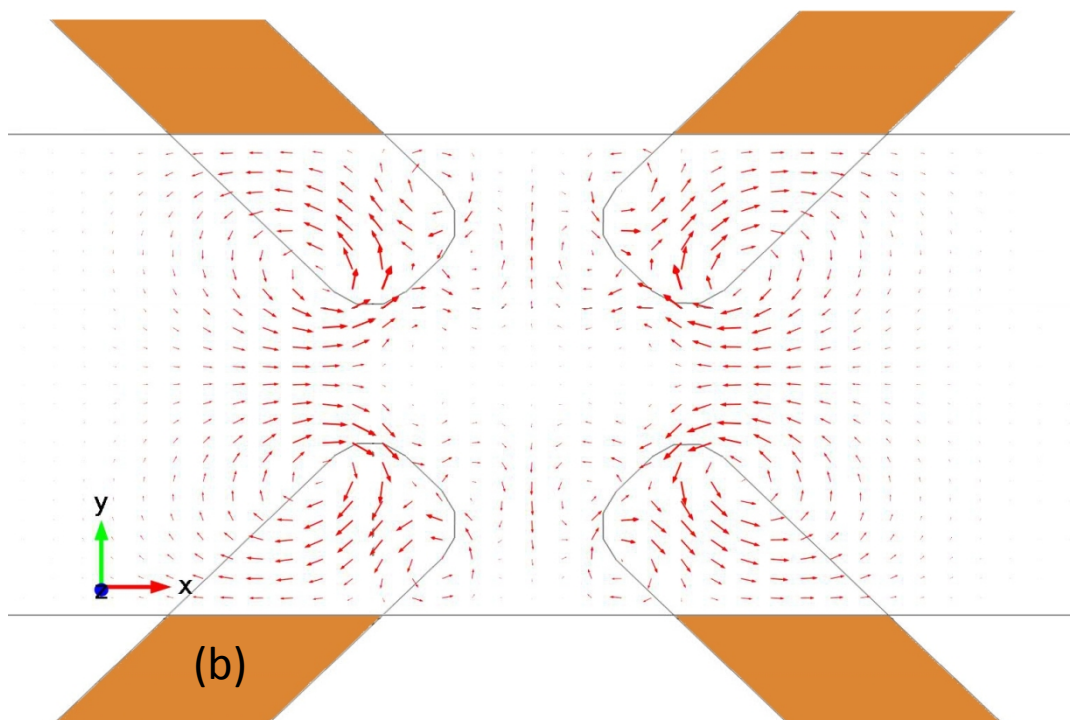
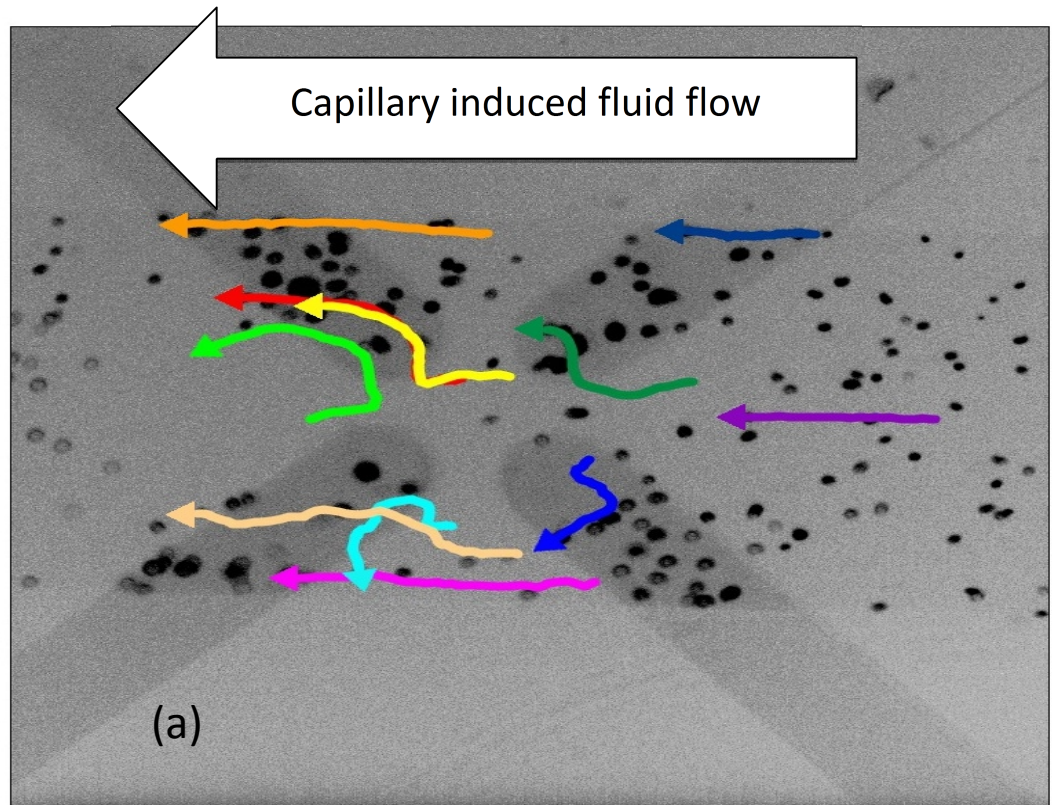


Figure 5.13. Tracks of the bacteria motion inside the PDMS channel induced by the capillary force and the 8 V peak-to-peak 5 MHz applied signal (a). Also shown is the x-y projection of the simulated streamlines of ACET flow in a polynomial electrode setup (b).

Although the desired effect of preventing the bacteria motion in a certain direction has been achieved using the finger electrodes and the PDMS channel, the dominating mechanism that hinders the motion is believed to be caused by drying of the fluid which is not useful for a practical microfluidic device. According to recent studies on pumping using ACET, unidirectional, non-circular flow can be achieved using microgrooved channels [122, 173]. However, fabrication of such electrodes is beyond the scope of this work. An alternative method that uses PDMS channel topography is investigated in 5.5.5 instead.

5.5.5 Proposed design for a channel geometry

A simulation-aided design of the channel that would result in a more controlled motion produced by Joule heating in an electric field has been developed and is shown in figure 5.14. The development of such a channel would require a silicon master with channels of different heights.

The frequency response of such device is consistent with the data, typical to ACET flow [130]: up to MHz region the velocity stays constant at has the highest magnitude. Increasing the frequency up to ~12 MHz reduces the magnitude of the flow. At even higher frequencies the direction of the flow reverses and the magnitude increases until at ~30 MHz it reaches a saturation. Increasing the voltage and decreasing the size of the channel increases the velocity of the fluid flow.

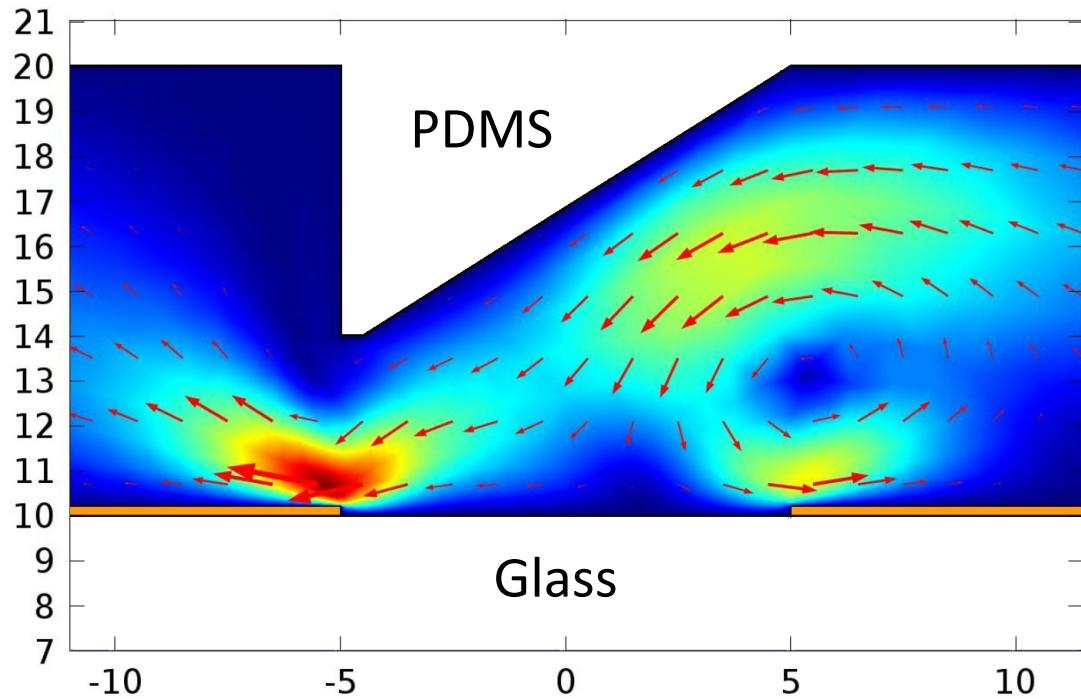


Figure 5.14. Simulation of the fluid flow in a modified PDMS channel with 5 Volts RMS applied signal. Details of other parameters used for simulation are given in table 3.1. Maximum velocity (dark most red colour above left electrode) was 9.28×10^{-6} m/s. Scales in x and y direction represent physical dimensions in μm .

Other parameters that effect the resulting fluid flow are to do with the geometry of the topographic PDMS channel and it's position with respect to electrode edges. As illustrated in figure 5.10, typical motion, produced in the channel contains symmetric circular motion above the electrode edges. By inserting the PDMS "block" above the electrodes the undesired back flow (streamlines from left to right) above the left electrode can be eliminated and significantly minimised above the right electrode. The efficiency of such device can be described by the resulting velocity and ability to minimise the undesired flow.

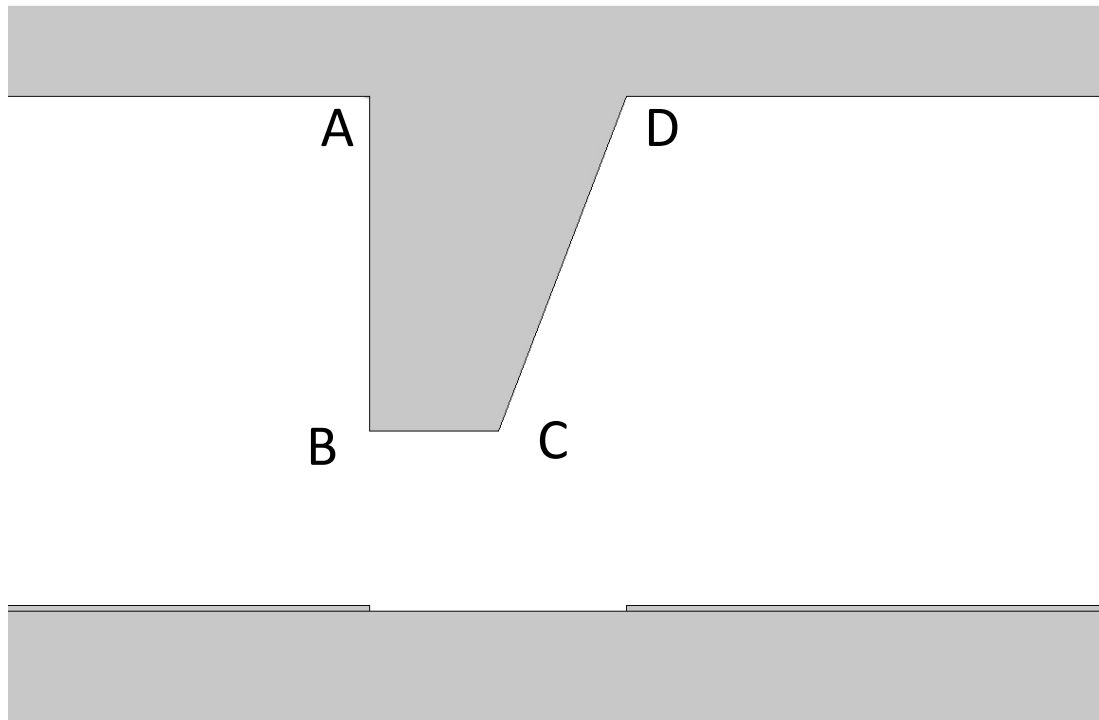


Figure 5.15. A schematic diagram of the PDMS block geometry

In figure 5.14 the block of PDMS is located directly above the gap, between the electrodes. Displacing the block to the right produces the circular motion above the left electrode as well as increasing the velocity of the undesired flow above the right electrode significantly reducing the efficiency of the device. When the block is displaced to the left, the magnitude of the desired flow was increased. It was also noted that the circular flow above the left electrode was minimised. Such displacement also had a negative effect as the "back flow" above the right electrode was also increased.

The efficiency of the device was also noted to be dependent on the physical dimensions of the block (AB and BC, figure 5.15). According to a Comsol simulation, as BC increases, the length of AB also has to be increased to avoid the undesired back flow above the left electrode. Lowering the block towards the

electrodes, however, has a negative effect - increase in the back flow above the right electrode. When $BC=AD$, the flow becomes symmetrical (line of symmetry is in the middle of the gap between the electrodes) as shown in figure 5.10. In order to optimise the flow, BC should be reduced which allows a reduction in AB as well. Note that as BC tends to zero, the smallest value of AB that allows unidirectional flow tends to a half of the channel width.

In addition, the region with high electric field is produced at the edge of the PDMS just above the left electrode. This can be further utilised for trapping as discussed in insulator-based dielectrophoretic devices [96].

5.6 Conclusion

A systematic study of the most commonly used electrical techniques to manipulate objects on micro scale has been performed on *Pseudomonas Fluorescens* bacterium. These techniques utilise both electric field produced by a DC input signal and an oscillating non-uniform electric field in standard dielectrophoretic setup. Upon the application of a constant electric field, negatively charged bacteria were repelled from the electrodes with a negative charge. A scaled down system for channels with $100\text{ }\mu\text{m}^2$ surface area and gold electrodes has been analysed. According to numerical simulation, for electrodes that are $10\text{ }\mu\text{m}$ apart, 0.01 Volts is sufficient to produce electric field that is strong enough to stop bacteria motility.

An alternative to using a DC signal is to use AC which is known to produce less Joule heating and also to provide more control of the particle manipulation in the solution. Commonly used AC electrokinetic techniques are dielectrophoresis, AC

electroosmosis and AC electrothermal flow. All three were experimentally investigated to see the effect on bacterial species.

When bacteria were subjected to a non-uniform electric field, the effect of the dielectrophoretic force could hardly be detected. Bacteria are living organisms with a sophisticated structure as discussed in 5.1. When placed in a medium with a salt concentration different to its natural habitat, the cell wall experiences osmotic pressure. As a result the bacteria adapts to the new environment. It is believed that these factors result in a small difference in the conductivities of living bacteria and its surrounding medium which is necessary for dielectrophoretic manipulation. However, when non-motile bacteria were observed, positive DEP trapping could be achieved.

Using the setup for DEP experiments it is possible to produce a fluid flow either due to the double layer around the electrodes – ACEO, or due to the temperature induced conductivity and permittivity gradients – ACET. These forces operate in media of different conductivities. For LB broth as used in experiments, clear ACEO effect could not be identified. Instead, ACET induced fluid flow was visible over the whole range of voltages and frequencies.

Using a numerical simulation, the design of a modified channel to optimise the ACET effect has been proposed. It can be adapted for a more complex system such as the Venice waterways and act either as a pump to push the bacteria in a controlled manner or act as a traffic system to prevent motion in specific directions. DC systems can also be used in such structures to act as a traffic system, preventing the motion of bacteria.

The observed effect of DC, ACEO and ACET match the data presented in literature. The exact dielectrophoretic response of the bacteria in LB broth would require a

more sophisticated model however it was clear that pDEP could not be observed for *Pseudomonas Fluorescence* bacteria. The significance of these findings is that electric fields combined with PDMS fabrication could be used to advance the studies on bacterial behaviour in spatially confined environment that represents its natural habitat.

Chapter VI: The Effect of Electric Field on the Behaviour of Molecular Motors

An experimental setup that supports the application of high electric fields without damaging the proteins on the surface is developed. This setup is used to analyse the effect of the electric field on the motility of the protein molecular motors. The experimental data is used to develop a numerical simulation that enables calculating parameters such as the forces that protein exert during the motility and quantify the motor distribution on the surface.

6.1 Introduction

Molecular motors are biological molecular machines that produce mechanical work through conversion of chemical, electrical or optical energy [174]. This is a very diverse and large class of nano to micro-sized machines that can be divided into chemical, DNA-based and protein-based molecular motors. Protein motors can be further sub-divided into ATP-based rotary motors (F_0F_1 – ATP synthase family and bacterial flagellum) and linear protein motors (kinesin, myosin and dynein superfamily). Non-biological (synthetic) molecular motors have also been recently manufactured.

In this chapter linear protein molecular motors are investigated with particular interest in actin-myosin II system. An introduction and the insight of their behaviour through the energy conversion cycle are presented first. The fundamental difference between various types of motors is also explained through the concepts of the processivity and the duty cycle in 6.2. This section also contains a list of applications molecular motors have.

One of the applications that was recently introduced includes integrating the highly efficient molecular motors into lab-on-a-chip devices. This application requires the understanding of motor distribution on the surface (list of currently used detection techniques is given in 6.3) and precise control over the directionality of the filament motion. The comprehensive review on the filament guiding techniques is presented in section 6.4.

It is also important to qualitatively determine motor distribution on the surface (i.e. determine the number of active and ATP insensitive motors) for a practical

microfluidic device. Using an elaborate experimental setup that allows the application of an electric field without hindering the motility with harmful products (section 6.5) the filament behaviour was observed. Upon application of the electric fields higher than 4 kV/m negatively charged filaments started orientating and move towards the cathode. Another effect of the external field was an increase of the sliding velocity on all tested surfaces. The simulation that takes into account all the forces that significantly contribute to the filament motion was developed.

By combining the experimentally obtained data and the simulation it was possible to determine the number of motors on different surfaces as well as the forces that myosin molecules exert on the filament. The detailed description of the model is presented in section 6.6.

Another numerical simulation was done to mimic the motor distribution on the surface for a known motor density. This enables determining the motors that are close enough to the filament to interact with it. The results of the numerical simulations are shown in 6.7 and the conclusion on the results obtained in this chapter and the implication of this work is given in 6.8

6.2 The molecular motors

Protein molecular motors (also called biomolecular motors) are naturally evolved machines that are present within many living organisms. They consist of amino acid (stimulus responsive) polymers that undergo dramatic conformational changes as they bind and hydrolyse ATP. These changes result in mechanical movement,

essential to many biological functions like cell division, transport of vesicles and muscle contraction [175]. Recent advances in molecular imaging, single molecule manipulation techniques (such as optical trapping) and development of motility assay prompted experimental investigations on molecular motors mechanisms [176-186]. Extensive theoretical analysis on their behaviour according to established physical, chemical and biological principles have also been presented [187-194]. In particular, biomolecular motors have been of tremendous interest to biologists, biophysicists and physiologists due to their central role in biology. “Tens of thousands of publications describe biomolecular motors from the perspective of the natural sciences and biomedicine” [195].

In general, protein molecular motors consist of a filament that slides above the motor in a stepwise fashion. For a directed motion of microtubule above a kinesin motor, for example, about a thousand amino acids are arranged in a specific sequence, forming a structure that allows ATP hydrolysis, conformation and affinity changes. The energy efficiency of this system can be higher than 50%, exceeding the efficiency of a diesel car engine [195]. High energy efficiency and small scales gave rise to a new avenue of research that investigates motors in an engineering and device-oriented context by means of the *in vitro* motility assay [71, 175, 196-200]. The motility assay has been conducted using two approaches: gliding motility assay, (filaments are moving over the stationary motors figure 6.1a) and bead geometry (the motors are introduced to a stationary filament figure 6.1b and c).

6.2.1 Types of motility assays

Bead geometry: in this case a filament (i.e. actin filament or a microtubule) is trapped (by absorption) to the surface while the motors are immobilised on the spherical particle - “bead” (figure 6.1b). Using optical tweezers, the bead is transported close to the filament, so that the motor and filament could interact. By calibrating the system, the displacement of the bead can reveal fundamental parameters of the system, i.e. the unitary step size and force exerted by the motor [180-182]. Alternatively, the filament can be trapped by optical tweezers and moved to a bead (or motility supporting surface) with the motors on it (figure 4.1c). This setup allows calculating same parameters as before, as well as the unbinding force that is required to “free” the filament from the motor that is in rigour state [201, 202] (bond between the actin filament and ATP insensitive motor). This geometry is mainly used to gain more insight on how motility occurs as well as to quantify the parameters of the system.

Gliding motility assay: The gliding geometry (figure 6.1a) or “inverted geometry” consists of a motility supporting surface coated glass cover slip (could be other surfaces like silicon oxide), motor proteins immobilised on this surface and filaments that move along the motors. For such system the filaments would move randomly across the entire motor covered area with a velocity that depends on the density of motors, temperature, the amount of ATP, ADP and phosphate in the solution [203-205]. The effect of surface hydrophobicity has also been reported to affect the gliding velocity [199, 206].

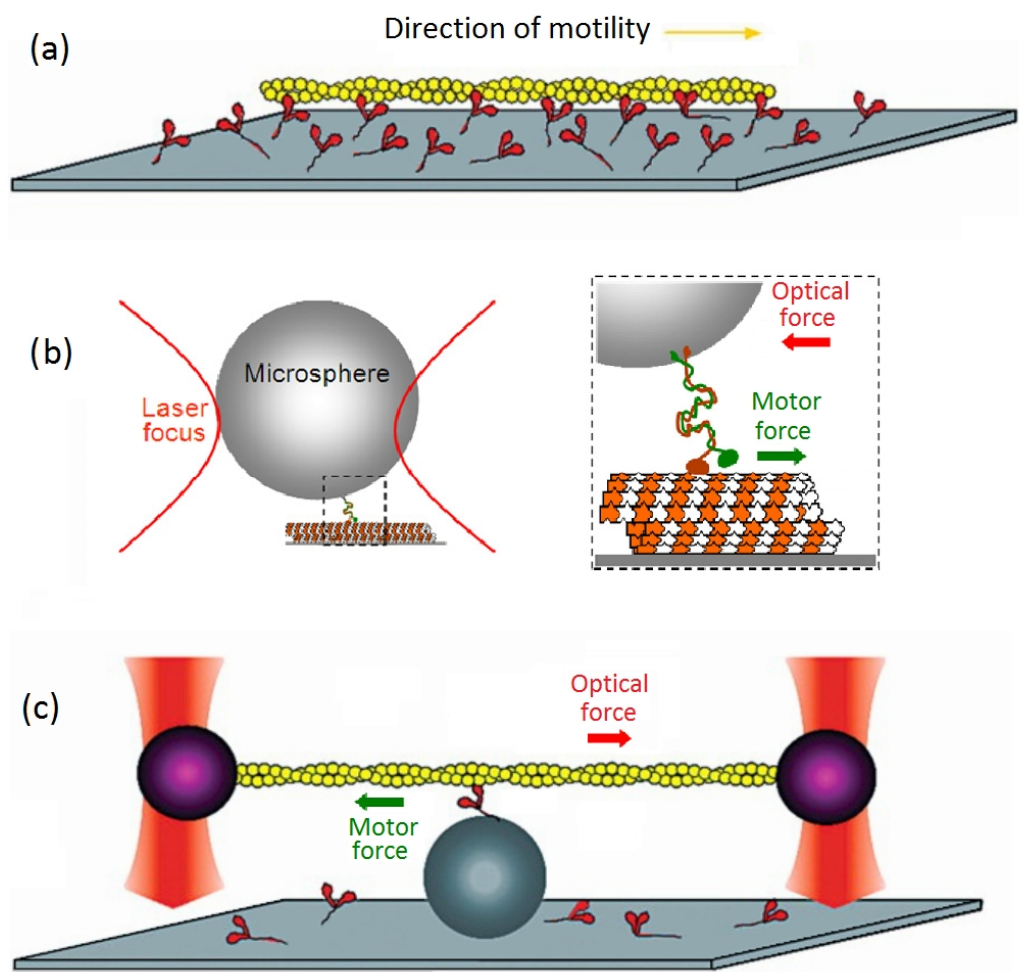


Figure 6.1. A schematic diagram of gliding motility assay (a) and bead geometry (b) and (c). Helical structure in (a) and (c) represents an actin filament interacting with myosin motors. Cylindrical structure in (b) is a microtubule, absorbed to the surface, while kinesin coated microsphere is moved to close proximity with microtubule for a motor and the filament to interact. Laser trap of kinesin coated microsphere (b) was reprinted from [195]. The original black and white illustrations of *in vitro* actin-myosin motility (a) and laser trapped actin filament (c) were adapted from [207] and [180]. The colours were added in [208].

6.2.2 Operating principle of molecular motors

As mentioned earlier, molecular motors produce mechanical motion by means of energy conversion. For linear molecular motors, which are of primary interest in these studies, the source of energy that is further converted to motion is ATP. The

full cycle of ATP binding, hydrolysis and the release of ADP and phosphate is demonstrated in figure 6.2. This biochemical cycle is coupled with the cycle of conformational changes as well as binding affinities to the filament. The coupling between these three cycles occurs by means of mechanical communication between elements in the protein structure [209] and results in the motion of the filament.

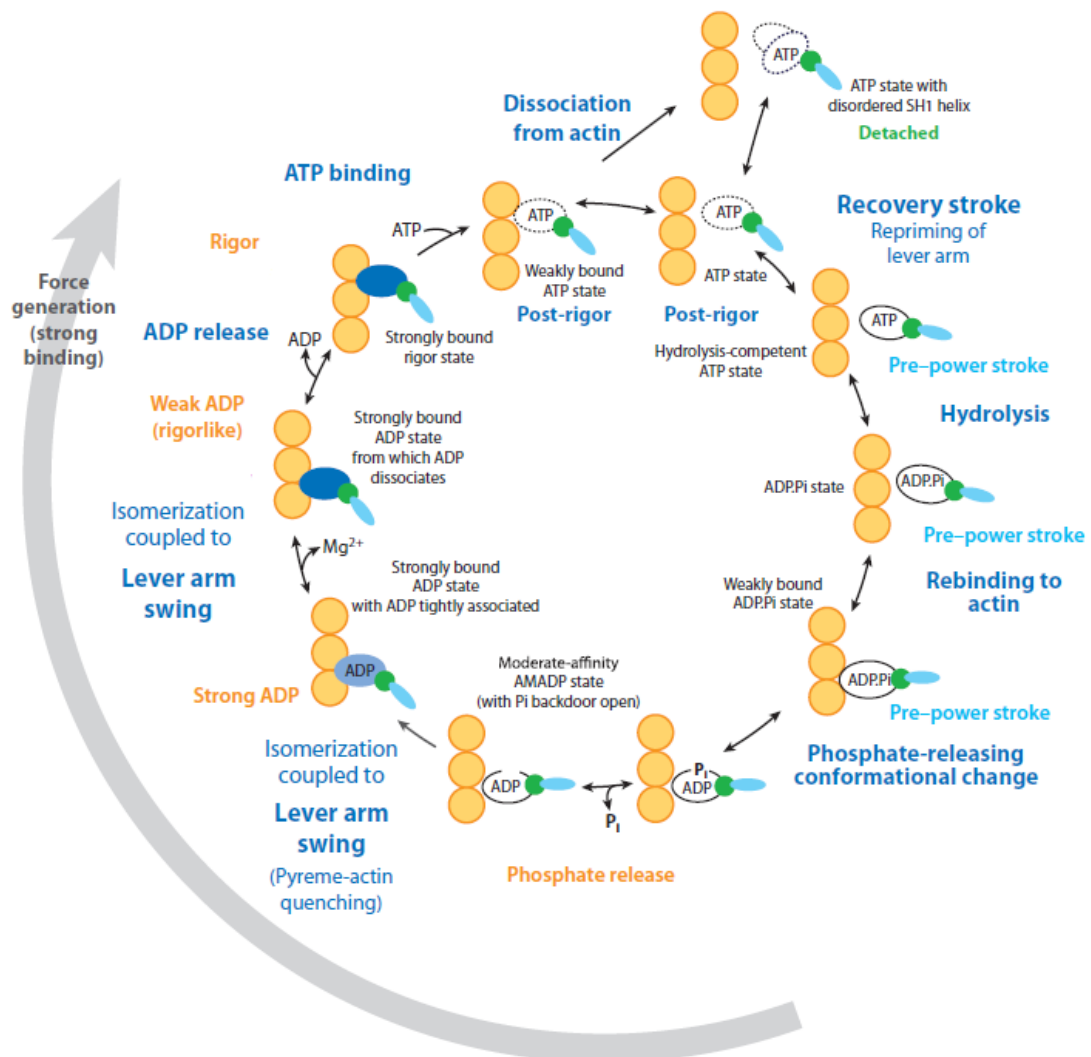


Figure 6.2. A schematic diagram of a full ATPase cycle of the interaction between the actin filament and the myosin motor. This interaction involves changes in conformation, nucleotide-binding state and actin affinity. The figure was reprinted from [210].

The motility of actin-myosin II system, which is used for further experimental and simulation work, can be explained by analysing the interaction of the filament and the motor according to the state of a motor. When ATP or other products of hydrolysis (i.e. ADP and inorganic phosphate) are bound to the myosin, a motor has a weak affinity for actin. This is referred to as weak binding state (post-rigour and pre-power stroke states figure 6.2). When an inorganic phosphate is released, the affinity of a motor increases by several orders of magnitude [211, 212]. This results in a strong bond between the motor and the filament (crossbridge), which is maintained even after ADP is released. When the ATP molecule later binds to the motor, myosin dissociates from the actin filament, returning to weak binding state. The cycle is then repeated. Myosin muscle motors *in vivo* operate in huge arrays. For example, a muscle fibre can have around a billion myosin molecules. Even within a sarcomere (a basic unit of a muscle) there are thousands of myosin-containing thick filaments, each having ~600 crossbridges, acting in parallel [192].

6.2.3 Processivity of molecular motors

In contrast to muscle myosin motors, the conventional kinesin molecules operate in small numbers: using electron micrographs it has been shown that only a few crossbridges between kinesin and microtubules are required for continuous motion [213]. The difference in the numbers of crossbridges for different motors can be explained by analysing their speeds and processivity, which in a context of linear molecular motors mean continuous interaction of a filament with the same motor.

Using *in vitro* motility assay it has been shown that a single molecule of kinesin can continuously move along the surface of a microtubule for over a hundred of 8 nm steps without detaching [176, 214]. Other evidence that kinesin is a processive motor is that “gliding microtubules swivel about a single point on the surface (at which the motors is presumed to be located)” [192]. In addition kinesin hydrolyses on average 125 molecules of ATP, following the initial binding to the microtubule [215], consistent with the motor taking 125 steps before detaching. The speed of this type of motors is independent of motor density and the length of the filament [214].

As opposed to kinesin, myosin II is a non-processive motor. It has been shown that the minimum concentration of ~ 600 HMM molecules/ μm^2 is required to move actin filaments, longer than 1.1 μm [216]. “Below this threshold, the filaments do not associate with the surface for long enough to detect the motility” [192]. In other words, because the interaction between the filament and the motor is very brief, there has to be a sufficient number of motors on the surface for filaments to move without detaching from the surface due to Brownian motion.

For completeness’ sake a third type of linear molecular motor – dynein should be mentioned. It is also important to clarify that within the kinesin, myosin and dynein superfamilies there are both processive and non-processive types of motors. All references to kinesin are made considering the processive type of these motors.

6.2.4 Duty cycle of molecular motors

The functional differences between different motors (i.e. processivity and speed) can be understood through the concept of duty ratio. In the context of linear molecular motors, the duty ratio r refers to the fraction of time that each motor spends attached to the filament τ_{on} with respect to full ATPase cycle τ_{total} .

$$r = \frac{\tau_{on}}{\tau_{on} + \tau_{off}} = \frac{\tau_{on}}{\tau_{total}}. \quad (6.1)$$

The conformational changes that result in the motion of the filament take places during τ_{on} . The minimum number of heads, required for continuous movement N_{min} depends on the duty ratio according to the equation 6.2

$$N_{min} \geq \frac{1}{r}. \quad (6.2)$$

This number guarantees that there will be at least one head bound to the filament [217-219]. For example, a single kinesin molecule with 2 heads is able to maintain a continuous attachment to a microtubule. This means that the duty ratio of each head has to be at least 0.5. For myosin II this value can be as low as 0.04 [218]. Low duty ratio and relatively large working distance (or stroke distance, see figure 6.3 for illustration) result in much faster motion of non-processive motors provided there is enough motor molecules immobilised on the surface to support continuous motility.

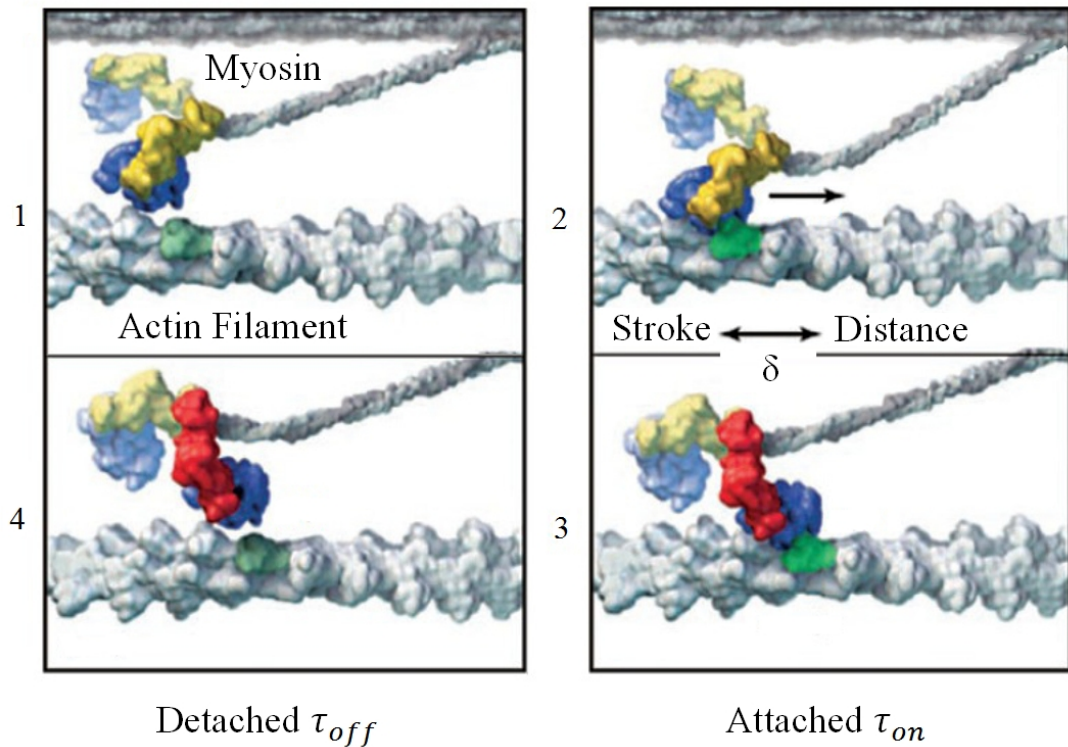


Figure 6.3. A Schematic diagram of the interaction between the myosin head and the actin filament. As a result, the filament moves a distance equal to the stroke distance of a lever arm δ . The motor moves towards the binding site (1), attaches to the filament forming a crossbridge (2). Upon hydrolysis of ATP molecule, lever arm experiences conformational change that results in the motion (2) and (3). The motor then detaches from the filament (4). The figure was reprinted from [209].

It might be expected that this difference is attribute to differences in ATPase rates, but experiments on ATP “consumption” rates have revealed that this is not the case. For instance, skeletal muscle myosin can move ~ 10 times faster than conventional kinesin while having only half the ATPase rate [192]. Lowering the amount of ATP in the solution would, however, result in velocity decrease for both processive and non-processive motors.

6.2.5 Applications of molecular motors

One of the functionalities of molecular motors *in vivo* is the transportation of specific organelles and vesicles at large distances at a controlled rate at well-defined points in time. This poses a challenge of using *in vitro* motility for similar purposes. In order to mimic the biological transport mechanism, the functionality of existing motility assay has to be expanded. It is necessary to gain control over the directionality of the motility, be able to load and unload the filament with specific cargoes and activate the motors in a controlled fashion. The system where all these tasks are achieved is termed “molecular shuttle” [220, 221]. These shuttles could serve as an alternative to scanning force probes [222] or template assisted self-assembly of objects on nano-scale [223].

Some other applications of the gliding motility assay include the transport of streptavidin-coated beads [221] and virus particles [224], the sorting of macromolecular assemblies [225] and the measuring of the force in pico-Newton range by assembling a forcemeter using kinesin and microtubules [226]. Alternatively molecular motors could be used as micropumps [227], in biocomputation devices [152] and as means to probe and image the surface [228, 229].

6.3 Detecting the protein motors on the surface

Proteins are known to adsorb to a vast number of surfaces, both hydrophilic and hydrophobic [230, 231]. Various medical and biotechnological applications require specific protein-surface interaction such as localised absorption, adsorption in

functionalised conformations or even a complete prevention of protein adsorption to the surface. Even though the development of surface coatings and surface modifiers has provided us with a significant control over specific and non-specific adsorption [232-235] and systematic studies to understand surface-motor interaction have been performed [200, 206, 236-238], improvements are still necessary for practical biomedical [239] and biotechnological applications [240].

Another challenge is to be able to characterise the surface. That is to perform quantitative and qualitative analysis of the protein adsorption on the surface. For this purpose, a large number of techniques have been developed over the years. Some examples of these techniques are: Radiolabeling, Spectrometry, Ellipsometry, X-ray Photoelectron Spectroscopy (XPS), Surface Plasmon Resonance (SPR), Infrared Spectroscopy (IRS). Some of the single molecule detection techniques include AFM, STM and SEM.

Quartz crystal microbalance (QCM) is also a technique that can be used to detect protein adsorption to the surface [154, 241-244]. The operating principle of QCM is that piezoelectric material (such as quartz crystal) oscillates with the applied potential. The frequency of oscillation is measured as a function of mass and as the motor molecules adsorb to the surface, the frequency of oscillation for the same applied potential decreases. This frequency decrease can be expressed by equation 6.3 [245]

$$f = -\frac{2f_0^2 \Delta m}{A\sqrt{\mu_q \rho_q}}, \quad (6.3)$$

where f_0 is the fundamental oscillation frequency, μ_q and ρ_q are the shear modulus of the quartz and density of the quartz respectively, A is the electrode area and Δm is the change in mass. Using equation 6.3 the mass of the absorbed proteins and subsequently the total number of motors on the surface can be calculated. However, not all of these motors participate in ATP hydrolysis. Some molecules that are adsorbed on the surface are “inactive”. This may be due to the structural damage of the protein which results in its inability to bind to ATP molecule. These inactive motors can still bind to the filament through a rigid bond which hinders the motility [201, 202].

The number of motors bound to a polymer-coated coverslip and participate in ATP hydrolysis can also be estimated. This value is obtained by comparing NH_4 -EDTA ATPase activities in flow cell with the values of control sample (of known amount of motors) in the solution. In the solution, the ATPase activities are determined calorimetrically based on the rate of inorganic phosphate release [246]. As a result a ratio between active and inactive motors on the surface can be obtained.

6.4 Guiding the molecular motors

Most of the applications, discussed earlier require the control over the motion of the filaments. A number of different techniques with different levels of success have been applied for this purpose. One of the ways to guide the motility is by using the surface topography. By “building” a wall on either side of the channel (figure 6.4a) it has been noted that filament guiding can be achieved [247, 248]. It has also been noted that the walls have to be of sufficient height, otherwise actin filaments and

microtubules would “climb” the wall [249] and either float into the bulk or start interacting with the motors adsorbed on the top of the wall. One of the ways to overcome this issue is to create 3-D confinement as illustrated in figure 6.4(b).

In addition, in order to induce the unidirectional motion, spatially restricted channels were formed in different geometrical shapes – rectifiers, providing up to 70% success rate [250]. The drawback, however, is that these elaborate systems with rectifiers occupy large areas thus compromising the miniaturisation.

An alternative to physical confinement that restricts the filament motion is eliminating or disabling motors on certain areas within the surface [247] (guiding using surface chemistry, figure 6.4c and d). Consider a filament as a flexible rod (although not entirely true, however the important aspect is that the Brownian motion is significant). While supported by motors, only the loose tip at the filament “head” region is affected by Brownian fluctuations. As the motors keep “pushing” the filament, the length of the loose end increases and so does the angle of swinging until the head reaches a motor molecule. Using surface chemistry techniques, it is possible to create a pattern with tracks that support motility and motor-free areas outside these tracks. For this setup, at the boundary between the two areas, the filament will either be forced to come back on track or float away from the surface unable to reach the motor molecule. Narrow tracks of a few nanometers have been generated to produce bidirectional motion. In addition, a combination of physical confinement and surface treatment can also be used [251, 252].

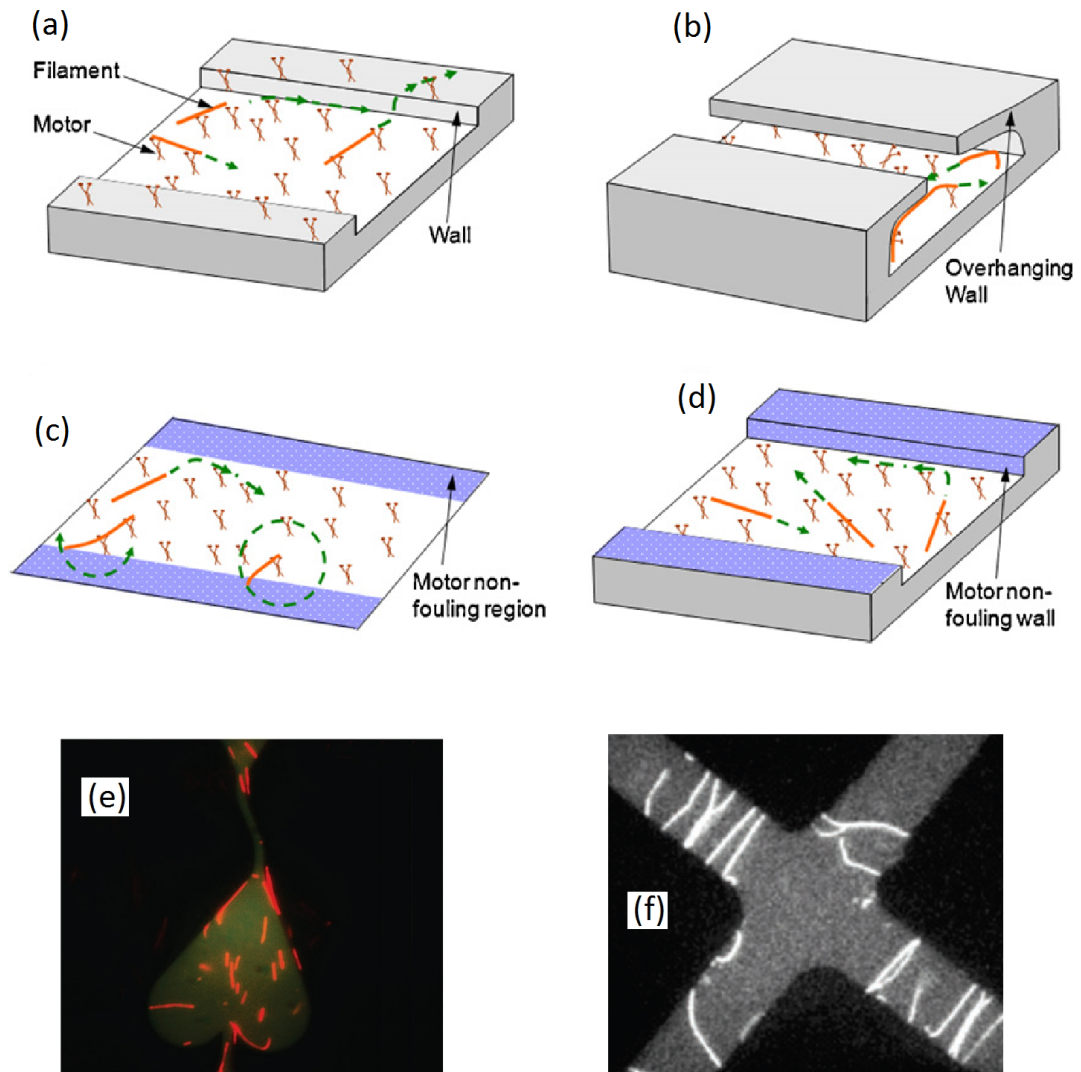


Figure 6.4. Illustration of some of the guiding techniques that are used to manipulate the directionality of the filament motility. (a) and (b) represent the physical confinement using the walls that restrict the channel. (c) and (d) illustrates the chemical modification of the surface. (e) and (f) show the rectifier geometry and DEP manipulation respectively. (a-d) were reprinted from [195], (e) from [253] and (f) was adapted from [254].

Alternatively, the alignment and guiding can be performed by forcing the tip of the filament to move in the desired direction (figure 6.4e and f). It can for example be achieved by external fluid flow [249]. Similarly, by functionalising the filaments with ferritic particles, magnetic fields can be used to guide the motility. Actin filaments are negatively charged, which allows the directing of the motility by means

of external electric field where electrophoretic force bends the loose tip of the filament in the direction of the cathode.

A dielectrophoretic system has also been reported to successfully orientate the actin filament [254]. In this case microfabricated electrodes were coated with a polymer surface that supports protein adsorption and motility. Upon application of the DEP force, the filaments would align and move in a bidirectional fashion.

6.5 *In Vitro* motility in the electric field

6.5.1 Materials and methods

In order to prepare the surfaces for actin-myosin motility glass cover slips were baked at 85 °C for 3 hours, then washed in ethanol and dried under a nitrogen flow. Nitrocellulose (NC) was deposited on the coverslip using 1% NC (w/v) dissolved in amyl acetate. The cover slip with the solution was then spin coated at 3600 RPM for 2 minutes. Similar procedure was done for 3 other surfaces: Poly(methyl methacrylate) (PMMA, average Mw=120000) 2% (w/v) in PGMEA; Poly(tertbutyl methacrylate) (PTBMA, average Mw=170000) 2% (w/v) in PGMEA and Poly(butyl methacrylate) (PBMA, average Mw=180000; Polysciences Europe) 1% (w/v) in toluene.

Alternatively, for the surface functionalisation with trimethylchlorosilane (TMCS), the glass coverslips were submerged for 5 minutes in dry acetone, methanol and chloroform. Later the coverslips were soaked in 5 % TMCS dissolved in chloroform

for 5 minutes. After silanisation cover slips were washed in dry chloroform, dried under a nitrogen flow and baked at 85°C for 1 hour.

The list of buffers and solutions, as well as the chemicals they consist of, that were used in the motility experiment is given below:

- LISS (buffer): 1 mM MgCl₂, 10 mM MOPS, 0.1 mM K₂EGTA, pH 7.4.
- L65 (buffer): LISS containing 50 mM KCl and 10 mM DTT.
- Assay solution: 1 mM MgATP, 10 mM DTT, 25 mM KCl and LISS with anti-bleach mixture containing 3 mg/ml⁻¹ glucose, 20 units/ml glucose oxidase, 870 units/ml catalase and ATP regenerating system containing 2.5 mM creatine phosphate and 56 units/ml creatine kinase.
- Blocking solution: 1 mg ml⁻¹ bovine serum albumin (BSA) in LISS buffer.
- Labelled actin: 10 µl of rhodamine phalloidin labelled actin filaments (rhodamine phalloidin was purchased from Invitrogen and actin was labelled according to manufacturer's protocol), 990 µl of L65.
- Blocking actin: 14 µl of unlabelled actin filaments, 986 µl of L65.

The protocol for actin myosin motility experiments is as follows:

- 1) 60 µl of heavy meromyosin (HMM; 120 µg/ml in L65) was applied to a flow cell containing the functionalised cover slip and incubated for 2 minutes.
- 2) The un-reacted binding sites on the cover slip were then blocked by applying 60 µl of blocking solution to the flow cell with the incubation period of 30 seconds.
- 3) The blocking solution in the flow cell was replaced with 60 µl of blocking actin (to block non-functioning HMM heads). After 1 minute of incubation,

excess blocking actin was removed by flushing the flow cell with 60 μ l of L65.

- 4) 60 μ l of labelled actin was further applied for 30 seconds. Excess labelled actin was later removed by flushing the flow cell with 60 μ l of L65.
- 5) 60 μ l of assay solution was applied. This solution contains ATP molecules necessary for motility to take place.
- 6) Finally The electrode chambers were also filled with assay solution and the electrodes applied to the sample.

For each surface filament guiding was imaged at field strengths in a range between 0 kV/m and 8 kV/m with an epifluorescence microscope (Zeiss Axio Imager.M1) fitted with an Andor iXon+ EMCCD camera at room temperature (23-35 °C).

The analysis of the videos was performed using the open source image processing program imageJ and the filament movement tracked using the plugin MtrackJ. Only those filaments that were fully motile, i.e. filaments that did not stop, or start moving, part way through the video, for the entire 50 frames of a video were tracked.

6.5.2 Experimental Procedure

The electric field was applied to the motility assay in a cell as shown in Figure 6.5. The actin filament motility occurs on a functionalized glass cover slip (Sigma-Aldrich), which is attached to a microscope slide via thin spacers, thus creating a classical flow cell [255]. Tall plastic cones, modified from pipette tips to hold copper electrodes at the top, were placed and sealed, at the open edges of the flow cell. The

chambers that house the electrodes keep the possible electrolysis species created during the experiment that are harmful to the acto-myosin system, e.g. hydrogen, oxygen and radicals, contained and separated from the actual motility chamber.

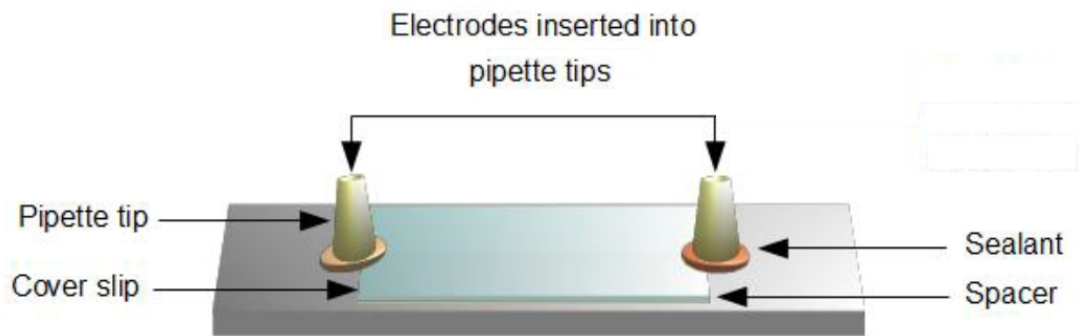


Figure 6.5. An illustration of the experimental setup used for the electrical guiding of the motility

Considering the relatively large distance between the electrodes (5 cm), this design results in the creation of essentially parallel electric field lines in the middle section of the cover slip where the observations were made. As a result all the filaments and motors experience a similar electrophoretic force, both in amplitude and direction.

6.5.3 Forces acting on the filament

The motility of the filaments is governed by a combination of all the forces that act on it. One essential feature of the non-processive motors, such as myosin II, is that a certain population of the motors that interact with the actin filament are pushing it in the direction of actual movement (active force). While the others, possibly due to the orientation of the motor molecule, oppose this movement thus effectively creating a resistive force. Another source of resistive force is the ATP-insensitive motors that attach to the filament with rigour bonds. The drag force of the fluid is also present

but it has been determined to be insignificant [256-258] and thus is not taken into consideration when developing the motility model.

The significance of a resistive force can be checked by applying the external electric force on the actin filament. The velocity due to electric field is given by [71, 198].

$$v = \frac{\beta \eta l_f E}{q} \approx E \mu_0, \quad (6.4)$$

where β is a dimensionless shape dependent factor, η is dynamic viscosity, l_f is the filament length, q is the total charge of actin filament and μ_0 is the electrophoretic mobility.

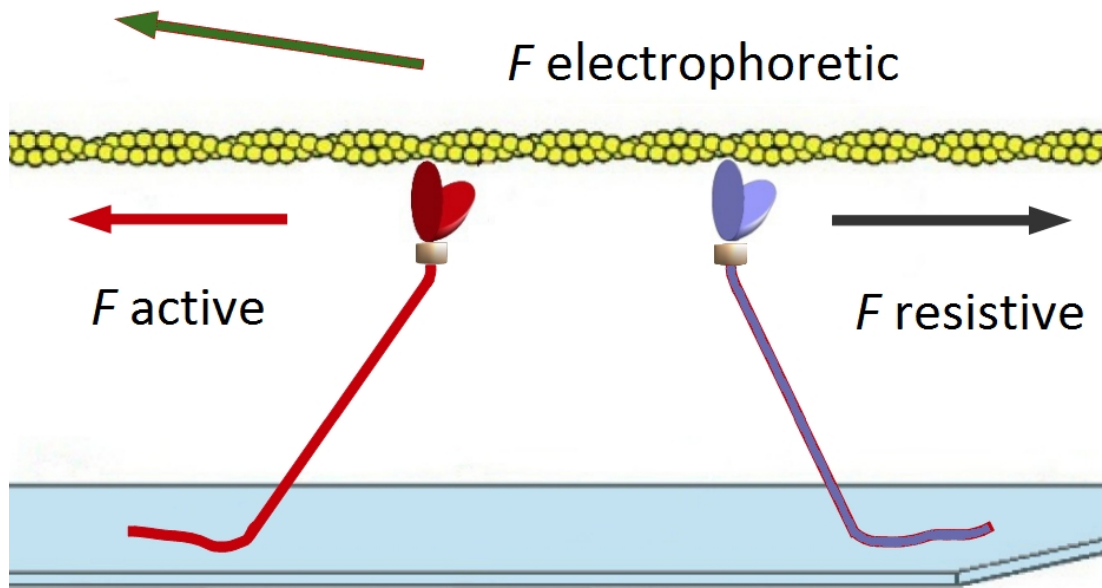


Figure 6.6. A schematic diagram of the forces, acting on the filament during the motility in the electric field

If there was no resistive force that acts on the filament, it can be inferred from equation 6.4 that the electric field at which the filament would move at a constant

sliding velocity of 15 $\mu\text{m/s}$ is $\sim 6 \text{ kV/m}$. This implies that when motility limiting factors are solely consisting of hydrodynamic drag and weak binding of molecular motors (assuming that a strong-binding cross bridge detaches immediately after their power-stroke) then at electric fields $\sim 6 \text{ kV/m}$ the observed velocity (with sufficient ATP present) should be $11 \mu\text{m/s}$ (v_{max} of conventional motility assay). This value, however, is much larger than the one observed experimentally (table 6.1).

6.5.4 Effect of the electric field on motility

Electrical motility experiments have revealed that the application of an electric field translates in an increase of the velocity of the movement and its guidance towards the positive electrode (table 6.1). Some filaments were observed to move against the direction of the field towards the negative electrode, but the majority of these eventually made U-turns towards the positive electrode.

Experimentally obtained angular distribution of the filament motion was also analysed. The direction of the parallel electric field lines were considered as 0 degrees. This direction coincides with the direction of the x axis of the M-track plugin of the ImageJ software used. By comparing the x and y coordinates of consecutive frames, the angles are determined.

The average angle θ is shown in table 6.1. The physical representation of θ is the angle between the average direction of the motion of the filament and the direction of the electric field that acts on it.

Note that the data, presented in table 6.1 represents the data that was used for the simulation. The graphs of the velocity profile of the actin filament at different electric fields on all surfaces are presented in the appendix.

Table 6.1. Experimental velocity data of actin filament motility over myosin coated surface at various electric fields. Data on average angle between the electric field and the direction of filament motion is included.

	E=0	E=2kV/m	E=4kV/m	E=6kV/m	E=8kV/m
	<i>v</i> , $\mu\text{m/s}$	<i>v</i> , $\mu\text{m/s}$; θ	<i>v</i> , $\mu\text{m/s}$; θ	<i>v</i> , $\mu\text{m/s}$; θ	<i>v</i> , $\mu\text{m/s}$; θ
NC	4.13	4.22; 62	5.09, 44	6.33; 26	7.82; 6
TMCS	4.51	4.74; 45	5.71; 23	8.23; 14	10.81; 11
PMMA	8.03	8.15; 53	8.65; 29	10.41; 17	11.13; 10
PBMA	3.75	3.83; 58	4.52; 37	5.54; 13	7.14; 12
PtBMA	7.21	7.56; 57	7.97; 43	9.05; 17	10.09; 15

A significant velocity increase was detected at electric fields above 5 kV/m. The ratio of motile to non-motile filaments (table 6.2) also shows transition at similar value of the electric field. At small electric fields (up to 6 kV/m) there is a marginal increase in the ratio between motile and non-motile filaments. However, between 6 and 8 kV/m the ratio dramatically increases. This indicates that when the electric field is approximately 6 kV/m the force exerted upon the filaments becomes large enough to overcome the forces due to a population of resistive myosin heads.

Table 6.2. The percentage of motile filaments on various surfaces at different electric fields.

	E=0, %	E=4 kV/m, %	E=6 kV/m, %	E=8 kV/m, %
NC	27.9	30.6	34.3	66.9
TMCS	31.07	38.7	44.44	80.48
PMMA	39.5	42.08	46.28	60.26
PBMA	22.1	25	27.14	41.98
PtBMA	31	31.9	33.8	51.6

The measured temperature of the cover slip during the sweeping on-off of the electric field does not vary importantly, as the temperature remains within ± 0.2 °C and so the increase in velocity is solely attributed to electrophoretic force.

6.6 Model description

The commonly presented relationship that describes the velocity of an actin filament as a function of a number of motors it interacts with is shown in equation 6.5

$$v = \eta \times V_0 \times [1 - (1 - f)^{N_a}], \quad (6.5)$$

where V_0 is the velocity during the power stroke, f is the probability that the interacting head undergoes a power stroke and the term in square brackets represent the probability that the filament is propelled by at least one out of N_a active heads [259, 260]. η (< 1) is an abstract coefficient, defined as the force transmission efficiency that presumably takes into account the resistive forces described before. However this model is insufficient to qualitatively explain the difference in velocities obtained for different surfaces (table 6.1).

Consider a single myosin molecule immobilised on the surface such that both lever arms can interact with the filament, the full ATPase cycle for each arm takes 50 ms [261, 262] and the arms do not act simultaneously. From the model design point of view these arms (active arms) have 2 states: bound state and detached state.

During the detached state the lever arm has no effect on the filament motion (this is not entirely true, however, the contributions of weak bonds were ignored as they were reported to be a few orders of magnitude lower than strong bonds [263, 264]).

Upon binding to the filament the lever arm undergoes a conformational change which results in the filament motion. When designing a model it was assumed that the bond lasts for 2 ms (4% [218, 261, 265] of 50 ms ATPase cycle) [198, 261] and if at least 1 lever arm is at this state, the filament is moving with maximum velocity as the contribution of hydrodynamic drag as already discussed is insignificant. The value of 11 $\mu\text{m/s}$ [266] has been used as the maximum velocity, which is in a good agreement with other reported data [175, 217, 267].

Numerically, the velocity during the 50 ms cycle with 1 myosin molecule interacting with the filament, would be 11 $\mu\text{m/s}$ for 4 ms (each myosin molecule has 2 lever arms) and 0 for the remaining 46 ms when the arms are detached.

	1	2	3	4	5	6	7	8	9	10	11	12	...	49	50
M1															
M2															
M3															

Figure 6.7. A schematic diagram of the interaction between 3 myosin molecules M1, M2 and M3 (each having 2 arms) with the filament. The time slots [1-50] are the ATPase cycle and the coloured blocks represent the randomly assigned time when the filament and the lever arm interacts.

During the actual motility tens of myosin molecules can interact with the filament to accommodate the continuous motion. The graphical visualisation of the motility produced by 3 motors is shown in the figure 6.7.

The filament in such system would move at a maximum velocity for 10 ms and remain stationary for other 40 ms of the cycle. The resulting velocity can be calculated as $0.2 \times v_{max} = 2.2 \mu\text{m/s}$. As shown in figure 6.7 between 1 and 4 ms the action of lever arms overlaps. This overlapping becomes more significant when the larger number of motors is used.

Numerical implication of this overlapping is the requirement of a very large amount of simulations for the result to converge. It was decided to simulate every 0.1 of a millisecond which allowed a much faster convergence. The simulations were designed in a way that the 50 ms cycle is represented by 500 time units of the simulation with 20 time units reserved for the power stroke of the lever arm. The velocity has been also scaled accordingly. 20 cycles were used for 1 second of the simulation, where the time for power stroke of each arm was randomly assigned within 1-480 time instances of each cycle. The average number of motors that act in each of 20 cycles remained the same but the time instances when the interaction between the lever arm and the filament occurred would change.

When an external field is applied, the negatively charged filaments experience a force due to the electric field. The actin-myosin bond during the power stroke is very strong and it is assumed that the electric field has no effect during the stroke period. When all lever arms are detached, however, the motion is given by the electrical mobility of the filament taking into account a contribution of non-hydrodynamic friction due to the proximity of actin to the surface [198].

The value of maximum velocity takes into account the work done by the motor to push the filament against the viscous load. The value, determined for electrical mobility also takes into account resistive forces imposed by friction. So when designing a model it was further assumed that the motility is only hindered by the presence of the resistive motors on the surface (consistent with [198]). Similar to active motors, the time frame when the resistive motors act on the filaments are randomly assigned. The resulting system consists of active and resistive motors as well as the external field which constantly acts on the filament.

Table 6.3. An Illustration of simulated motility mechanism. At time instances 20 and 160 the filament moves due to conformational change of the lever arm. At 40 and 140 the filament is dragged by the electric field. In this example the force due to electric field is the same as the active force (unity). It acts only once to help overcome the resistive force produced by a single rigour bond, which is 5 times larger. At time instance 120, two active arms (2^*) act simultaneously to overcome resistive force

Time	F_{act}	F_{res}	E	Motile
21-40	1	0	0	✓
41-60	0	0	1	✓
61-80	1	5	1	✗
81-100	1	3	0	✗
101-120	0	2	0	✗
121-140	2^*	2	0	✗
141-160	0	0	1	✓
161-180	1	0	0	✓

The Matlab designed simulation analyses the resulting effect on the actin filament at each time instance (0.1 ms). Before the resistive force is encountered, the motion is given either by the conformational change or by the electric field. Once the time instance when randomly assigned resistive force is reached, the filament stops moving. The active forces of the lever arms from the following time frames are then added to overcome the resistive force. The motion is re-established at the frame

when the resulting active forces are stronger than the resistive force. The summary is shown in table 6.3. The velocities are then added up for the entire second of the simulated motility and averaged over the number of time instances used.

The values of active and resistive forces in table 6.3 are shown for illustration purpose of how the motility is simulated. Using optical tweezers experiments, these values have been previously determined in literature. Clearly for a different number of active and resistive motors the resulting simulated velocity will vary. So by performing a simulation over a large range of active and resistive motors it is possible to quantitatively determine when the simulated velocity matches the experimentally determined ones.

Summing the resulting velocities at each instance and dividing it by the number of periods used for simulation gives an estimation of the average velocity value. The force generated by the external electric field has two effects. Firstly, it assists the force generated by the active motors for the filament to overcome the resistive motors. Secondly, it pushes the filament when it is only constrained by a weak binding of active myosin.

Table 6.4. List of the parameters used for the simulation

Parameter	Value
F_{active} per lever arm	1.7 pN [180, 268]
F_{rigour} per motor molecule	9.2 pN [201]
T_{cycle}	50 ms [261]
τ_{on}	2 ms [261]
Electrophoretic mobility μ_0	$2.5 \times 10^{-9} \text{ m}^2/\text{V} \times \text{s}$ [198]
Maximum sliding velocity	11 $\mu\text{m/s}$ [266]
Linear charge density λ_q	4 e/nm [269]

From the maximum velocity the stroke distance of $d=11$ nm per 1 ms can be deduced according to the detachment kinetics described in [261].

The model, written in Matlab, which simulates the movement of actin filaments on a myosin-covered surface under an externally applied force per cycle, is based on the following constitutive relationships:

$$v' = \begin{cases} \frac{\mu_0 E \times \cos(\theta)}{T_{cycle}}, F_{resist} = 0, F_{act} = 0 \\ \frac{d}{T_{cycle}}, F_{resist} = 0, F_{act} \neq 0 \\ 0, F_{resist} > F_{act} + F_E \end{cases} \quad (6.6)$$

and

$$v_r \times n = \sum_{n=1}^{n=20} \sum_{T=1}^{T_{cycle}} v', \quad (6.7)$$

where v' is the velocity at each time instance within the cycle, v_r is the resulting velocity, $\cos(\theta)$ is the angular component between the direction of filament motion and electric field, n is the number of periods used for simulation, d is the size of the stroke, performed by a lever arm, and $F_E = q \times E$ is the electric force that helps to overcome inactive motors, F_{act} and F_{resist} are the forces generated by the active motors and the resistive motors respectively.

When designing the model it was assumed that the direction of the motion is constant and is given by the average angle. This simplification ignores any Brownian fluctuations on the tip of the actin filament during the motility.

6.7 Simulated results

Considering the fact that the time instances when active and resistive forces take place are randomly assigned, the resulting velocity v_r for each simulation is different. Therefore, in order to compare it with the experimental values, an average of a large number of simulations, v_{Av} was used for all computational measurements. For the situation, when no resistive force is present, the velocity plot of the actin filament in electric field is shown in figure 6.8

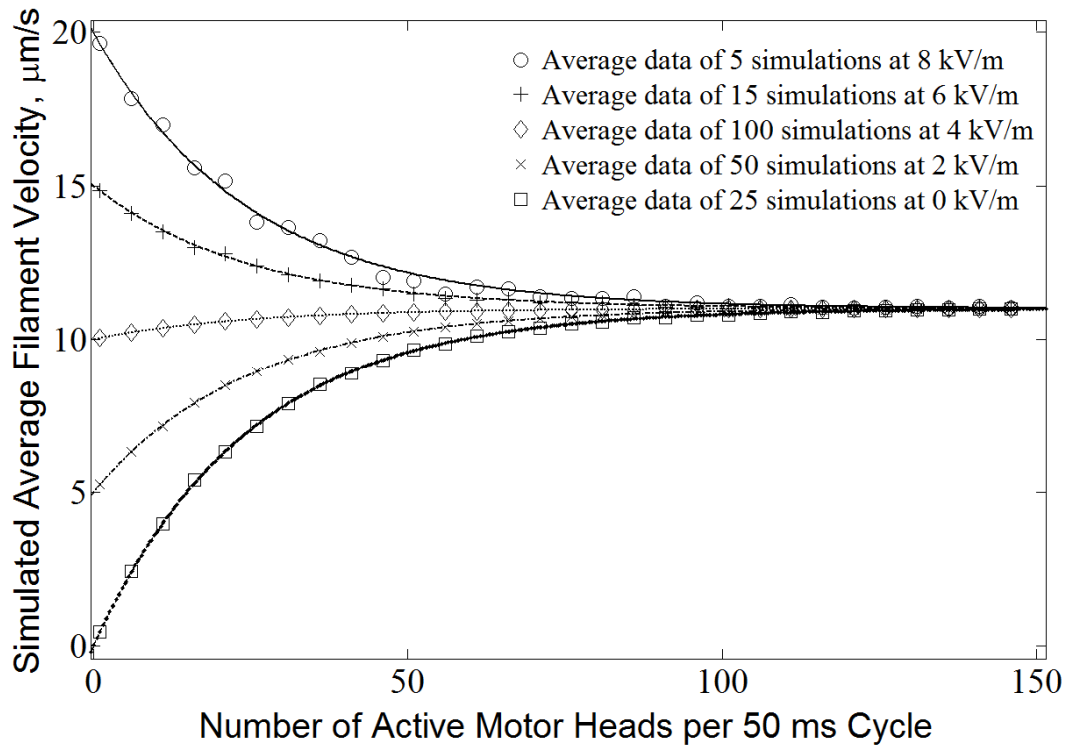


Figure 6.8. Simulated average velocity vs. number of motor heads interacting with the filament per single 50 ms cycle. The lines represent the fitted exponentials over an average of 500 simulations.

The difference between simulations is explained by the fact that more than a single head can bind to the filament at the same time instance. As the number of simulations increases the data set converges as illustrated in figure 6.8.

Assuming that the average number of motors acting on the filament on the same surface stays constant for all electric fields and the resistive force is attributed to rigour bonds (table 6.4) it is possible to calculate the ratio of active and inactive motors on the surface. This is done by comparing the simulated and experimentally obtained velocities (table 6.1). The simulation would take into account a range of active and inactive motors and corresponding electric fields. An example of a velocity plot for a range of motors is shown in figure 6.9.

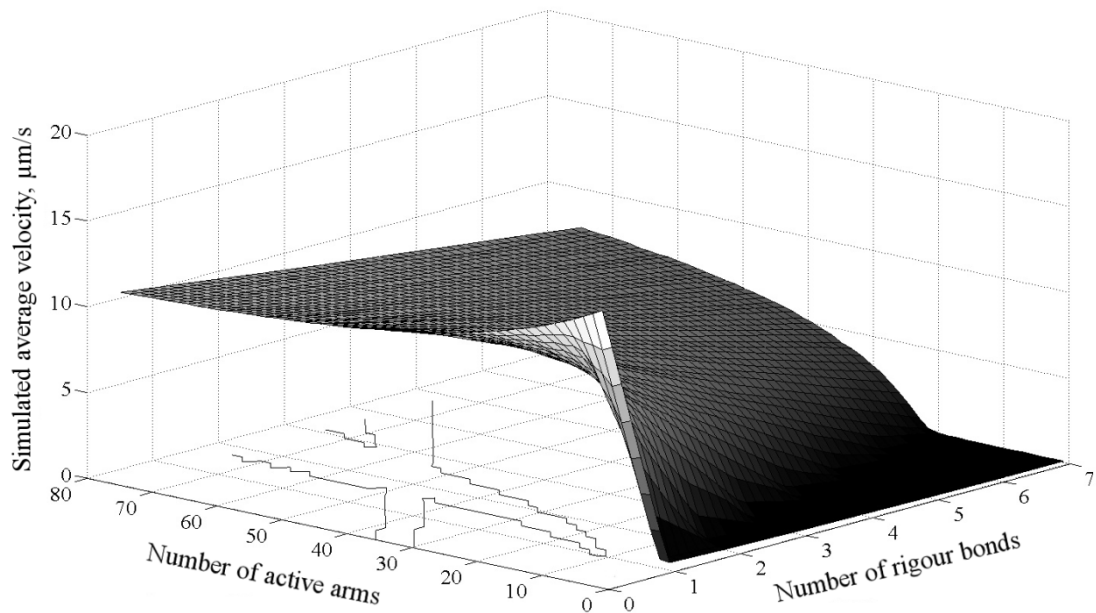


Figure 6.9. A simulated velocity surface plot for a range of active and rigour bound motors per single 50 ms cycle at 8 kV/m. The two projection on X and Y axis represent the motor pairs that accommodate the experimental velocity on PtBMA surface (table 4.1) at 0 and 8 kV/m within the 0.4 $\mu\text{m/s}$ range.

Similar velocity matrixes are produced for all fields and surfaces. The projection on x and y axis represents the motor pairs that accommodate experimental velocities under the same conditions (i.e. the same field and the surface) within 0.4 $\mu\text{m/s}$ range. The intersection area of all the projections at each field for a given surface represents

the active and inactive motor pairs that produce velocities, similar to the ones determined experimentally.

The simulation takes into account a whole number of active and rigour bonds. When matching these results at various electric fields with corresponding experimental values, a very small number of motor pairs are allowed. The summary of the motor pairs for all the surfaces is illustrated in figure 6.10. As expected, the lower increase in the velocity due to the external electric field is explained by a larger number of interacting motors.

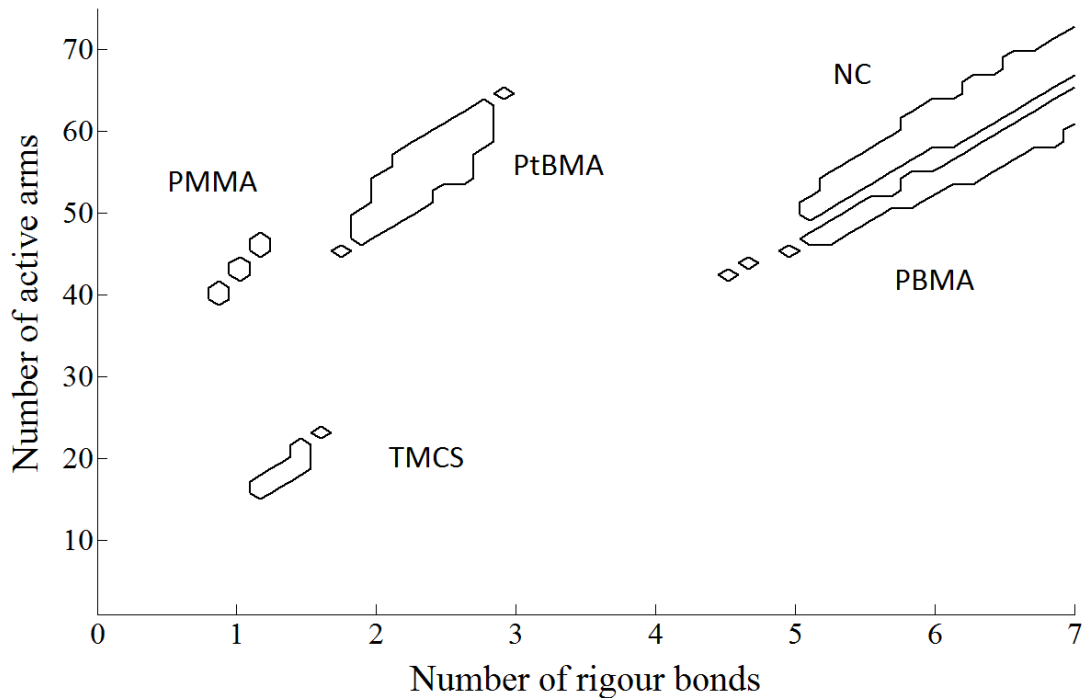


Figure 6.10. Simulated ratio of active and rigour motors per single 50 ms cycle that provides with velocities, similar to the ones obtained experimentally.

The simulated results on PMMA and PtBMA surfaces indicate the highest ratio of active motors. This is consistent with the fact that the experimentally obtained velocities when the electric field was not applied for these surfaces were highest. For

TMCS the least number of interacting motor molecules were determined and as a result the effect of an external force on the filament velocity on this surface was the most significant. Measurements on both NC and PBMA surfaces showed low sliding velocity with and without the external field. According to the simulation, this is explained by a large number of motors with a high ratio of inactive motors interacting with the filament during the motility.

So far by inputting various motility parameters and active and resistive forces of the motor molecules (table 6.4) it has been possible to estimate the number of motors that interact with the filaments on different surfaces. However, using the QCM technique, described in section 6.2 it is possible to determine the total mass and as a result the total number of the motors on the surface. Moreover, by measuring the rate of the inorganic phosphate release it is also possible to determine the value of active motors and hence the ratio of the total and active number of the HMM on the surface. If the number of motors that interact with the filament is known, it is possible to reverse the simulation to determine the forces, exerted by the myosin molecules on the filament (figure 6.11).

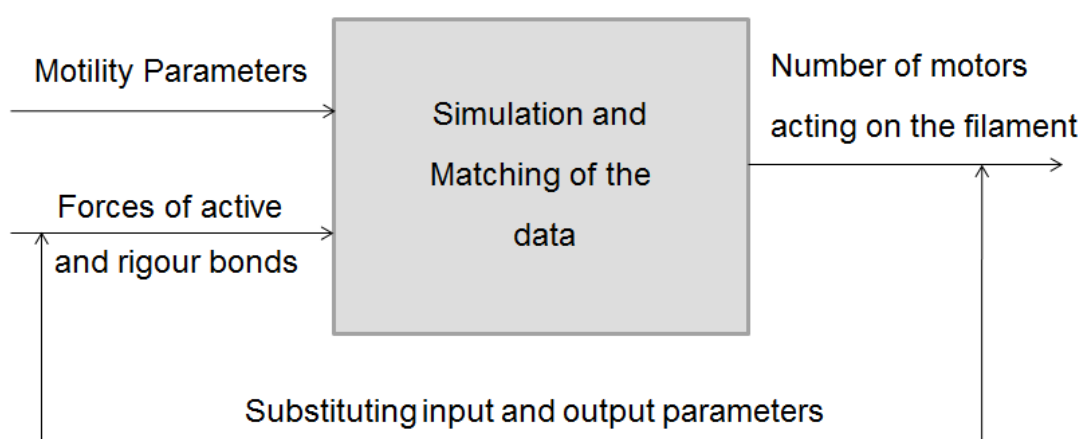


Figure 6.11. A schematic diagram of reversing the simulation of actin myosin motility.

Using the QCM experiments, a total number of motor molecules per $1 \mu\text{m}^2$ on the nitrocellulose surface was determined to be 1990, 1800 of which were active. These values are in a good agreement with previously reported measurements on the NC surface [260]. This results in a ratio of $\sim 10\%$ of inactive motors which is consistent with the simulation (figure 4.9). According to the band model described by Uyeda *et al.*, [259] the number of motors that interact with the filament N_m is given by

$$N_m = \frac{w_b \times \rho_h}{l_f}, \quad (6.8)$$

where w_b is the width of the band (length of lever arm extension to reach the filament), ρ_h is the motor density on the surface and l_f is the length of the filament which for the NC was determined to be $\sim 1 \mu\text{m}$. For the density of 1990 motors per $1 \mu\text{m}^2$ calculated for this surface, there are 52 arms acting on the filament, assuming only 1 arm can bind to the filament and that a myosin molecule can interact with a filament that is within 26 nm distance [259, 260, 270].

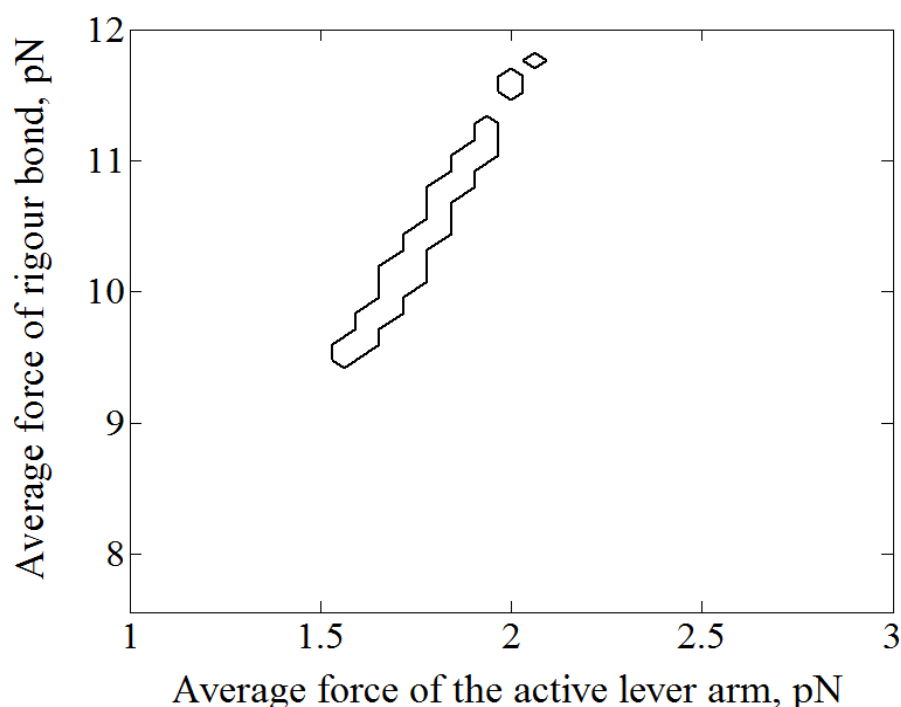


Figure 6.12. Simulated active and rigour forces of the motility on the NC surface that match the experimental values.

The resulting average forces that produce the velocities that are similar to the experimental values are shown in figure 6.12. Again the matching was done within 0.4 $\mu\text{m/s}$ region. The active forces, according to the simulation are in a good agreement with the experimental measurements performed using laser traps (table 6.5). The resistive force is slightly higher than the force produced solely by rigour bonds. This is believed to be caused by the orientation of the motors on the surface that “pushes” the filament in the direction, opposite to the original motion.

Table 6.5 A comparison of forces determined using via laser traps and the simulation aided with electrical motility experiments.

Average Active Force per Myosin Molecule	Average Resistive Force
3.6 pN (Determined with simulation)	10.6 pN (Determined with simulation)
3.4 pN	9.2 pN per Inactive Myosin
4.6 pN	14.8 pN per Inactive arm at high load

Alternatively the number of motors that interact with the filament for a known total number of motors on the surface can be calculated using a numerical simulation. Using sparse matrix in Matlab, the motors are randomly distributed on the simulated surface. By space partitioning data structure using k-dimensional space (k-d tree) the nearest neighbour search is performed to locate the motors that are within 26 nm distance away from the filament (figure 6.13).

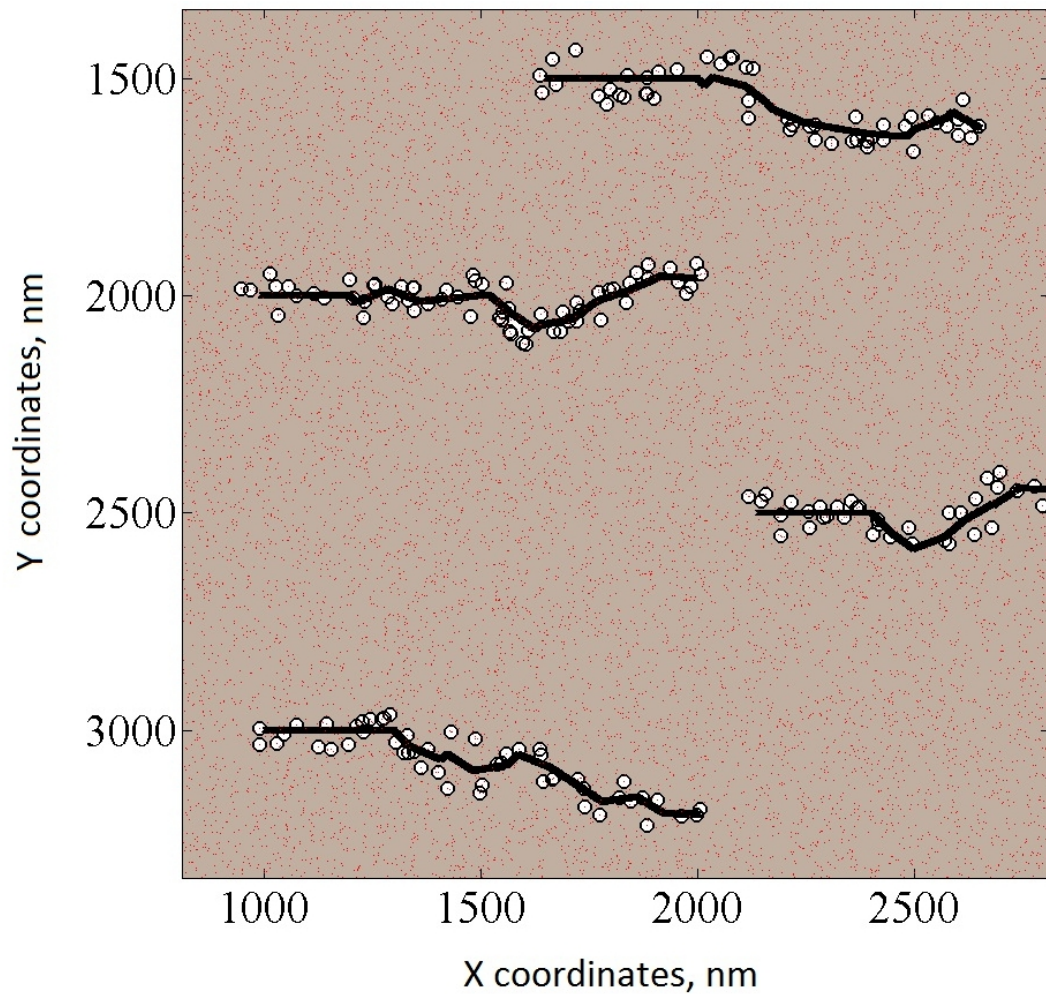


Figure 6.13. Simulated actin filament motility on the myosin (red dots) coated surface. The circles around the filaments represent the motors that are within the 26 nm proximity. For illustration purpose only selective motors that can interact with the filament are shown.

The average number of motors, interacting with the 1 μm filament using the simulation described was 63 myosin molecules for a density of 1990 motors per 1 μm^2 . This number is in a good agreement with 52 motors determined using the band model.

6.8 Conclusion

A novel technique has been presented to determine the number of active and inactive motors on the surface as well as the forces, generated by lever arms when interacting with the actin filament. This technique consists of an experimental procedure to determine the velocity and directionality of the filaments while subjected to external forces (i.e. electric field acting on negatively charged filament) and the numerical simulation that determines the necessary conditions for the observed motility. The simulation determined ratio of active and inactive motors for NC surface was in a good agreement with QCM and ATPase performed experiments. Both active and resistive forces also matched previously reported results.

Currently the measurements of the force of molecular motor require modification of the actin filaments, allowing for direct measurement of the force via fluorescence, or using optical tweezers. These modifications have the potential to alter the motility system under investigation and the methods, particularly those using optical tweezers, are inherently slow and require specialised equipment. The procedure described in this chapter is cheap, easy to setup and only requires a signal generator. Moreover it has the potential of miniaturisation which can be beneficial for lab-on-a-chip applications.

The numerical simulation that was used to interpret the experimental data is based on the assumption that the resistive force to the filament motion consists of the inactive (ATP insensitive) motors and active motors push the filament in the direction of motion. The actual orientation of motors on the surface, however is random. Thus the resistive force may be also caused by the motor, positioned in a way that the lever arm is pushing the filament in the direction, opposite to motion. The active force, presented in literature is often given as a statistical average. The variation of active force within the same experiment may also be explained by the random motor orientation on the surface. Another effect that needs investigating in order to develop a more realistic simulation of actin-myosin motility is the effect that the electric field has on the orientation of motors.

The experimentally determined filament sliding velocities on various surfaces were different. Using the numerical simulation, this difference was explained by the variation in the number of active and resistive motors on the surface. A number of factors is believed to have an quantitative and qualitative effect on the motor absorption to the surface. The qualitative effect is given by the number of arms that can interact with the filament after absorption to the surface. For a myosin II molecule, two, one or even no lever arms can interact with the filament depending on how the motor is positioned on the surface [271, 272]. The factors that affect the adsorption may be the hydrophobic/hydrophilic properties of the surface or different surface charges.

Moreover it is believed that the topography of surfaces used in the experiments may be different. As a result the filament travels extra distance to reach a motor that is located above or below its position affecting the velocity.

The novel approach of combining the numerical simulation with the experimental results using the electrical motility could be of great benefit when developing a cargo transport system within lab-on-a-chip device with molecular motors. Conventional methods in this case could not be used to determine parameters such as the number of motors or produced forces due to small scales of the device.

Chapter VII: Conclusion

Overview of main research findings and contributions are presented in this chapter

In this thesis various electrokinetic techniques were tested on objects with different mechanisms that describe its motion to further explore one of the main challenges that designing a practical microfluidic device has: designing a system that is capable of precise object manipulation and is small enough to be integrated into a practical device. The objects used in this work were the fluorescent spheres, bacteria and protein motors.

The motion of latex spheres described by the Brownian motion in the solution was investigated first. Using the castellated electrode geometry, the particles would migrate towards and away from the electrode edges as the dielectrophoretic force was switched on and off in a controlled manner. As a result, a number of concepts: amplitude modulated dielectrophoresis, oscillation bandwidth, normalised amplitude, cyclic steady state have been developed to characterise this motion. The image analysis tool has also been developed to quantitatively characterise the particle motion around the electrode edges.

The analysis has shown that particles of different size would respond differently to an amplitude modulated dielectrophoretic force. The experiments where the duty cycle was changed have demonstrated that as the modulating frequency increases, the maximum amplitude value progresses towards the higher duty cycle ratio. The developed AM-DEP system has already been successfully used in literature [142, 273] as a foundation to determining the parameters of objects, which is crucial when designing a simulation of the dielectrophoretic system.

The *Pseudomonas Fluorescence* bacteria, which has a more complicated motility mechanism was investigated next. It uses the flagella motor and its ability to rotate

and switch directions in response to environmental signals. It also has a sophisticated internal structure with ionic pump to introduce the nutrients and minimise the osmotic pressure on the cell wall.

The investigation of various electrokinetic techniques on the bacteria in the environment that supports the bacteria growth has been carried out. It was assumed that the difference in medium and bacteria conductivity and permittivity is insufficient to accommodate the dielectrophoretic force as the effect of DEP could not be observed over a range of frequencies and voltages. Non-motile (presumably dead) bacteria could, however, be trapped by pDEP force. This could be explained by the ion leakage after the death phase of the bacteria.

The effect of ACEO was also not observed for the frequency range that could be used with the setup. The frequency, at which the ACEO effect was previously reported, resulted in rapid bubble formation.

The negatively charged bacteria were successfully manipulated by the constant electric field with the needles and PDMS channel design and the fluid flow produced by the electrothermal flow. The developed setups however would either compromise the detection using fluorescent microscope (in the case of DC fields) or would result in fluid drying (ACET).

Using the computer aided simulation the experimental setup that produces the unidirectional fluid flow (ACET) was developed using the topographical PDMS channel design. Another simulation has shown that DC voltage of 0.01 V is sufficient to prevent the bacteria motion in a microfluidic channel. Both of these systems could be integrated into a practical microfluidic device.

The motility of protein motors used in the final study consists of the filament protein that slides over the motor cover surface and the motor protein that binds to the filament and pushes it, according to the resulting effect of the motor orientation and the Brownian motion.

The experimental setup was developed to investigate the effect of a constant electric field on the motility of the molecular motors. Five different surfaces were used for the experiment. The application of higher external electric field resulted in different velocity increase on different surfaces.

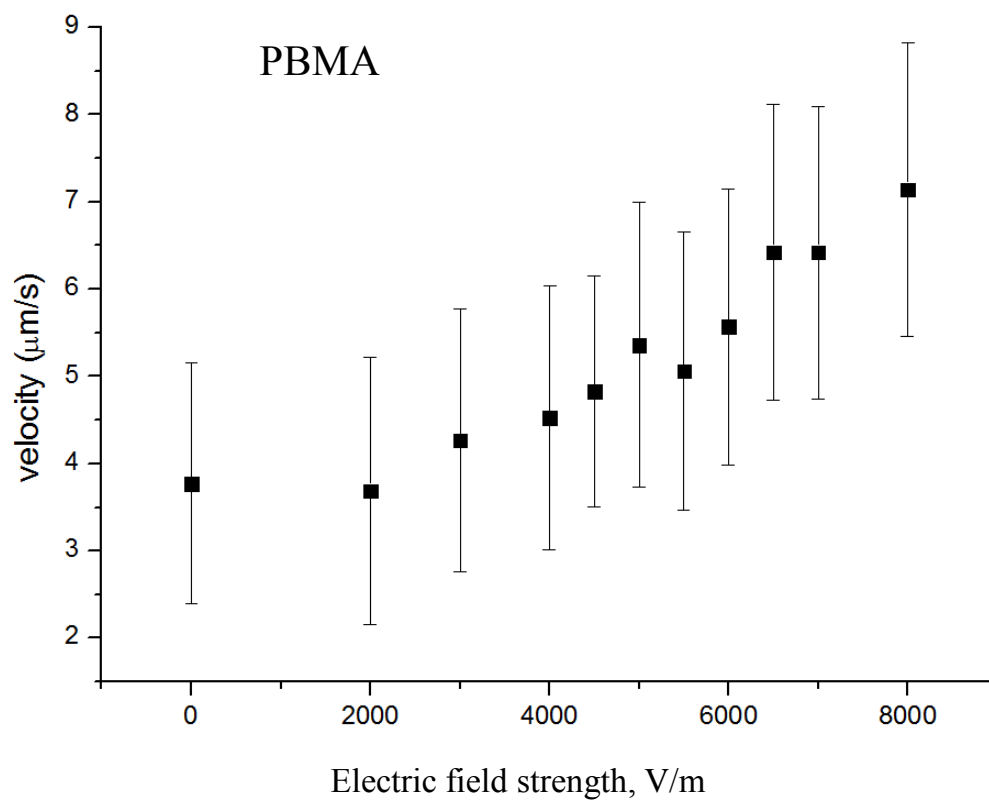
According to a developed simulation, the difference in the velocity increase is explained by the variation in the amount of active and resistive motors. It can be concluded that the highest velocity increase on the TMCS surface is explained by the fact that it has the least amount of motors interacting with the filament during the motility.

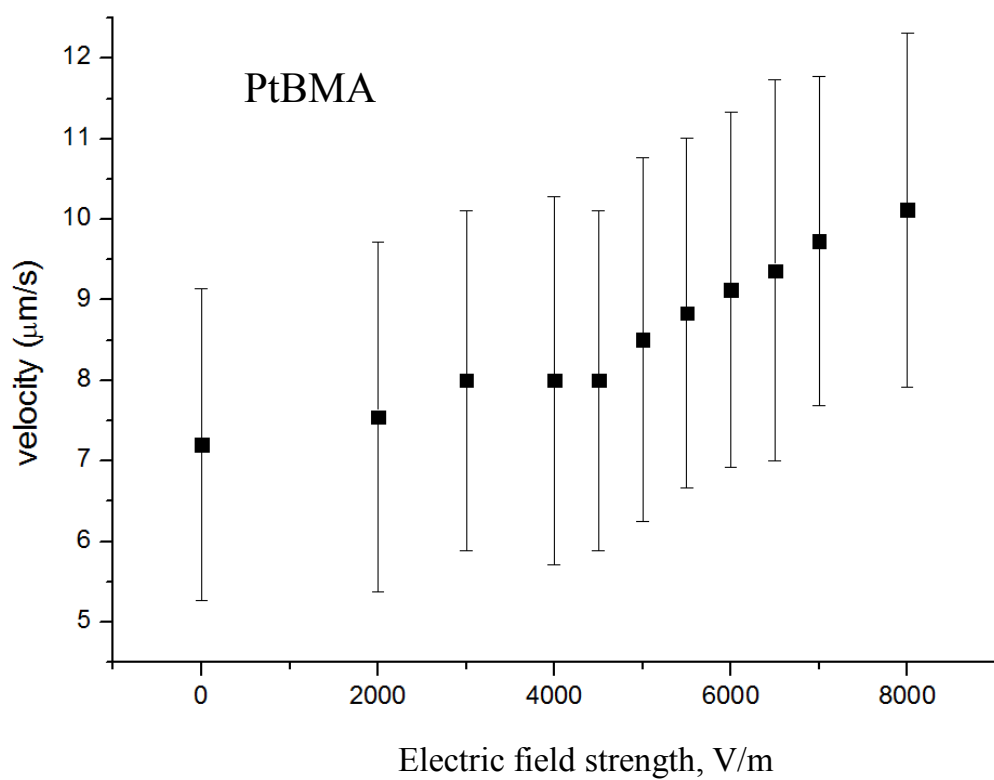
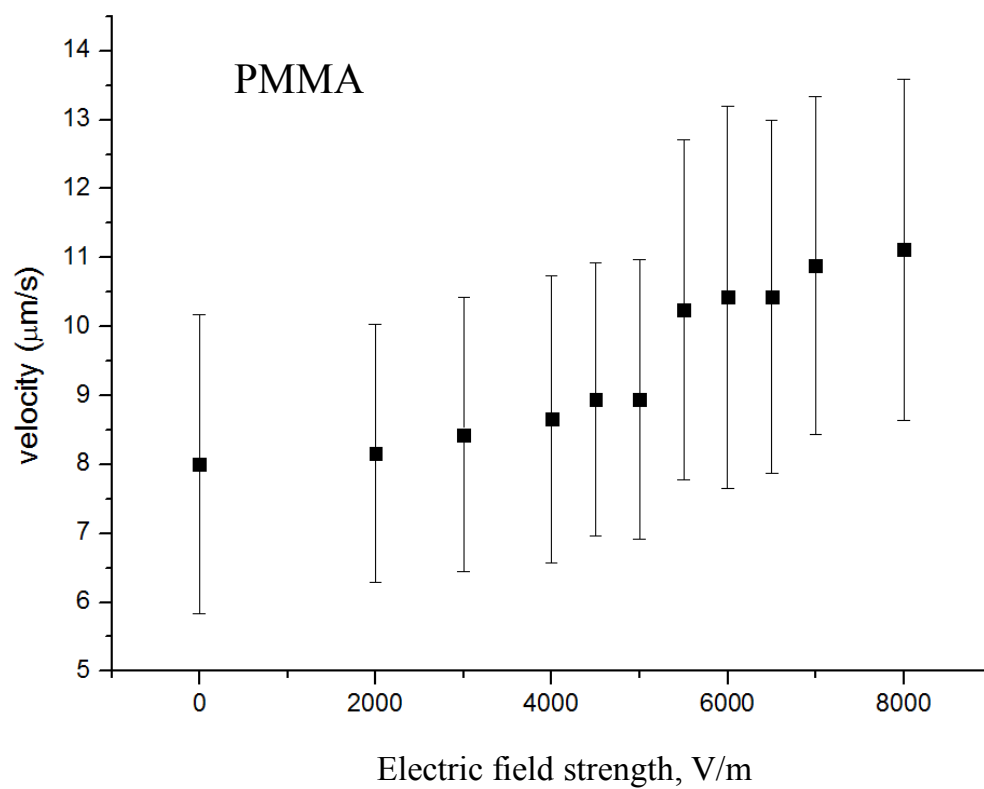
Using another simulation the fundamental parameters of the motility have been calculated: the determined values for active and resistive force were 3.6 pN and 10.6 pN respectively, which is in a good agreement with previously reported data.

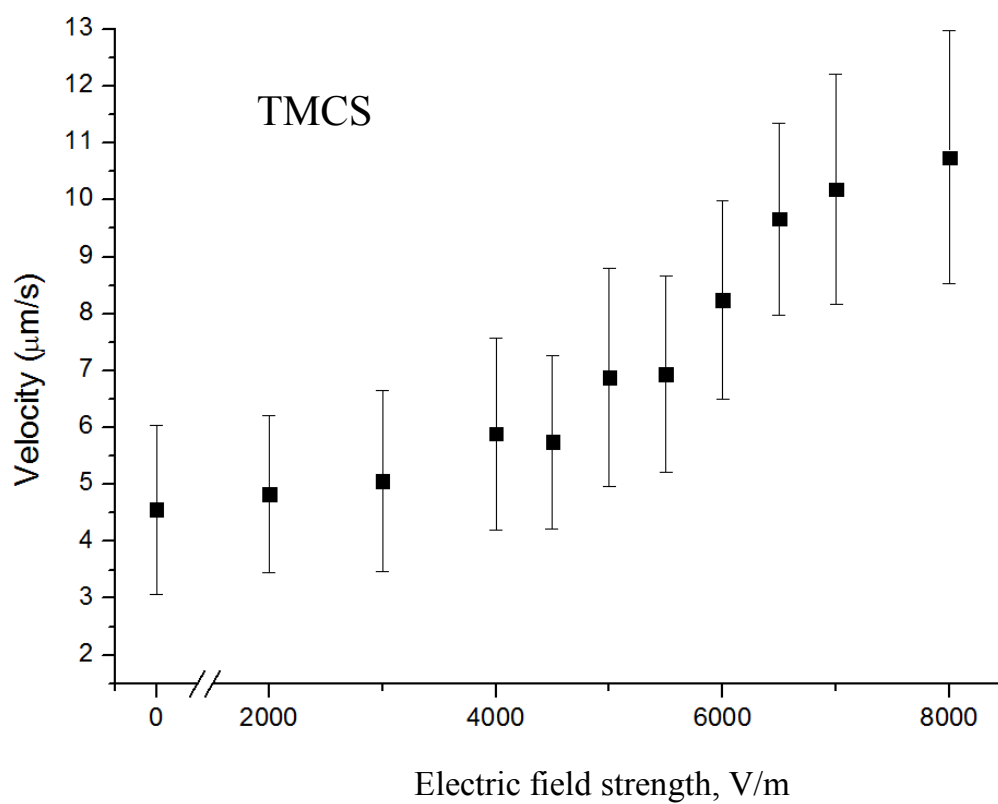
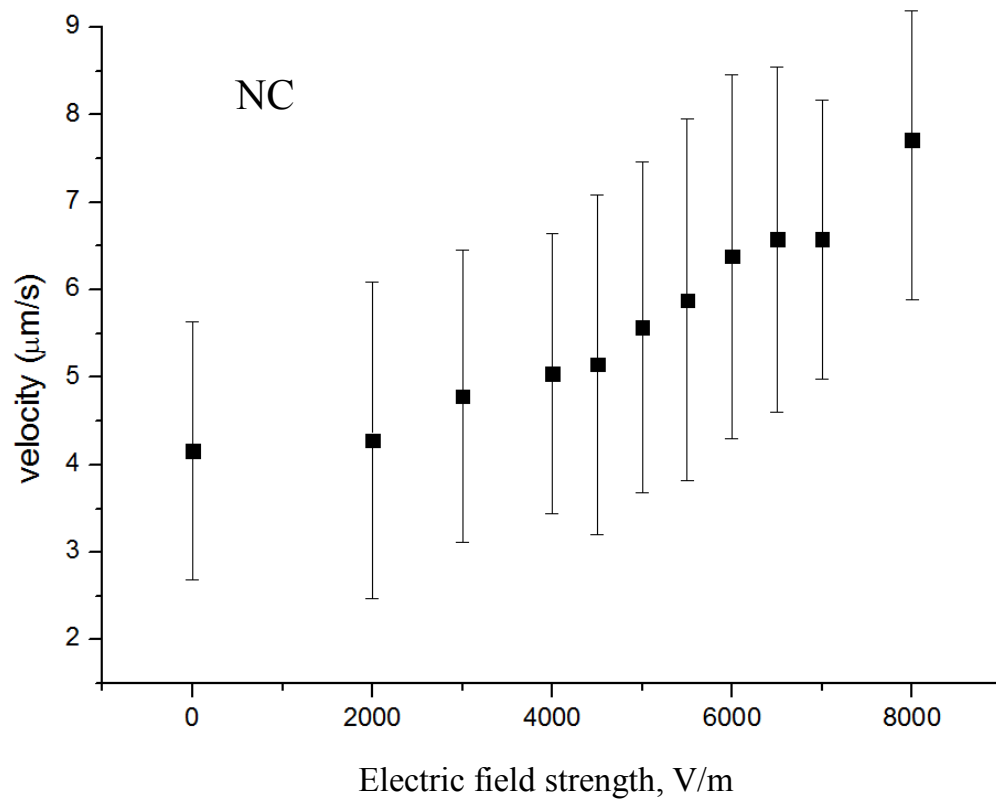
Finally, using the simulation in Matlab, the number of motors that can interact with the filament for a given motor distribution on the surface was calculated. For a motor density of 1990 motors per $1 \mu\text{m}^2$, 63 myosin molecules could interact with the $1 \mu\text{m}$ filament. This value is in a good agreement with the 52 motors, determined in the literature.

Appendix

The graphs of the velocity against the electric field on 5 surfaces are presented:







References

1. Singh, R., *Electronic Devices and Integrated Circuits*. 2009: Pearson Education Canada.
2. Riordan, M. and L. Hoddeson, *Crystal Fire: The Birth of the Information Age*. 1997: Norton.
3. Zimmerman, W.B.J. and S. International Centre for Mechanical, *Microfluidics: History, Theory and Applications*. 2006: Springer.
4. Gad-el-Hak, M., *MEMS: Introduction and Fundamentals*. 2010: Taylor & Francis.
5. Chin, C.D., V. Linder, and S.K. Sia, *Commercialization of microfluidic point-of-care diagnostic devices*. Lab Chip, 2012. **12**(12): p. 2118-2134.
6. Janasek, D., J. Franzke, and A. Manz, *Scaling and the design of miniaturized chemical-analysis systems*. Nature, 2006. **442**(7101): p. 374-380.
7. Hong, J.W. and S.R. Quake, *Integrated nanoliter systems*. Nat Biotech, 2003. **21**(10): p. 1179-1183.
8. Manz, A. and J.C.T. Eijkel, *Miniaturization and chip technology. What can we expect?* Pure and Applied Chemistry, 2001. **73**(10): p. 1555-1561.
9. Lion, N., et al., *Why the move to microfluidics for protein analysis?* Current Opinion in Biotechnology, 2004. **15**(1): p. 31-37.
10. Whitesides, G.M., *The origins and the future of microfluidics*. Nature, 2006. **442**(7101): p. 368-373.
11. Iverson, B.D. and S.V. Garimella, *Recent advances in microscale pumping technologies: a review and evaluation*. Microfluidics and Nanofluidics, 2008. **5**(2): p. 145-174.
12. Laser, D.J. and J.G. Santiago, *A review of micropumps*. Journal of Micromechanics and Microengineering, 2004. **14**(6): p. R35-R64.
13. Beebe, D.J., G.A. Mensing, and G.M. Walker, *Physics and applications of microfluidics in biology*. Annual Review of Biomedical Engineering, 2002. **4**: p. 261-286.
14. Fiorini, G.S. and D.T. Chiu, *Disposable microfluidic devices: fabrication, function, and application*. Biotechniques, 2005. **38**(3): p. 429-446.
15. Yamahata, C., et al., *Plastic micropump with ferrofluidic actuation*. Journal of Microelectromechanical Systems, 2005. **14**(1): p. 96-102.
16. Chung, K.H., et al., *Polymer microfluidic device replacing fluids using only capillary force*. Biomedical Applications of Micro- and Nanoengineering II, 2005. **5651**: p. 204-213.
17. Chung, K.H., et al., *Microfluidic chip accomplishing self-fluid replacement using only capillary force and its bioanalytical application*. Analytica Chimica Acta, 2007. **585**(1): p. 1-10.
18. Cubaud, T., et al., *Bubble dispenser in microfluidic devices*. Physical Review E, 2005. **72**(3).
19. Schwarz, M.A. and P.C. Hauser, *Recent developments in detection methods for microfabricated analytical devices*. Lab Chip, 2001. **1**(1): p. 1-6.
20. Baker, C.A., et al., *Recent advances in microfluidic detection systems*. Bioanalysis, 2009. **1**(5): p. 967-975.
21. Moon, S., et al., *Integrating microfluidics and lensless imaging for point-of-care testing*. Biosensors & Bioelectronics, 2009. **24**(11): p. 3208-3214.

22. Szczypinski, R., et al., *Fluorescence detection in microfluidics systems*. Przegląd Elektrotechniczny, 2012. **88**(10B): p. 88-91.
23. Dennis, P.J., et al., *Development of a Photothermal Absorbance Detector for Use with Microfluidic Devices*. Analytical Chemistry, 2010. **82**(10): p. 4063-4071.
24. Hiki, S., et al., *Highly sensitive detection of non-labeled peptides using UV excitation thermal lens microscope/liquid chromatography*. Bunseki Kagaku, 2007. **56**(1): p. 1-7.
25. Connatser, R.M., et al., *Analytical optimization of nanocomposite surface-enhanced Raman spectroscopy/scattering detection in microfluidic separation devices*. Electrophoresis, 2008. **29**(7): p. 1441-1450.
26. Farquharson, S. and P. Maksymiuk, *Simultaneous chemical separation and surface-enhanced Raman spectral detection using silver-doped sol-gels*. Applied Spectroscopy, 2003. **57**(4): p. 479-482.
27. Walker, P.A., et al., *Isotachophoretic separations on a microchip. Normal Raman spectroscopy detection*. Analytical Chemistry, 1998. **70**(18): p. 3766-3769.
28. Lacher, N.A., et al., *Microchip capillary electrophoresis/electrochemistry*. Electrophoresis, 2001. **22**(12): p. 2526-2536.
29. Wang, J., *Electrochemical detection for microscale analytical systems: a review*. Talanta, 2002. **56**(2): p. 223-231.
30. Lichtenberg, J., N.F. de Rooij, and E. Verpoorte, *A microchip electrophoresis system with integrated in-plane electrodes for contactless conductivity detection*. Electrophoresis, 2002. **23**(21): p. 3769-3780.
31. Pumera, M., et al., *Contactless conductivity detector for microchip capillary electrophoresis*. Analytical Chemistry, 2002. **74**(9): p. 1968-1971.
32. Urban, P.L., et al., *High-density micro-arrays for mass spectrometry*. Lab Chip, 2010. **10**(23): p. 3206-3209.
33. Nilsson, J., et al., *Review of cell and particle trapping in microfluidic systems*. Analytica Chimica Acta, 2009. **649**(2): p. 141-157.
34. Velez, O.D. and K.H. Bhatt, *On-chip micromanipulation and assembly of colloidal particles by electric fields*. Soft Matter, 2006. **2**(9): p. 738-750.
35. Morgan, H. and N.G. Green, *AC electrokinetics : colloids and nanoparticles*. 2003, Philadelphia, PA: Research Studies Press.
36. Shim, J.U., et al., *Using microfluidics to decouple nucleation and growth of protein crystals*. Crystal Growth & Design, 2007. **7**(11): p. 2192-2194.
37. Zheng, B., et al., *A droplet-based, composite PDMS/glass capillary microfluidic system for evaluating protein crystallization conditions by microbatch and vapor-diffusion methods with on-chip X-ray diffraction*. Angewandte Chemie-International Edition, 2004. **43**(19): p. 2508-2511.
38. Hansen, C.L., et al., *A robust and scalable microfluidic metering method that allows protein crystal growth by free interface diffusion*. Proceedings of the National Academy of Sciences of the United States of America, 2002. **99**(26): p. 16531-16536.
39. Martinez, A.W., et al., *Diagnostics for the Developing World: Microfluidic Paper-Based Analytical Devices*. Analytical Chemistry, 2010. **82**(1): p. 3-10.
40. Mao, X.L. and T.J. Huang, *Microfluidic diagnostics for the developing world*. Lab Chip, 2012. **12**(8): p. 1412-1416.
41. Yager, P., et al., *Microfluidic diagnostic technologies for global public health*. Nature, 2006. **442**(7101): p. 412-418.

42. Reboud, J., et al., *Shaping acoustic fields as a toolset for microfluidic manipulations in diagnostic technologies*. Proceedings of the National Academy of Sciences of the United States of America, 2012. **109**(38): p. 15162-15167.
43. Chin, C.D., et al., *Microfluidics-based diagnostics of infectious diseases in the developing world*. Nature Medicine, 2011. **17**(8): p. 1015-U138.
44. Takayama, S., et al., *Selective chemical treatment of cellular microdomains using multiple laminar streams*. Chemistry & Biology, 2003. **10**(2): p. 123-130.
45. Terenna, C.R., et al., *Physical Mechanisms Redirecting Cell Polarity and Cell Shape in Fission Yeast*. Current Biology, 2008. **18**(22): p. 1748-1753.
46. Hargis, A.D., J.P. Alarie, and J.M. Ramsey, *Characterization of cell lysis events on a microfluidic device for high-throughput single cell analysis*. Electrophoresis, 2011. **32**(22): p. 3172-3179.
47. Mellors, J.S., et al., *Integrated Microfluidic Device for Automated Single Cell Analysis Using Electrophoretic Separation and Electrospray Ionization Mass Spectrometry*. Analytical Chemistry, 2010. **82**(3): p. 967-973.
48. Wheeler, A.R., et al., *Microfluidic device for single-cell analysis*. Analytical Chemistry, 2003. **75**(14): p. 3581-3586.
49. McClain, M.A., et al., *Microfluidic devices for the high-throughput chemical analysis of cells*. Analytical Chemistry, 2003. **75**(21): p. 5646-5655.
50. Cho, B.S., et al., *Passively driven integrated microfluidic system for separation of motile sperm*. Analytical Chemistry, 2003. **75**(7): p. 1671-1675.
51. Kim, J., et al., *A microfluidic device for high throughput bacterial biofilm studies*. Lab Chip, 2012. **12**(6): p. 1157-1163.
52. Kim, J., H.D. Park, and S. Chung, *Microfluidic Approaches to Bacterial Biofilm Formation*. Molecules, 2012. **17**(8): p. 9818-9834.
53. Groisman, A., et al., *A microfluidic chemostat for experiments with bacterial and yeast cells*. Nature Methods, 2005. **2**(9): p. 685-689.
54. Balagadde, F.K., et al., *Long-term monitoring of bacteria undergoing programmed population control in a microchemostat*. Science, 2005. **309**(5731): p. 137-140.
55. Burton, E.A., et al., *Molecular Gradients of Bioinertness Reveal a Mechanistic Difference between Mammalian Cell Adhesion and Bacterial Biofilm Formation*. Langmuir, 2009. **25**(3): p. 1547-1553.
56. Wessel, A.K., et al., *Going local: technologies for exploring bacterial microenvironments*. Nat Rev Micro, 2013. **11**(5): p. 337-348.
57. Wu, Z.G., et al., *Soft inertial microfluidics for high throughput separation of bacteria from human blood cells*. Lab Chip, 2009. **9**(9): p. 1193-1199.
58. Moon, H.S., et al. *Continuous microfluidic airborne bacteria separation using dielectrophoresis*. in *Solid-State Sensors, Actuators and Microsystems Conference, 2009. TRANSDUCERS 2009. International*. 2009.
59. Xia, N., et al., *Combined microfluidic-micromagnetic separation of living cells in continuous flow*. Biomedical Microdevices, 2006. **8**(4): p. 299-308.
60. Khoshmanesh, K., et al., *On-chip separation of Lactobacillus bacteria from yeasts using dielectrophoresis*. Microfluidics and Nanofluidics, 2012. **12**(1-4): p. 597-606.
61. Oblath, E.A., et al., *A microfluidic chip integrating DNA extraction and real-time PCR for the detection of bacteria in saliva*. Lab Chip, 2013. **13**(7): p. 1325-1332.
62. Jha, A.K., A. Tripathi, and A. Bose, *A microfluidic device for bacteria detection in aqueous samples*. Environmental Technology, 2011. **32**(14): p. 1661-1667.
63. Li, Y.X., et al., *Microfluidic Chip Electrophoresis with Laser-Induced Fluorescence Detection for Rapid Analysis of Four Foodborne Pathogenic Bacteria*. Chinese Journal of Analytical Chemistry, 2008. **36**(12): p. 1667-1671.

64. Yu, J.J., L.D. Xiao, and M. Yang, *A PDMS microfluidic chip with nanostructures for bacteria concentration and fast detection*. Mems 2008: 21st IEEE International Conference on Micro Electro Mechanical Systems, Technical Digest, 2008: p. 272-275.
65. Boehm, D.A., P. Gottlieb, and S.Z. Hua, *Surface functionalization of a microfluidic biosensor for bacteria detection and identification*. Sensors and Smart Structures Technologies for Civil, Mechanical, and Aerospace Systems 2007, Pts 1 and 2, 2007. **6529**: p. U180-U187.
66. Ikeda, M., et al., *Rapid and simple detection of food poisoning bacteria by bead assay with a microfluidic chip-based system*. Journal of Microbiological Methods, 2006. **67**(2): p. 241-247.
67. Xi, C.W., S. Boppart, and L. Raskin, *Use of molecular beacons for the detection of bacteria in microfluidic devices*. Microfluidics, Biomems, and Medical Microsystems, 2003. **4982**: p. 170-177.
68. Mukhopadhyay, R., *Molecular motors - Meet microfluidic systems*. Analytical Chemistry, 2005. **77**(13): p. 249a-252a.
69. Korten, T., A. Mansson, and S. Diez, *Towards the application of cytoskeletal motor proteins in molecular detection and diagnostic devices*. Current Opinion in Biotechnology, 2010. **21**(4): p. 477-488.
70. Montemagno, C. and G. Bachand, *Constructing nanomechanical devices powered by biomolecular motors*. Nanotechnology, 1999. **10**(3): p. 225-231.
71. Bakewell, D.J.G. and D.V. Nicolau, *Protein linear molecular motor-powered nanodevices*. Australian Journal of Chemistry, 2007. **60**(5): p. 314-332.
72. Spetzler, D., et al., *Recent developments of bio-molecular motors as on-chip devices using single molecule techniques*. Lab Chip, 2007. **7**(12): p. 1633-1643.
73. Korten, S., et al., *Sample solution constraints on motor-driven diagnostic nanodevices*. Lab Chip, 2013. **13**(5): p. 866-876.
74. Russel, W.B., D.A. Saville, and W.R. Schowalter, *Colloidal dispersions*. Cambridge monographs on mechanics and applied mathematics. 1989, Cambridge ; New York: Cambridge University Press. xvii, 525 p., 1 leaf of plates.
75. Lyklema, J., *Fundamentals of interface and colloid science*. 2000, San Diego: Academic Press. v. <3>.
76. Delgado, A.n.V., *Interfacial electrokinetics and electrophoresis*. Surfactant science series. 2002, New York: Marcel Dekker, Inc. xii, 991 p.
77. Reuss, F.F., *Mem. Soc. Imperiale Naturalistes Moscow* 2. 1809: p. 327.
78. Smoluchowski, M., *Contribution a la theorie de l'endosmose electrique et de quelques phenomenes correlatifs*. Bulletin International de l'Academie des Sciences de Cracovie, 1903. **8**: p. 182.
79. Sarkar, P. and P.S. Nicholson, *Electrophoretic deposition (EPD): Mechanisms, kinetics, and application to ceramics*. Journal of the American Ceramic Society, 1996. **79**(8): p. 1987-2002.
80. Hanaor, D., et al., *The effects of carboxylic acids on the aqueous dispersion and electrophoretic deposition of ZrO₂*. Journal of the European Ceramic Society, 2012. **32**(1): p. 235-244.
81. Pohl, H.A., *Dielectrophoresis : the behavior of neutral matter in nonuniform electric fields*. Cambridge monographs on physics. 1978, Cambridge ; New York: Cambridge University Press. xii, 579 p.
82. Pohl, H.A., *The Motion and Precipitation of Suspensoids in Divergent Electric Fields*. Journal of Applied Physics, 1951. **22**(7): p. 869-871.

83. Pethig, R., *Review Article-Dielectrophoresis: Status of the theory, technology, and applications*. Biomicrofluidics, 2010. **4**(2).
84. Green, N.G., A. Ramos, and H. Morgan, *Numerical solution of the dielectrophoretic and travelling wave forces for interdigitated electrode arrays using the finite element method*. Journal of Electrostatics, 2002. **56**(2): p. 235-254.
85. Morgan, H., et al., *The dielectrophoretic and travelling wave forces generated by interdigitated electrode arrays: analytical solution using Fourier series*. Journal of Physics D-Applied Physics, 2001. **34**(10): p. 1553-1561.
86. Song, H.J. and D.J. Bennett, *A semi-analytical approach using artificial neural network for dielectrophoresis generated by parallel electrodes*. Journal of Electrostatics, 2010. **68**(1): p. 49-56.
87. Sun, T., H. Morgan, and N.G. Green, *Analytical Solutions of the Dielectrophoretic and Travelling Wave Forces Generated by Interdigitated Electrode Arrays*. Electrostatics 2007, 2009. **142**.
88. Wang, X.J., et al., *A theoretical method of electrical field analysis for dielectrophoretic electrode arrays using Green's theorem*. Journal of Physics D-Applied Physics, 1996. **29**(6): p. 1649-1660.
89. Hoettges, K.F., et al., *Optimizing particle collection for enhanced surface-based biosensors*. Ieee Engineering in Medicine and Biology Magazine, 2003. **22**(6): p. 68-74.
90. Voldman, J., et al., *A microfabrication-based dynamic array cytometer*. Analytical Chemistry, 2002. **74**(16): p. 3984-3990.
91. Hughes, M.P., M.P. Hughes, and K.F. Hoettges, *Microengineering in biotechnology*. 2010: Humana Press.
92. Martinez-Duarte, R., et al., *The integration of 3D carbon-electrode dielectrophoresis on a CD-like centrifugal microfluidic platform*. Lab Chip, 2010. **10**(8): p. 1030-1043.
93. Fiedler, S., et al., *Dielectrophoretic sorting of particles and cells in a microsystem*. Analytical Chemistry, 1998. **70**(9): p. 1909-1915.
94. Thomas, R.S., H. Morgan, and N.G. Green, *Negative DEP traps for single cell immobilisation*. Lab Chip, 2009. **9**(11): p. 1534-1540.
95. Braff, W.A., A. Pignier, and C.R. Buie, *High sensitivity three-dimensional insulator-based dielectrophoresis*. Lab Chip, 2012. **12**(7): p. 1327-1331.
96. Lapidco-Encinas, B.H., et al., *Insulator-based dielectrophoresis for the selective concentration and separation of live bacteria in water*. Electrophoresis, 2004. **25**(10-11): p. 1695-1704.
97. Shafiee, H., et al., *Contactless dielectrophoresis: a new technique for cell manipulation*. Biomedical Microdevices, 2009. **11**(5): p. 997-1006.
98. Pethig, R. and G.H. Markx, *Applications of dielectrophoresis in biotechnology*. Trends in Biotechnology, 1997. **15**(10): p. 426-432.
99. Jones, T.B., *Electromechanics of particles*. 1995, Cambridge ; New York: Cambridge University Press. xxii, 265 p.
100. Hughes, M.P., *Nanoelectromechanics in engineering and biology*. Nano- and microscience, engineering, technology, and medicine series. 2003, Boca Raton: CRC Press. 322 p.
101. Castellarnau, M., et al., *Dielectrophoresis as a tool to characterize and differentiate isogenic mutants of Escherichia coli*. Biophysical Journal, 2006. **91**(10): p. 3937-3945.
102. Hawkins, B.G., et al., *Automated Dielectrophoretic Characterization of Mycobacterium smegmatis*. Analytical Chemistry, 2011. **83**(9): p. 3507-3515.

103. Marx, G.H., et al., *Dielectrophoretic Characterization and Separation of Microorganisms*. Microbiology-Uk, 1994. **140**: p. 585-591.
104. Yunus, Z., et al., *A simple method for the measurement of bacterial particle conductivities*. Journal of Microbiological Methods, 2002. **51**(3): p. 401-406.
105. Zhu, K., et al., *Separation by dielectrophoresis of dormant and nondormant bacterial cells of Mycobacterium smegmatis*. Vol. 4. 2010.
106. Jen, C.-P. and T.-W. Chen, *Selective trapping of live and dead mammalian cells using insulator-based dielectrophoresis within open-top microstructures*. Biomedical Microdevices, 2009. **11**(3): p. 597-607.
107. Lapizco-Encinas, B.H., et al., *Dielectrophoretic Concentration and Separation of Live and Dead Bacteria in an Array of Insulators*. Analytical Chemistry, 2004. **76**(6): p. 1571-1579.
108. Patel, S., et al., *Microfluidic separation of live and dead yeast cells using reservoir-based dielectrophoresis*. Biomicrofluidics, 2012. **6**(3): p. 34102.
109. Jen, C.-P. and W.-F. Chen, *An insulator-based dielectrophoretic microdevice for the simultaneous filtration and focusing of biological cells*. Biomicrofluidics, 2011. **5**(4): p. -.
110. Helmholtz, H., *Studien über electrische Grenzschichten*. Annalen der Physik, 1879. **243**(7): p. 337-382.
111. Gouy, *On the constitution of the electric charge at the surface of an electrolyte*. Comptes Rendus Hebdomadaires Des Seances De L Academie Des Sciences, 1909. **149**: p. 654-657.
112. Chapman, D.L., *A Contribution to the Theory of Electrocapillarity*. Philosophical Magazine, 1913. **25**(148): p. 475-481.
113. Stern, O., *The theory of the electrolytic double shift*. Zeitschrift Fur Elektrochemie Und Angewandte Physikalische Chemie, 1924. **30**: p. 508-516.
114. Ramos, A., et al., *Ac electrokinetics: a review of forces in microelectrode structures*. Journal of Physics D-Applied Physics, 1998. **31**(18): p. 2338-2353.
115. Ramos, A., et al., *AC electric-field-induced fluid flow in microelectrodes*. Journal of Colloid and Interface Science, 1999. **217**(2): p. 420-422.
116. Gonzalez, A., et al., *Fluid flow induced by nonuniform ac electric fields in electrolytes on microelectrodes. II. A linear double-layer analysis*. Physical Review E, 2000. **61**(4): p. 4019-4028.
117. Green, N.G., et al., *Fluid flow induced by nonuniform ac electric fields in electrolytes on microelectrodes. I. Experimental measurements*. Physical Review E, 2000. **61**(4): p. 4011-4018.
118. Green, N.G., A. Ramos, and H. Morgan, *Ac electrokinetics: a survey of sub-micrometre particle dynamics*. Journal of Physics D-Applied Physics, 2000. **33**(6): p. 632-641.
119. Muller, T., et al., *Trapping of micrometre and sub-micrometre particles by high-frequency electric fields and hydrodynamic forces*. Journal of Physics D-Applied Physics, 1996. **29**(2): p. 340-349.
120. Green, N.G., et al., *Electrothermally induced fluid flow on microelectrodes*. Journal of Electrostatics, 2001. **53**(2): p. 71-87.
121. Fuhr, G., T. Schnelle, and B. Wagner, *Traveling Wave-Driven Microfabricated Electrohydrodynamic Pumps for Liquids*. Journal of Micromechanics and Microengineering, 1994. **4**(4): p. 217-226.
122. Du, E. and S. Manoochehri, *Enhanced ac electrothermal fluidic pumping in microgrooved channels*. Journal of Applied Physics, 2008. **104**(6).

123. Stubbe, M. and J. Gimsa, *A short review on AC electro-thermal micropumps based on smeared structural polarizations in the presence of a temperature gradient*. Colloids and Surfaces a-Physicochemical and Engineering Aspects, 2011. **376**(1-3): p. 97-101.
124. Wu, J., M. Lian, and K. Yang, *Micropumping of biofluids by alternating current electrothermal effects*. Applied Physics Letters, 2007. **90**(23).
125. Sasaki, N., T. Kitamori, and H.B. Kim, *Fluid mixing using AC electrothermal flow on meandering electrodes in a microchannel*. Electrophoresis, 2012. **33**(17): p. 2668-2673.
126. Ng, W.Y., et al., *DC-biased AC-electroosmotic and AC-electrothermal flow mixing in microchannels*. Lab Chip, 2009. **9**(6): p. 802-809.
127. Loire, S., et al., *A theoretical and experimental study of ac electrothermal flows*. Journal of Physics D-Applied Physics, 2012. **45**(18).
128. Fleisch, D.A., *A student's guide to Maxwell's equations*. 2008, Cambridge, UK ; New York: Cambridge University Press. ix, 134 p.
129. Lide, D.R., *CRC handbook of chemistry and physics : a ready reference book of chemical and physical data*. 1993, CRC Press.
130. Chen, D.F. and H. Du, *Simulation studies on electrothermal fluid flow induced in a dielectrophoretic microelectrode system*. Journal of Micromechanics and Microengineering, 2006. **16**(11): p. 2411-2419.
131. Pham, D., et al., *Effects of polymer properties on laser ablation behaviour*. Smart Materials & Structures, 2002. **11**(5): p. 668-674.
132. Pethig, R., et al., *Development of biofactory-on-a-chip technology using excimer laser micromachining*. Journal of Micromechanics and Microengineering, 1998. **8**(2): p. 57-63.
133. Schnelle, T., et al., *Dielectrophoretic manipulation of suspended submicron particles*. Electrophoresis, 2000. **21**(1): p. 66-73.
134. Franssila, S., *Introduction to microfabrication*. 2nd ed. 2010, Chichester, West Sussex England: John Wiley & Sons. xiv, 518 p.
135. Folch, A. and M. Toner, *Cellular micropatterns on biocompatible materials*. Biotechnology Progress, 1998. **14**(3): p. 388-392.
136. Bakewell, D.J. and H. Morgan, *Dielectrophoresis of DNA: Time- and frequency-dependent collections on microelectrodes (vol 5, pg 1, 2006)*. Ieee Transactions on Nanobioscience, 2006. **5**(2): p. 139-146.
137. Carlson, A.B., P.B. Crilly, and J.C. Rutledge, *Communication systems : an introduction to signals and noise in electrical communication*. 2002, Boston: McGraw-Hill.
138. Bakewell, D.J. and A. Chichenkov, *Quantifying dielectrophoretic nanoparticle response to amplitude modulated input signal (vol 45, 365402, 2012)*. Journal of Physics D-Applied Physics, 2012. **45**(49).
139. Papoulis, A., *Probability, random variables, and stochastic processes*. 2nd ed. McGraw-Hill series in electrical engineering Communications and information theory. 1984, New York: McGraw-Hill. xv, 576 p.
140. Gardiner, C.W., *Handbook of stochastic methods for physics, chemistry, and the natural sciences*. 2nd ed. Springer series in synergetics 13. 1985, Berlin ; New York: Springer-Verlag. xix, 442 p.
141. Bakewell, D.J. and H. Morgan, *Quantifying dielectrophoretic collections of sub-micron particles on microelectrodes*. Measurement Science & Technology, 2004. **15**(1): p. 254-266.

142. Bakewell, D.J. and D. Holmes, *Dual-cycle dielectrophoretic collection rates for probing the dielectric properties of nanoparticles*. Electrophoresis, 2013: p. n/a-n/a.
143. Freeman-Cook, L. and K.D. Freeman-Cook, *Staphylococcus aureus infections*. Deadly diseases and epidemics. 2006, Philadelphia: Chelsea House Publishers. 182 p.
144. Gram, H.C., *The differential staining of Schizomycetes in tissue sections and in dried preparations*. Fortschritte der Medizin, 1884. **2**: p. 185-89.
145. Prescott, L.M., J.P. Harley, and D.A. Klein, *Microbiology*. 3rd ed. 1996, Dubuque, IA: Wm. C. Brown Publishers. xxxii, 935, 93 p.
146. Madigan, M.T., M.T. Madigan, and T.D. Brock, *Brock biology of microorganisms*. 12th ed. 2009, San Francisco, CA: Pearson/Benjamin Cummings. xxviii, 1061 p.
147. Whitesides, G.M., et al., *Soft lithography in biology and biochemistry*. Annual Review of Biomedical Engineering, 2001. **3**: p. 335-373.
148. DiLuzio, W.R., et al., *Escherichia coli swim on the right-hand side*. Nature, 2005. **435**(7046): p. 1271-1274.
149. Meel, C., et al., *Three-Dimensional Obstacles for Bacterial Surface Motility*. Small, 2012. **8**(4): p. 530-534.
150. Binz, M., et al., *Motility of bacteria in microfluidic structures*. Microelectronic Engineering, 2010. **87**(5-8): p. 810-813.
151. Kojima, M., et al. *Evaluation of bacteria behavior in micro-channel for bacteria driven liposome*. in *Micro-NanoMechatronics and Human Science (MHS), 2011 International Symposium on*. 2011.
152. Nicolau, D.V., et al., *Molecular motors-based micro- and nano-biocomputation devices*. Microelectronic Engineering, 2006. **83**(4-9): p. 1582-1588.
153. Hanson, K.L., et al., *Fungi use efficient algorithms for the exploration of microfluidic networks*. Small, 2006. **2**(10): p. 1212-1220.
154. van Zalinge, H. and D.V. Nicolau, *From personal communication*.
155. Kremmydas, G.F., A.P. Tampakaki, and D.G. Georgakopoulos, *Characterization of the Biocontrol Activity of Pseudomonas fluorescens Strain X Reveals Novel Genes Regulated by Glucose*. Plos One, 2013. **8**(4).
156. de Bruijn, I. and J.M. Raaijmakers, *Regulation of Cyclic Lipopeptide Biosynthesis in Pseudomonas fluorescens by the ClpP Protease*. Journal of Bacteriology, 2009. **191**(6): p. 1910-1923.
157. Schrott, W., et al., *Study on surface properties of PDMS microfluidic chips treated with albumin*. Biomicrofluidics, 2009. **3**(4).
158. Pelesko, J.A. and D.H. Bernstein, *Modeling MEMS and NEMS*. 2002: Taylor & Francis.
159. Harris, J.O. and R.M. Kline, *Electrophoresis of Motile Bacteria*. Journal of Bacteriology, 1956. **72**(4): p. 530-532.
160. Cheng, I.F., et al., *An integrated dielectrophoretic chip for continuous bioparticle filtering, focusing, sorting, trapping, and detecting*. Biomicrofluidics, 2007. **1**(2).
161. Cheng, I.F., et al., *A continuous high-throughput bioparticle sorter based on 3D traveling-wave dielectrophoresis*. Lab Chip, 2009. **9**(22): p. 3193-3201.
162. Park, S. and A. Beskok, *Alternating current electrokinetic motion of colloidal particles on interdigitated microelectrodes*. Analytical Chemistry, 2008. **80**(8): p. 2832-2841.
163. Asencor, F.J., et al., *Comparison between the Behavior of Yeast and Bacteria in a Nonuniform Alternating Electric-Field*. Bioelectrochemistry and Bioenergetics, 1990. **24**(2): p. 203-214.
164. Inoue, T., et al., *Dielectrophoretic Behavior of Micrococcus-Lysodeikticus and Its Protoplast*. Journal of Electrostatics, 1988. **21**(2-3): p. 215-223.

165. Markx, G.H., P.A. Dyda, and R. Pethig, *Dielectrophoretic separation of bacteria using a conductivity gradient*. Journal of Biotechnology, 1996. **51**(2): p. 175-180.
166. Kijlstra, J. and A. Vanderwal, *Electrokinetic Behavior of Bacterial Suspensions*. Bioelectrochemistry and Bioenergetics, 1995. **37**(2): p. 149-151.
167. Suehiro, J., et al., *Selective detection of specific bacteria using dielectrophoretic impedance measurement method combined with an antigen-antibody reaction*. Journal of Electrostatics, 2003. **58**(3-4): p. 229-246.
168. Bessette, P.H., et al., *Microfluidic library screening for mapping antibody epitopes*. Analytical Chemistry, 2007. **79**(5): p. 2174-2178.
169. Li, H.B. and R. Bashir, *Dielectrophoretic separation and manipulation of live and heat-treated cells of Listeria on microfabricated devices with interdigitated electrodes*. Sensors and Actuators B-Chemical, 2002. **86**(2-3): p. 215-221.
170. Johansson, L.E., et al., *Determination of conductivity of bacteria by using cross-flow filtration*. Biotechnology Letters, 2006. **28**(8): p. 601-603.
171. Morbach, S. and R. Kramer, *Body shaping under water stress: Osmosensing and osmoregulation of solute transport in bacteria*. Chembiochem, 2002. **3**(5): p. 385-397.
172. Green, N.G., et al., *Fluid flow induced by nonuniform ac electric fields in electrolytes on microelectrodes. III. Observation of streamlines and numerical simulation*. Physical Review E, 2002. **66**(2).
173. Du, E. and S. Manoochehri, *Microfluidic pumping optimization in microgrooved channels with ac electrothermal actuations*. Applied Physics Letters, 2010. **96**(3).
174. Hackney, D.D., *The kinetic cycles of myosin, kinesin, and dynein*. Annual Review of Physiology, 1996. **58**: p. 731-750.
175. Fulga, F., D.V. Nicolau, and D.V. Nicolau, *Models of protein linear molecular motors for dynamic nanodevices*. Integrative Biology, 2009. **1**(2): p. 150-169.
176. Block, S.M., L.S.B. Goldstein, and B.J. Schnapp, *Bead Movement by Single Kinesin Molecules Studied with Optical Tweezers*. Nature, 1990. **348**(6299): p. 348-352.
177. Uyeda, T.Q.P., et al., *Quantized velocities at low myosin densities in an in vitro motility*. Nature, 1991. **352**(6333): p. 307-311.
178. Svoboda, K., et al., *Direct Observation of Kinesin Stepping by Optical Trapping Interferometry*. Nature, 1993. **365**(6448): p. 721-727.
179. Svoboda, K. and S.M. Block, *Force and Velocity Measured for Single Kinesin Molecules*. Cell, 1994. **77**(5): p. 773-784.
180. Finer, J.T., R.M. Simmons, and J.A. Spudich, *Single Myosin Molecule Mechanics - Piconewton Forces and Nanometer Steps*. Nature, 1994. **368**(6467): p. 113-119.
181. Spudich, J.A. and A. Mehta, *Single myosin molecule mechanics: Nanometer steps, piconewton forces, millisecond kinetics, and stiffness of elastic elements measured with a dual-beam laser trap*. FASEB Journal, 1997. **11**(9): p. A855-A855.
182. Ishijima, A., et al., *Multiple- and single-molecule analysis of the actomyosin motor by nanometer piconewton manipulation with a microneedle: Unitary steps and forces*. Biophysical Journal, 1996. **70**(1): p. 383-400.
183. Vale, R.D., et al., *Direct observation of single kinesin molecules moving along microtubules*. Nature, 1996. **380**(6573): p. 451-453.
184. Yanagida, T., et al., *Single molecule analysis of the actomyosin motor*. Current Opinion in Cell Biology, 2000. **12**(1): p. 20-25.
185. Schliwa, M. and G. Woehlke, *Molecular motors*. Nature, 2003. **422**(6933): p. 759-765.
186. Molloy, J.E. and S. Schmitz, *Molecular motors - Kinesin steps back*. Nature, 2005. **435**(7040): p. 285-+.

187. Huxley, A.F., *Muscle Structure and Theories of Contraction*. Progress in Biophysics & Molecular Biology, 1957. **7**: p. 255-&.
188. Huxley, A.F. and R.M. Simmons, *Proposed Mechanism of Force Generation in Striated Muscle*. Nature, 1971. **233**(5321): p. 533-&.
189. Hill, T.L., E. Eisenberg, and L. Greene, *Theoretical-Model for the Cooperative Equilibrium Binding of Myosin Subfragment-1 to the Actin-Troponin-Tropomyosin Complex*. Proceedings of the National Academy of Sciences of the United States of America-Biological Sciences, 1980. **77**(6): p. 3186-3190.
190. Cordova, N.J., B. Ermentrout, and G.F. Oster, *Dynamics of Single-Motor Molecules - the Thermal Ratchet Model*. Proceedings of the National Academy of Sciences of the United States of America, 1992. **89**(1): p. 339-343.
191. Imafuku, Y., Y.Y. Toyoshima, and K. Tawada, *Monte Carlo study for fluctuation analysis of the in vitro motility driven by protein motors*. Biophysical Chemistry, 1996. **59**(1-2): p. 139-153.
192. Howard, J., *Mechanics of motor proteins and the cytoskeleton*. 2001, Sunderland, Mass.: Sinauer Associates, Publishers. xvi, 367 p.
193. Wang, H. and G. Oster, *Ratchets, power strokes, and molecular motors*. Applied Physics a-Materials Science & Processing, 2002. **75**(2): p. 315-323.
194. Atzberger, P.J. and C.S. Peskin, *A Brownian Dynamics model of kinesin in three dimensions incorporating the force-extension profile of the coiled-coil cargo tether*. Bulletin of Mathematical Biology, 2006. **68**(1): p. 131-160.
195. Agarwal, A. and H. Hess, *Biomolecular motors at the intersection of nanotechnology and polymer science*. Progress in Polymer Science, 2010. **35**(1-2): p. 252-277.
196. Turner, D.C., et al., *Selective adhesion of functional microtubules to patterned silane surfaces*. Biophysical Journal, 1995. **69**(6): p. 2782-2789.
197. Suzuki, H., et al., *Linear Arrangement of Motor Protein on a Mechanically Deposited Fluoropolymer Thin-Film*. Japanese Journal of Applied Physics Part 1-Regular Papers Short Notes & Review Papers, 1995. **34**(7B): p. 3937-3941.
198. Riveline, D., et al., *Acting on actin: the electric motility assay*. European Biophysics Journal with Biophysics Letters, 1998. **27**(4): p. 403-408.
199. Nicolau, D.V., et al., *Actin motion on microlithographically functionalized myosin surfaces and tracks*. Biophysical Journal, 1999. **77**(2): p. 1126-1134.
200. Mansson, A., *Translational actomyosin research: fundamental insights and applications hand in hand*. Journal of Muscle Research and Cell Motility, 2012. **33**(3-4): p. 219-233.
201. Nishizaka, T., et al., *Unbinding Force of a Single Motor Molecule of Muscle Measured Using Optical Tweezers*. Nature, 1995. **377**(6546): p. 251-254.
202. Nishizaka, T., et al., *Characterization of single actomyosin rigor bonds: Load dependence of lifetime and mechanical properties*. Biophysical Journal, 2000. **79**(2): p. 962-974.
203. Greenberg, M.J., et al., *The direct molecular effects of fatigue and myosin regulatory light chain phosphorylation on the actomyosin contractile apparatus*. American Journal of Physiology-Regulatory Integrative and Comparative Physiology, 2010. **298**(4): p. R989-R996.
204. Hooft, A.M., et al., *An accelerated state of myosin-based actin motility*. Biochemistry, 2007. **46**(11): p. 3513-3520.
205. Rossi, R., et al., *Temperature dependence of speed of actin filaments propelled by slow and fast skeletal myosin isoforms*. Journal of Applied Physiology, 2005. **99**(6): p. 2239-2245.

206. Albet-Torres, N., et al., *Mode of heavy meromyosin adsorption and motor function correlated with surface hydrophobicity and charge*. Langmuir, 2007. **23**(22): p. 11147-11156.
207. Kron, S.J. and J.A. Spudich, *Fluorescent Actin-Filaments Move on Myosin Fixed to a Glass-Surface*. Proceedings of the National Academy of Sciences of the United States of America, 1986. **83**(17): p. 6272-6276.
208. Rice, S.E., T.J. Purcell, and J.A. Spudich, *Building and using optical traps to study properties of molecular motors*. Biophotonics, Pt B, 2003. **361**: p. 112-133.
209. Vale, R.D. and R.A. Milligan, *The way things move: Looking under the hood of molecular motor proteins*. Science, 2000. **288**(5463): p. 88-95.
210. Sweeney, H.L. and A. Houdusse, *Structural and Functional Insights into the Myosin Motor Mechanism*. Annual Review of Biophysics, Vol 39, 2010. **39**: p. 539-557.
211. White, H.D. and E.W. Taylor, *Energetics and Mechanism of Actomyosin Adenosine-Triphosphatase*. Biochemistry, 1976. **15**(26): p. 5818-5826.
212. Eisenberg, E. and T.L. Hill, *Muscle-Contraction and Free-Energy Transduction in Biological-Systems*. Science, 1985. **227**(4690): p. 999-1006.
213. Miller, R.H. and R.J. Lasek, *Cross-Bridges Mediate Anterograde and Retrograde Vesicle Transport Along Microtubules in Squid Axoplasm*. Journal of Cell Biology, 1985. **101**(6): p. 2181-2193.
214. Howard, J., A.J. Hudspeth, and R.D. Vale, *Movement of Microtubules by Single Kinesin Molecules*. Nature, 1989. **342**(6246): p. 154-158.
215. Hackney, D.D., *Highly Processive Microtubule-Stimulated Atp Hydrolysis by Dimeric Kinesin Head Domains*. Nature, 1995. **377**(6548): p. 448-450.
216. Toyoshima, Y.Y., S.J. Kron, and J.A. Spudich, *The Myosin Step Size - Measurement of the Unit Displacement Per Atp Hydrolyzed in an Invitro Assay*. Proceedings of the National Academy of Sciences of the United States of America, 1990. **87**(18): p. 7130-7134.
217. Harada, Y., et al., *Mechanochemical Coupling in Actomyosin Energy Transduction Studied by Invitro Movement Assay*. Journal of Molecular Biology, 1990. **216**(1): p. 49-68.
218. Uyeda, T.Q.P., S.J. Kron, and J.A. Spudich, *Myosin step size: Estimation from slow sliding movement of actin over low densities of heavy meromyosin*. Journal of Molecular Biology, 1990. **214**(3): p. 699-710.
219. Leibler, S. and D.A. Huse, *Porters Versus Rowers - a Unified Stochastic-Model of Motor Proteins*. Journal of Cell Biology, 1993. **121**(6): p. 1357-1368.
220. Dennis, J.R., J. Howard, and V. Vogel, *Molecular shuttles: directed motion of microtubules along nanoscale kinesin tracks*. Nanotechnology, 1999. **10**(3): p. 232-236.
221. Hess, H., et al., *Light-controlled molecular shuttles made from motor proteins carrying cargo on engineered surfaces*. Nano Letters, 2001. **1**(5): p. 235-239.
222. Eigler, D.M. and E.K. Schweizer, *Positioning Single Atoms with a Scanning Tunneling Microscope*. Nature, 1990. **344**(6266): p. 524-526.
223. Yin, Y.D., et al., *Template-assisted self-assembly: A practical route to complex aggregates of monodispersed colloids with well-defined sizes, shapes, and structures*. Journal of the American Chemical Society, 2001. **123**(36): p. 8718-8729.
224. Bachand, G.D., et al., *Active Capture and Transport of Virus Particles Using a Biomolecular Motor-Driven, Nanoscale Antibody Sandwich Assay*. Small, 2006. **2**(3): p. 381-385.
225. Ionov, L., M. Stamm, and S. Diez, *Size sorting of protein assemblies using polymeric gradient surfaces*. Nano Letters, 2005. **5**(10): p. 1910-1914.

226. Hess, H., J. Howard, and V. Vogel, *A Piconewton Forceometer Assembled from Microtubules and Kinesins*. Nano Letters, 2002. **2**(10): p. 1113-1115.
227. Bull, J.L., A.J. Hunt, and E. Meyhofer, *A theoretical model of a molecular-motor-powered pump*. Biomedical Microdevices, 2005. **7**(1): p. 21-33.
228. Hess, H., et al., *Surface Imaging by Self-Propelled Nanoscale Probes*. Nano Letters, 2001. **2**(2): p. 113-116.
229. Kerssemakers, J., et al., *3D Nanometer Tracking of Motile Microtubules on Reflective Surfaces*. Small, 2009. **5**(15): p. 1732-1737.
230. Vroman, L., *Effect of Adsorbed Proteins on the Wettability of Hydrophilic and Hydrophobic Solids*. Nature, 1962. **196**(4853): p. 476-477.
231. Andrade, J.D., *Surface and interfacial aspects of biomedical polymers*. 1985, New York: Plenum Press.
232. Castner, D.G. and B.D. Ratner, *Biomedical surface science: Foundations to frontiers*. Surface Science, 2002. **500**(1-3): p. 28-60.
233. Lopez, G.P., et al., *Glow-Discharge Plasma Deposition of Tetraethylene Glycol Dimethyl Ether for Fouling-Resistant Biomaterial Surfaces*. Journal of Biomedical Materials Research, 1992. **26**(4): p. 415-439.
234. Dalsin, J.L., et al., *Mussel adhesive protein mimetic polymers for the preparation of nonfouling surfaces*. Journal of the American Chemical Society, 2003. **125**(14): p. 4253-4258.
235. Nakanishi, K., T. Sakiyama, and K. Imamura, *On the adsorption of proteins on solid surfaces, a common but very complicated phenomenon*. Journal of Bioscience and Bioengineering, 2001. **91**(3): p. 233-244.
236. Balaz, M., et al., *Effects of surface adsorption on catalytic activity of heavy meromyosin studied using a fluorescent ATP analogue*. Biochemistry, 2007. **46**(24): p. 7233-7251.
237. Jaber, J.A., P.B. Chase, and J.B. Schlenoff, *Actomyosin-driven motility on patterned polyelectrolyte mono- and multilayers*. Nano Letters, 2003. **3**(11): p. 1505-1509.
238. Mansson, A., et al., *In vitro assays of molecular motors - impact of motor-surface interactions*. Frontiers in Bioscience, 2008. **13**: p. 5732-5754.
239. Ratner, B.D. and S.J. Bryant, *BIOMATERIALS: Where We Have Been and Where We are Going*. Annual Review of Biomedical Engineering, 2004. **6**(1): p. 41-75.
240. Fischer, T. and H. Hess, *Materials chemistry challenges in the design of hybrid bionanodevices: supporting protein function within artificial environments*. Journal of Materials Chemistry, 2007. **17**(10): p. 943-951.
241. Caruso, F., et al., *Quartz-Crystal Microbalance and Surface-Plasmon Resonance Study of Surfactant Adsorption onto Gold and Chromium-Oxide Surfaces*. Langmuir, 1995. **11**(5): p. 1546-1552.
242. Geddes, N.J., et al., *Piezoelectric Crystal for the Detection of Immunoreactions in Buffer Solutions*. Sensors and Actuators B-Chemical, 1994. **17**(2): p. 125-131.
243. Hook, F., et al., *A comparative study of protein adsorption on titanium oxide surfaces using in situ ellipsometry, optical waveguide lightmode spectroscopy, and quartz crystal microbalance/dissipation*. Colloids and Surfaces B-Biointerfaces, 2002. **24**(2): p. 155-170.
244. Rickert, J., A. Brecht, and W. Gopel, *Quartz crystal microbalances for quantitative biosensing and characterizing protein multilayers*. Biosensors & Bioelectronics, 1997. **12**(7): p. 567-575.
245. Sauerbrey, G., *Verwendung von Schwingquarzen zur Wägung dünner Schichten und zur Mikrowägung*. Zeitschrift Fur Physik, 1959. **155**(2): p. 206-222.

246. Taussky, H.H. and E. Shorr, *A Microcolorimetric Method for the Determination of Inorganic Phosphorus*. Journal of Biological Chemistry, 1953. **202**(2): p. 675-685.
247. Clemmens, J., et al., *Mechanisms of microtubule guiding on microfabricated kinesin-coated surfaces: Chemical and topographic surface patterns*. Langmuir, 2003. **19**(26): p. 10967-10974.
248. Sundberg, M., et al., *Actin filament guidance on a chip: Toward high-throughput assays and lab-on-a-chip applications*. Langmuir, 2006. **22**(17): p. 7286-7295.
249. Stracke, R., et al., *Physical and technical parameters determining the functioning of a kinesin-based cell-free motor system*. Nanotechnology, 2000. **11**(2): p. 52-56.
250. Hiratsuka, Y., et al., *Controlling the direction of kinesin-driven microtubule movements along microlithographic tracks*. Biophysical Journal, 2001. **81**(3): p. 1555-1561.
251. Mahanivong, C., et al., *Manipulation of the motility of protein molecular motors on microfabricated substrates*. Biomedical Microdevices, 2002. **4**(2): p. 111-116.
252. Wright, J., et al., *Micropatterning of myosin on O-acryloyl acetophenone oxime (AAPO), layered with bovine serum albumin (BSA)*. Biomedical Microdevices, 2002. **4**(3): p. 205-211.
253. van den Heuvel, M.G.L., et al., *High rectifying efficiencies of microtubule motility on kinesin-coated gold nanostructures*. Nano Letters, 2005. **5**(6): p. 1117-1122.
254. Asokan, S.B., et al., *Two-dimensional manipulation and orientation of actin-myosin systems with dielectrophoresis*. Nano Letters, 2003. **3**(4): p. 431-437.
255. Kron, S.J. and J.A. Spudich, *Fluorescent actin filaments move on myosin fixed to a glass surface*. Proceedings of the National Academy of Sciences, 1986. **83**(17): p. 6272-6276.
256. Tawada, K. and K. Sekimoto, *A physical model of ATP-induced actin-myosin movement in vitro*. Biophysical Journal, 1991. **59**(2): p. 343-356.
257. Chase, P.B., et al., *Viscosity and solute dependence of F-actin translocation by rabbit skeletal heavy meromyosin*. American Journal of Physiology-Cell Physiology, 2000. **278**(6): p. C1088-C1098.
258. Hunt, A.J., F. Gittes, and J. Howard, *The force exerted by a single kinesin molecule against a viscous load*. Biophysical Journal, 1994. **67**(2): p. 766-781.
259. Uyeda, T.Q.P., S.J. Kron, and J.A. Spudich, *Myosin step size – estimation from slow sliding movement of actin over low densities of heavy-meromyosin*. Journal of Molecular Biology, 1990. **214**(3): p. 699-710.
260. Harris, D.E. and D.M. Warshaw, *Smooth and skeletal- muscle myosin both exhibit low duty cycles at zero load in-vitro*. Journal of Biological Chemistry, 1993. **268**(20): p. 14764-14768.
261. Spudich, J.A., *How molecular motors work*. Nature, 1994. **372**(6506): p. 515-518.
262. Tyska, M.J., et al., *Two heads of myosin are better than one for generating force and motion*. Proceedings of the National Academy of Sciences of the United States of America, 1999. **96**(8): p. 4402-4407.
263. Yengo, C.M., et al., *Actin-induced closure of the actin-binding cleft of smooth muscle myosin*. Journal of Biological Chemistry, 2002. **277**(27): p. 24114-24119.
264. Lorenz, M. and K.C. Holmes, *The actin-myosin interface*. Proceedings of the National Academy of Sciences of the United States of America, 2010. **107**(28): p. 12529-12534.
265. Harris, D.E. and D.M. Warshaw, *Smooth and Skeletal-Muscle Myosin Both Exhibit Low Duty Cycles at Zero Load in-Vitro*. Journal of Biological Chemistry, 1993. **268**(20): p. 14764-14768.

266. Saito, K., et al., *Movement of Single Myosin-Filaments and Myosin Step-Size on an Actin Filament Suspended in Solution by a Laser Trap*. Biophysical Journal, 1994. **66**(3): p. 769-777.
267. Guo, B. and W.H. Guilford, *The tail of myosin reduces actin filament velocities in the in vitro motility assay*. Biophysical Journal, 2004. **86**(1): p. 53a-53a.
268. Miyata, H., et al., *Mechanical Measurements of Single Actomyosin Motor Force*. Biophysical Journal, 1995. **68**(4): p. S286-S290.
269. Hosek, M. and J.X. Tang, *Polymer-induced bundling of F actin and the depletion force*. Physical Review E, 2004. **69**(5).
270. Guo, B. and W.H. Guilford, *The tail of myosin reduces actin filament velocity in the in vitro motility assay*. Cell Motil. Cytoskel., 2004. **59**(4): p. 264-272.
271. Albet-Torres, N., et al., *Molecular motors on lipid bilayers and silicon dioxide: different driving forces for adsorption*. Soft Matter, 2010. **6**(14): p. 3211-3219.
272. Persson, M., et al., *Heavy Meromyosin Molecules Extending More Than 50 nm above Adsorbing Electronegative Surfaces*. Langmuir, 2010. **26**(12): p. 9927-9936.
273. M.M.M. Elnasharty, A.M.G., G.M. Turkey, M. Kamal, Fatima H Labeed, M.P. Hughes, K.F. Hoettges, *Cell Membrane Analysis Using Modulated Dielectrophoresis*. ROMANIAN J. BIOPHYS, 2012. **22**(3).